LUND UNIVERSITY

Photoemission Electron Microscopy for Ultrafast Nano-Optics - Femtoseconds to Attoseconds

Mårsell, Erik

2015

Photoemission Electron Microscopy for Ultrafast Nano-Optics

Femtoseconds to Attoseconds

Erik Mårsell

LUND
UNIVERSITY

DOCTORAL THESIS

by due permission of the Faculty of Science, Lund University, Sweden.
To be defended in the Rydberg Lecture Hall at the Department of Physics,
29 January 2016 at 09:15.

Faculty opponent:
Prof. Martin Aeschlimann
Technische Universität Kaiserslautern

Organization
LUND UNIVERSITY

Division of Synchrotron Radiation Research
Department of Physics
Box 118, S-221 00 Lund
Author:
Erik Mårsell

Document name
DOCTORAL THESIS

Date of issue
18 December 2015

Sponsoring organization

Title and subtitle
Photoemission Electron Microscopy for Ultrafast Nano-Optics: Femtoseconds to Attoseconds

Abstract

Ultrafast nano-optics is a new and quickly evolving research field centred around the control, manipulation, and application of light on a nanometre and femtosecond scale. This can lead to improved electro-optical devices, more sensitive spectroscopy, and real-time control of chemical reactions. However, understanding the simultaneous nanometre and femtosecond evolution of nano-optical fields requires characterization methods with ultrahigh spatiotemporal resolution. A method that during the past 15 years has shown great promise for such studies is photoemission electron microscopy (PEEM) in combination with ultrashort laser pulses. Both PEEM, nanostructure fabrication methods, and a large variety of pulsed light sources are under rapid parallel development, leading also to quickly increasing possibilities of nanometre and femtosecond characterization.

This thesis explores the combination of PEEM with various state-of-the-art lab-based sources of femtosecond and attosecond pulses with wavelengths spanning from 30 nm to 1.55 μm for studies of ultrafast nano-optics. It is based on experiments carried out with five different laser systems, studying light interaction with tailored metallic and semiconducting nanostructures. The work comprises construction of new experimental setups, PEEM measurements, development of data analysis tools, and complementary investigations using techniques such as scanning electron microscopy, X-ray photoelectron spectroscopy, and scanning tunnelling microscopy.

Using few-cycle pulses from an ultra-broadband Ti:sapphire oscillator, localized surface plasmons in metallic nanostructures were studied with a temporal resolution down to a few femtoseconds. Metallic structures were also studied with PEEM using femtosecond pulses in the telecommunication wavelength regime. Other light sources employed include an optical parametric chirped pulse amplification system, with which anisotropy effects in semiconductor nanowires were studied.

Finally, the thesis explores the use of extreme ultraviolet attosecond pulse trains produced by high-order harmonic generation (HHG) as light source for PEEM. Working with 1 kHz repetition rate, the spatial resolution was found to be limited by space charge effects to a few hundred nanometres. However, with a new HHG system working at 200 kHz repetition rate, the resolution was improved by a factor of 2—3, along with a reduction in acquisition time by an order of magnitude. Novel high-repetition rate attosecond light sources are therefore expected to play a key role in pushing the temporal resolution of PEEM into the attosecond regime.

Key words

PEEM, ultrashort laser pulses, ultrafast nano-optics, plasmonics, silver nanoparticles, semiconductor nanowires, nonlinear photoemission, attosecond pulses, high-order harmonic generation

Classification system and/or index terms (if any)

Supplementary bibliographical information

Language
English

ISSN and key title

ISBN
978-91-7623-614-7 (print)
978-91-7623-615-4 (pdf)

Recipient's notes

Number of pages
218

Price

Security classification

Photoemission Electron Microscopy for Ultrafast Nano-Optics

Femtoseconds to Attoseconds

Erik Mårsell

Doctoral thesis

2015

Division of Synchrotron Radiation Research
Department of Physics
Lund University

LUND
UNIVERSITY

Front cover: Combination of microscopy techniques for functional and aesthetic visualization of near-field enhancement. A scanning electron micrograph (blue) of a single rice-shaped silver nanoparticle is overlaid by a multiphoton photoemission electron micrograph (red) of the very same particle, showing the enhanced electric fields at the two ends.

Back cover: Different types of fields commonly encountered in southern Sweden.

Division of Synchrotron Radiation Research
Department of Physics
Lund University

ISBN: 978-91-7623-614-7 (print)
ISB(N+1): 978-91-7623-615-4 (pdf)

Printed in Sweden by Media-Tryck, Lund University
Lund 2015

"The idea of posting wise quotes by inspirational masterminds was all ruined when the internet started to get spammed with fake ones."

Sir Isaac Newton

Abstract

Ultrafast nano-optics is a new and quickly evolving research field centred around the control, manipulation, and application of light on a nanometre and femtosecond scale. This can lead to improved electro-optical devices, more sensitive spectroscopy, and real-time control of chemical reactions. However, understanding the simultaneous nanometre and femtosecond evolution of nano-optical fields requires characterization methods with ultrahigh spatiotemporal resolution. A method that during the past 15 years has shown great promise for such studies is photoemission electron microscopy (PEEM) in combination with ultrashort laser pulses. Both PEEM, nanostructure fabrication methods, and a large variety of pulsed light sources are under rapid parallel development, leading also to quickly increasing possibilities of nanometre and femtosecond characterization.

This thesis explores the combination of PEEM with various state-of-the-art lab-based sources of femtosecond and attosecond pulses with wavelengths spanning from 30 nm to 1.55 μm for studies of ultrafast nano-optics. It is based on experiments carried out with five different laser systems, studying light interaction with tailored metallic and semiconducting nanostructures. The work comprises construction of new experimental setups, PEEM measurements, development of data analysis tools, and complementary investigations using techniques such as scanning electron microscopy, X-ray photoelectron spectroscopy, and scanning tunnelling microscopy.

Using few-cycle pulses from an ultra-broadband Ti:sapphire oscillator, localized surface plasmons in metallic nanostructures were studied with a temporal resolution down to a few femtoseconds. Metallic structures were also studied with PEEM using femtosecond pulses in the telecommunication wavelength regime. Other light sources employed include an optical parametric chirped pulse amplification system, with which anisotropy effects in semiconductor nanowires were studied.

Finally, the thesis explores the use of extreme ultraviolet attosecond pulse trains produced by high-order harmonic generation (HHG) as light source for PEEM. Working with 1 kHz repetition rate, the spatial resolution was found to be limited by space charge effects to a few hundred nanometres. However, with a new HHG system working at 200 kHz repetition rate, the resolution was improved by a factor of 2–3, along with a reduction in acquisition time by an order of magnitude. Novel high-repetition rate attosecond light sources are therefore expected to play a key role in pushing the temporal resolution of PEEM into the attosecond regime.

Populärvetenskaplig sammanfattning

Nanotekniken håller i skrivande stund på att revolutionera samhället med nya innovationer inom exempelvis elektronik och medicin. En viktig del i detta är utvecklingen av nya och förbättrade sätt att avbilda strukturer av nanometerstorlek (en nanometer är en miljarddels meter). Avancerade karakteriseringsmetoder skapar en ökad förståelse för hur nanostrukturer beter sig, vilket är en förutsättning för utvecklingen av nya komponenter. Särskilt viktiga är metoder för att karakterisera egenskaper hos ytor, eftersom ytan hos ett material får större effekt ju mindre partiklar materialet består av.

På ett mer fundamentalt plan har forskare de senaste decennierna lyckats mäta snabbare och snabbare processer, ända ned på en skala av femtosekunder och attosekunder. En femtosekund är en miljondels miljarddels sekund, och en attosekund är tusen gånger kortare. Det går ungefär dubbelt så många attosekunder på en sekund som det har gått sekunder sedan Big Bang. Genom att skapa ljuspulser som bara varar i ett hundratal attosekunder går det därför att mäta hur fort grundläggande processer inuti atomer går.

Denna jakt på att kunna mäta mindre strukturer och snabbare processer kan liknas vid dagens IT-samhälle. Mobiltelefoner får plats i fickan men kan ändå utföra många processer samtidigt och lagra stora mängder data. Detta har möjliggjorts genom miniatyriseringen av elektroniska komponenter. När telefonen används för att kommunicera med är prioriteringen i stället att signalerna ska sändas fort, med många bitar information per sekund. Därför används elektromagnetiska vågor som signaler genom luften och genom optiska fibrer. En stor utmaning är att koppla samman dessa teknologier för att skapa komponenter och kretsar som samtidigt är små och snabba. Det är här forskningen kring ultrasnabb nano-optik kommer in.

Ljus är det absolut snabbaste som finns, men kan normalt sett inte koncentreras på en skala mindre än dess våglängd, som är hundratals nanometer (i detta sammanhang ansett som ett långt avstånd). Nano-optik handlar om att kringgå detta genom att skapa ytor av olika material och former för att koncentrera ljuset ytterligare. Metalliska nanostrukturer är särskilt bra på detta genom en speciell sorts "partikel", kallad ytplasmon, som uppkommer genom att ljuset växelverkar med elektronerna i metallen. Forskningsfältet kring ytplasmoner kallas för plasmonik, och utgör en viktig del av nano-optiken.

För att förstå ljusets extremt snabba rörelser i nanostrukturer krävs avbildningstekniker som samtidigt kan mäta ljus på en liten längdskala och kort tidsskala. Ett av de mest framgångsrika instrumenten för detta är fotoemissionselektronmikroskopet, som skapar en kraftigt förstorad bild av elektroner som avges från en yta när den träffas av ljus. Återigen ligger styrkan i att kombinera

de små elektronerna med det snabba ljuset. Fotoemissionselektronmikroskopet har använts för att studera ultrasnabb nano-optik sedan 2001, med mer och mer avancerade experimentuppställningar.

Den här avhandlingen handlar om användningen av nya typer av avancerade laserljuskällor för att studera ultrasnabb nano-optik i fotoemissionselektronmikroskop. En av de nya ljuskällorna visar sig kunna avbilda hur ljuset svänger olika snabbt i olika delar av en nanopartikel under ett fåtal femtosekunder. En annan kan användas för att studera hur ljuset växelverkar med specialdesignade nanotrådar av halvledarmaterial. Ytterligare en typ av ljuskälla utforskas på grund av dess förmåga att sända ut pulser på attosekundskalan. Tillsammans visar experimenten hur de senaste årens utveckling inom laserfysiken ger upphov till många nya möjligheter för karakterisering av ljusets växelverkan med nanostrukturer. Nya karakteriseringsmetoder är en förutsättning för en ökad förståelse för nano-optik, en teknologi som kan leda till såväl förbättrade solceller som optiska logiska kretsar med överlägsen hastighet.

List of Papers

This doctoral thesis is based on the following papers, which in the text will be referred to by their Roman numerals.

Paper I—Direct Subwavelength Imaging and Control of Near-Field Localization in Individual Silver Nanocubes
E. Mårsell, R. Svärd, M. Miranda, C. Guo, A. Harth, E. Lorek, J. Mauritsson, C. L. Arnold, H. X. Xu, A. L'Huillier, A. Mikkelsen, and A. Losquin.
Applied Physics Letters **107,** 201111 (2015).

I suggested the experiment, I took major part in performing the experiments and analysing the data, and I was the main responsible for writing the paper.

Paper II—Nanoscale Imaging of Local Few-Femtosecond Near-Field Dynamics within a Single Plasmonic Nanoantenna
E. Mårsell, A. Losquin, R. Svärd, M. Miranda, C. Guo, A. Harth, E. Lorek, J. Mauritsson, C. L. Arnold, H. X. Xu, A. L'Huillier, and A. Mikkelsen.
Nano Letters **15,** 6601–6608 (2015).

I planned the experiment, took part in constructing the experimental setup, I performed the experiment, analysed the data and the simulations, and wrote the paper.

Paper III—Size and Shape Dependent Few-Cycle Near-Field Dynamics in Individual Bow-Tie Nanoantennas
E. Lorek, E. Mårsell, A. Losquin, M. Miranda, A. Harth, C. Guo, R. Svärd, C. L. Arnold, A. L'Huillier, A. Mikkelsen, and J. Mauritsson.
Optics Express **23,** 31460–31471 (2015).

I took part in the planning of the experiment and the sample design, and I was the main responsible for performing the experiments. I developed some of the analysis tools, and I took part in the analysis and the writing of the paper.

Paper IV—Photoemission Electron Microscopy of Localized Surface Plasmons in Silver Nanostructures at Telecommunication Wavelengths
E. Mårsell, E. W. Larsen, C. L. Arnold, H. X. Xu, J. Mauritsson, and A. Mikkelsen.
Journal of Applied Physics **117,** 083104 (2015).

I was the main responsible for performing the PEEM and STM experiments, I analysed the data, and I took significant part in the writing of the paper.

Paper V—Direct Imaging of Crystal Phase Dependent Multiphoton Photoemission from InAs Nanowires
E. Mårsell, A. Harth, A. Losquin, C. Guo, Y.-C. Cheng, R. Svärd, E. Lorek, S. Lehmann, G. Nylund, C. L. Arnold, M. Miranda, K. A. Dick, J. Mauritsson, A. L'Huillier, and A. Mikkelsen.
In manuscript

I planned and performed the experiments, I was the main responsible for the analysis and interpretation of the data and simulations, and I wrote the paper.

Paper VI—Secondary Electron Imaging of Nanostructures Using Extreme Ultra-Violet Attosecond Pulse Trains and Infra-Red Femtosecond Pulses
E. Mårsell, C. L. Arnold, E. Lorek, D. Guenot, T. Fordell, M. Miranda, J. Mauritsson, H. X. Xu, A. L'Huillier, and A. Mikkelsen.
Annalen der Physik **525,** 162-170 (2013).

I was involved in the planning of the experiments, and I was the main responsible for the laboratory work. I developed and performed the Monte Carlo simulations, and I took significant part in the writing of the paper.

Paper VII—Imaging Localized Surface Plasmons by Femtosecond to Attosecond Time-Resolved Photoelectron Emission Microscopy—"ATTO-PEEM"
S. H. Chew, K. Pearce, C. Späth, A. Guggenmos, J. Schmidt, F. Süßmann, M. F. Kling, and U. Kleineberg.

E. Mårsell, C. L. Arnold, E. Lorek, P. Rudawski, C. Guo, M. Miranda, F. Ardana, J. Mauritsson, A. L'Huillier, and A. Mikkelsen.

In *"Attosecond Nanophysics: From Basic Science to Applications"*, edited by Peter Hommelhoff and Matthias Kling, Wiley-VCH, pp 325–364 (2015).

I was responsible for the experiments described as "second and third generation" in the second part (section 10.3.3) of the chapter, I analysed the corresponding data, and I took part in the writing of the chapter.

I also contributed to the following papers, which are outside the scope of this thesis:

Paper VIII—Manipulating the Dynamics of Self-Propelled Gallium Droplets Using Gold Nanoparticles and Nanoscale Surface Morphology
A. A. Zakharov, E. Mårsell, E. Hilner, R. Timm, J. N. Andersen, E. Lundgren, and A. Mikkelsen.
ACS Nano **9,** 5422–5431 (2015).

Paper IX—Characterizing the Geometry of InAs Nanowires using Mirror Electron Microscopy
S. M. Kennedy, M. Hjort, B. Mandl, E. Mårsell, A. A. Zakharov, A. Mikkelsen, D. M. Paganin and D. E. Jesson.
Nanotechnology **23,** 125703 (2012).

Paper X—Alloying and Oxidation of *in situ* Produced Core–Shell Al@Yb Nanoalloy Particles—An "On-the-Fly" Study
C. Zhang, T. Andersson, M.-H. Mikkelä, E. Mårsell, O. Björneholm, X. Xu, M. Tchaplyguine, and Z. Liu.
Journal of Chemical Physics **141,** 084302 (2014).

Abbreviations and Symbols

APT	Attosecond Pulse Train
BBO	Beta Barium Borate, β-BaB_2O_4
CA	Contrast Aperture
CEP	Carrier–Envelope Phase
CPA	Chirped Pulse Amplification
E_F	Fermi level energy
E_{vac}	Vacuum level energy
FWHM	Full-Width at Half Maximum
GDD	Group Delay Dispersion
HHG	High-order Harmonic Generation
IR	Infrared
IS-PEEM	Integral Sample Stage Photoemission Electron Microscope
ITO	Indium Tin Oxide
ITR-PEEM	Interferometric Time-Resolved Photoemission Electron Microscopy
LASER	Light Amplification by Stimulated Emission of Radiation
LEEM	Low Energy Electron Microscopy
LSP	Localized Surface Plasmon
nPPE	n-Photon Photoemission
$n(\omega)$	Refractive index
OPA	Optical Parametric Amplification
OPCPA	Optical Parametric Chirped Pulse Amplification
PEEM	Photoemission Electron Microscopy
p-polarization	Electric field parallel to the plane of incidence
s-polarization	Electric field perpendicular to the plane of incidence
SE	Secondary Electron
SEM	Scanning Electron Microscopy
SHG	Second Harmonic Generation
SPP	Surface Plasmon Polariton
XUV	Extreme Ultraviolet
Δt	Pulse duration, FWHM
$\Delta\omega$	Pulse spectral width, FWHM
$\epsilon(\omega)$	Dielectric function
θ	Polarization angle
τ	Temporal delay
Φ	Work function
$\phi(\omega)$	Spectral phase
ω_0	Carrier frequency
ω_p	Plasma frequency
$\hbar\omega$	Photon energy

Acknowledgements

Working in a collaborative project surrounded by experts in a large variety of fields, there are many people to whom I am indebted. I have received plenty of help with all aspects of work, I have had access to excellent equipment and samples, and I have also had a great time during my PhD. I would like to thank all of you who have made this happen, and I apologize in advance for leaving out anyone.

First, and most importantly, I want to thank my main supervisor Anders Mikkelsen. Your broad knowledge of anything going on at a surface and how to measure it is surpassed only by your encouragement, inspiration, and positive spirit. It has been a true pleasure to work with you, and I could not have wished for a better supervisor.

Thanks also to my co-supervisor Anne L'Huillier. Besides knowing everything worth to know about high-order harmonic generation, you manage to lead a large group of researchers through inspiration, with a visionary attitude and plenty of enthusiasm as soon as someone is "doing physics" in your labs.

Arthur Losquin, I have really enjoyed working with you these past two years. Before you arrived I very much missed having a true plasmonics-geek around to discuss with. Thank you for sharing joy and frustration caused by alternating accomplishments and setbacks, and thank you for being head of simulations.

None of the work behind this thesis would have been possible without the people developing and running the fantastic laser sources here in Lund. Big thanks to all of you, from Thomas Fordell and Jörg Schwenke who helped me with my first experiments, via Cord Arnold, Miguel Miranda, and Diego Guénot who have been around for most of my time here (thanks Cord for your not-always-so-appropriate comments and drawings during some frustrating times in the lab at a way too late hour), to Piotr Rudawski, Anne Harth, and Chen Guo who managed to get light out of the seemingly impossible MHz system. Esben Witting Larsen, thanks for the TOPAS-PEEM project, for letting me play black metal in the lab, and for your Danish sense of humour. Thanks to Eleonora Lorek and Johan Mauritsson for work on the harmonic generation setup and on the FIB structures. To all of you laser people: not only have you always worked day and night to get the lasers running, but you have also made me feel very welcome in your group.

Elisabeth Nilsson and Knut Deppert, thanks for running the engineering nanoscience program back in the days, and for being sources of inspiration when it comes to teaching, especially in relation to the sustainable development course. Elisabeth, it has been a pleasure to assist in teaching your courses. The education system needs more people like you.

Thanks to Lars Samuelson and all the other people who have made sure that Lund University is among the world leaders in nanoscience. An associated thank you to Sebastian Lehmann, Magnus Borgström, Daniel Jacobsson, and other "nanowire farmers" for providing "probably the best III–V nanowires in the world".

Thanks to Hongxing Xu for discussing plasmonics, for providing excellent silver nanostructures (used in 5 out of 7 papers in this thesis!), and for a very pleasant visit in Beijing.

Alexei Zhakarov and Yuran Niu, thanks for showing me what a real PEEM instrument looks like, and for company at the LEEM/PEEM conferences.

I have had the pleasure of working together with a few diploma workers during these years. Thanks to David Engberg and Björn Erik Skovdal for good times in the lab and measuring plenty of nanowires. An extra large thank you to Robin Svärd for all the work you put in on both experiments and simulations.

Thanks to the people who have given me feedback on my thesis, including Anders Mikkelsen, Anne L'Huillier, Cord Arnold, Arthur Losquin, and Johan Knutsson.

Thanks to collaborators at the division of Chemical Physics, where I have spent some time first borrowing their laser, and later in an attempt to do THz STM. Thanks also to Sarah McKibbin for sharing lab time, STM experience, laughter, and frustration in relation to this project.

Thanks to alla@sljus for creating a relaxed and inspirational environment to work in. Being able to let go of work for a while to socialize during lunches and coffee breaks has been very important to me. Thanks also to the people with whom I've shared offices for standing to be around me almost every day.

Patrik Wirgin and Anneli Nilsson-Ahlm, thanks for your patience with everything economic and administrative that I don't understand.

Martin Hjort, thanks for being an inexhaustible source of knowledge about everything from surface science and UHV work to what happened in yesterday's reality shows and the latest gossip about the Royal family. Thanks also for always having a pun to tell (or write on the board), and for sharing literally thousands of beers during these years.

Thanks to the Fun in Fysicum (RIP) crew for organizing all the activities, especially the ping pong tournaments. Thanks also to those involved in the more recent OSA/SPIE activities (and the associated semi-violent Jungle speed games), as well as to everyone who has organized events such as Kick-offs, nmC/NanoLund retreats, and ADMIRE workshops.

Thanks to Filip Lenrick, Martin Hjort, Daniel Jacobsson, and all of our visitors for the excellent conference updates. Our inter-department, inter-faculty sharing of international experiences on the highest possible level has been very rewarding.

I would like to thank Christoph Lemke for conference company and for sending me curry wurst-flavoured energy drink.

Johan Valentin Knutsson and Olof Persson are acknowledged for their entertaining pretzel stick duel. I would also like to thank Mogunda5 . for never being afraid to use the f-word.

Thanks to Daniel Jacobsson, Johan Valentin Knutsson, *et al.* for reminding me of how fun skiing is.

Thanks to people such as Martin Hjort, Erik Månsson, Elin Gråsnäs, Sara Blomberg, Olof Persson, Sofie Yngman, and Johan Valentin Knutsson for general spirit-enhancing activities, including but not limited to inappropriate comments, word puns, growing cress in keyboards, photographing leeks in vacuum chambers, scaring economists, and not finishing ski races.

Arvo.

Finally, thanks to all of my friends for support and for reminding me of the world outside academia (and to Mattias for reminding me of the existence of other parts of academia by referring to me as "nano-tomte"). Thanks also to my family; from my late grandfather Ludde who introduced me to academia without me (or him, I think) knowing it, via my parents who have always inspired me to learn new things, to my older sisters who led the way from the start by doing their homework out loud.

Bottom line is:
Every person mentioned above has contributed to this thesis. Thank you.

Contents

Chapter 1

Introduction

Technological advances during the past century have made electrical devices smaller and faster, energy conversion more efficient, and chemical sensors able to detect single molecules. Many of these advances, from the long-distance communication facilitating the internet, via the electronic components in our smartphones, to the solar cells steadily gaining market shares in electricity production, rely on the interaction between light and electrons in materials. Traditionally, the small electronic semiconductor components have been relatively slow due to the reliance on motion of electrons, while the faster photonic components have been large because of the long wavelength of the employed light. A major challenge has therefore been to find a way of manufacturing components that are both small and fast. One approach is based on the concentration of light down to subwavelength dimensions, a research field known as nano-optics. Particularly interesting is the interaction of light with metallic nanostructures, where the free conduction electrons can give rise to collective excitations known as surface plasmons. Surface plasmons are the cornerstone in plasmonics, which is an emerging technology with the capability of filling the needs for devices that are both small and fast. This is illustrated in figure 1.1, mapping various technologies on the basis of speed and size [1].

The upper left quadrant in figure 1.1, representing metallic nanoplasmonics, extends to the regime of a few nanometres ($1\,\text{nm} = 10^{-9}$ m) and a few femtoseconds ($1\,\text{fs} = 10^{-15}$ s) (1 PHz corresponds to a period of 1 fs). Bringing optics to the nanoscale through plasmonics therefore means that signal transport occurs on a nanometre length scale and a femtosecond, or even attosecond ($1\,\text{as} = 10^{-18}$ s), timescale. This calls for the development of new characterization methods for imaging of light concentration and dynamics with extreme spatiotemporal resolution.

The development of characterization methods has for the most part focused on improving either the spatial or the temporal resolution. For spatial resolution, optical microscopes are fundamentally limited by diffraction to a resolution of approximately half the wavelength of light, or a few hundred nanometres. This limit was circumvented by the, eventually Nobel Prize awarded, invention of the electron microscope in the 1930s [2]. Much like light, electrons also have a wave-like nature, but typically with a much shorter wavelength than light. This has led modern electron microscopes to reach sub-Ångström spatial resolution [3, 4]. The high spatial resolution possible with electron probes is in analogy to the

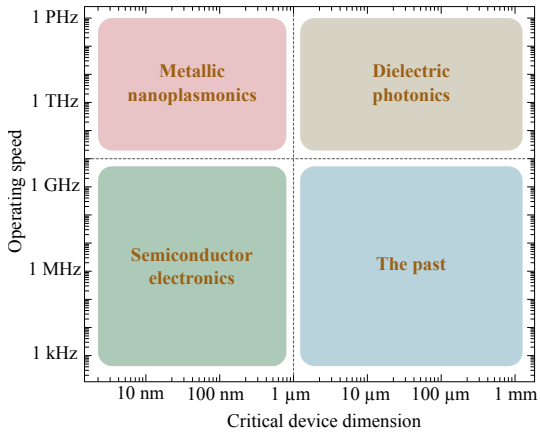

Figure 1.1: Illustration of the typical dimensions and operating speeds of various technologies [1].

small size possible for electronic components, as illustrated in figure 1.1.

Conversely, optical methods have been the most successful for measurements with high temporal resolution. Much like an electron can be squeezed into a smaller space than light, light can be concentrated into shorter bursts than electrons. This opens up possibilities for capturing snapshots of very fast dynamic processes. A famous early-day example of a time-resolved experiment is the film of the galloping horse recorded in 1878 with a time resolution of 1 ms. In modern experiments, electron dynamics have been measured with a temporal resolution reaching below 100 attoseconds [5, 6]. This improvement in temporal resolution by a factor of ten trillion can be compared to the ten thousand-fold improvement in state-of-the-art spatial resolution during the same period of time.

The impressive development of time-resolved measurements can to a large extent be attributed to the invention of the laser (Light Amplification by Stimulated Emission of Radiation) in 1960 [7]. This versatile source of intense, coherent light has since been developed to produce bursts of light as short as a single oscillation of the optical field, which is on the order of a few femtoseconds [8]. Application of femtosecond laser pulses to study the dynamics of chemical reactions, known as femtochemistry, gave Ahmed Zewail the Nobel Prize in Chemistry in 1999 [9]. Since then, the field of attosecond science has emerged thanks to the discovery and development of high-order harmonic generation, the highly nonlinear frequency upconversion that can occur when very strong electromagnetic fields interact with matter [10, 11]. This phenomenon has pushed the duration of the shortest light bursts to below 100 as [8, 12].

A natural approach for developing characterization methods with simultaneously high spatial and temporal resolution is to combine electrons and light to get the best from both worlds. This is done in photoemission electron microscopy (PEEM), where light illuminates a surface and electrons emitted through the

photoelectric effect are used to form an image. This method was introduced by Brüche in 1933 [13]. In PEEM, the spatial resolution is defined by the electron optics, but the technique can still be used to image light on a surface through photoemission. The combination of PEEM and short laser pulses has therefore been used for simultaneous nanometre and femtosecond resolved imaging since the beginning of the 21st century [14–16].

In 2007, it was proposed that PEEM could be used in combination with attosecond pulses produced by high-order harmonic generation to push the temporal resolution into the attosecond regime [17]. This initiated experimental efforts to combine high-order harmonics with PEEM in (at least) two separate research groups [18, 19]. So far, the experiments have turned out to be quite challenging because of most high-harmonic sources not being suitable for PEEM. The concept of PEEM with attosecond temporal resolution therefore to this day remains a theoretical proposal. However, the recent and ongoing development of high-order harmonic sources working at high repetition rates opens up new possibilities for PEEM imaging using attosecond pulses, and eventually for nanometre-resolved films of attosecond electron dynamics at nanostructure surfaces.

1.1 Aim and outline of this thesis

This doctoral thesis summarizes five years of exploring the use of PEEM together with a variety of state-of-the-art laser systems for application in ultrafast nano-optics. The work has been carried out in a collaborative effort between the Division of Synchrotron Radiation Research, with expertise in surface science and microscopy, and the Division of Atomic Physics, with expertise in laser science and time-resolved measurements. In addition, specially tailored metallic and semiconducting nanostructures have been supplied by the Institute of Physics at the Chinese Academy of Sciences in Beijing, China, and the Division of Solid State Physics in Lund. The research has had two, partly overlapping, main directions: *i*) to investigate how various novel pulsed light sources can be used for PEEM, and *ii*) to characterize light interaction with different types of nanostructures using PEEM with appropriate light sources.

The thesis is based on seven papers resulting from experiments using five different types of light sources. Paper **I** is about the imaging and control of nanolocalized enhanced electric fields in Ag nanocubes, using pulses from an ultra-broadband laser oscillator. Papers **II**–**III** present studies exploring the spatiotemporal imaging of ultrafast electric field dynamics in metallic nanoantennas using two few-cycle laser pulses with a variable delay.

In Paper **IV**, the use of femtosecond pulses in the telecommunication wavelength range around 1.55 μm together with PEEM is demonstrated. Paper **V** presents the first laser-based PEEM study of semiconductor nanowires, using pulses from an optical parametric amplifier. Finally, Papers **VI**–**VII** are about PEEM using attosecond pulse trains produced by high-order harmonic generation, where Paper **VII** presents the first PEEM images acquired with a novel high-repetition rate high-order harmonic source.

The first part of this thesis consists of seven chapters giving a background to the theoretical concepts and experimental techniques used for the papers. Chapter 2 gives an introduction to the broad field of nano-optics, including plasmonics. Chapter 3 then discusses some theoretical and experimental aspects of ultrashort laser pulses. In chapter 4, various types of photoemission are introduced and lay the foundation for chapter 5, which describes photoemission electron microscopy. Chapter 6 ties together the concepts from the previous chapters to discuss the main experimental results on which the papers are based. Finally, Chapter 7 summarizes and concludes the thesis, and gives a glimpse into the possible future of this and related work. All of the experimental data presented in this thesis are from measurements performed by the author, unless otherwise specified.

Chapter 2

Nanostructure Optics

The research field of nano-optics has seen a tremendous increase in activity during the past couple of decades due to rapid development of both nanostructure fabrication techniques and experimental characterization methods. What makes nanostructures interesting for optics is their subwavelength dimensions, which makes them interact with visible light in a way distinctly different from both macroscopic objects and single atoms. This chapter will give a brief general introduction to nano-optics, starting with a description of the types of structures used in the work behind this thesis. It will then continue by describing how classical electrodynamics can be applied to nanostructure optics.

2.1 Nanostructures

The definition of a nanostructure is a bit of a political issue [20], but typically includes structures with at least one dimension on the scale of approximately 1–100 nm. Fabrication of nanostructures can be done either by the controlled assembly of atoms ("bottom-up"), or by the selective removal of material from a larger object ("top-down"). The bow-tie nanostructures used for Paper **III** were manufactured by milling from a Au film using a focused ion beam, i.e. a top-down technique. The other types of nanostructures used were fabricated using bottom-up methods.

2.1.1 Colloidal silver nanostructures

Papers **I**, **II**, **IV**, **VI**, and **VII** all include studies of Ag nanostructures made in solution. Solution-based methods are often quick, cheap, and simple ways of making nanoscale materials. The particular nanostructures used in the studies presented in the papers were synthesized by the group of Hongxing Xu at the Chinese Academy of Sciences in Beijing, China, using a so-called polyol process. The polyol process can be used for production of a large variety of geometries, such as cubes [21], wires [22], rice [23], and octahedra [24]. It is based on the reduction of a metal salt (e.g. $AgNO_3$) by a reducing agent such as ethylene glycol (which can also work as the solvent) and with the polymer poly(vinyl pyrrolidone) (PVP) acting as a capping agent by binding to selected facets. For example, PVP binds more strongly to {100} facets of Ag than to {111} facets, which can lead to the growth of high-aspect ratio nanowires from multiply twinned seed

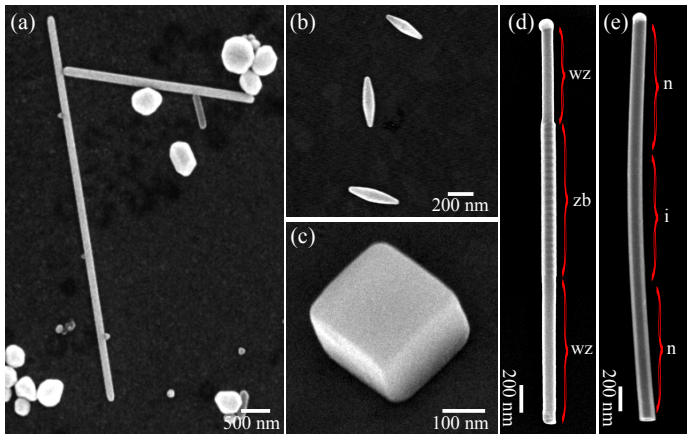

Figure 2.1: SEM images of (a) Ag nanowires and nanoparticles, (b) Ag nanorice, (c) a Ag nanocube (30° tilt), (d) an InAs nanowire with varying crystal structure (5° tilt, image by Sebastian Lehmann), and (e) an InP nanowire with varying doping level.

nanoparticles [25].

The resulting geometry from a polyol process can be controlled through changes in reaction conditions such as temperature and time, through changing the size of the repeating unit in PVP [21], through the use of seed particles [25], or through the addition of chemicals such as NaBr [24]. Figure 2.1 shows scanning electron microscopy (SEM) images of resulting Ag nanowires (a), nanorice (b), and nanocubes (c). The growth mechanisms inherently give the nanostructures a controlled crystallinity, typically with differently oriented single-crystalline domains separated by twin-plane boundaries. On the other hand, the synthesis process also means that the particles may have chemical residues on the surface, altering the surface properties. Furthermore, the positions and orientations of the individual nanostructures on a substrate are difficult to control, resulting in random ensembles of particles. However, for microscopy studies this is of minor importance as individual structures can be identified in the microscope.

2.1.2 Epitaxial III–V semiconductor nanowires

Compound semiconductors made from a stoichiometric mixture of elements from group III (most notably Al, Ga, and In) and group V (most notably N, P, As, and Sb) of the periodic table can have properties far superior to the commonly used semiconductor materials of Si and Ge. However, the III–V materials are much more expensive, and possible combinations of different compounds are limited due to lattice mismatch. A way to overcome both of these problems is by using nanowires, and much of the nanoscience research in Lund during the past decade has therefore focused on the synthesis and application of III–V semiconductor nanowires. Nanowires are typically grown using a vapour-liquid-solid

method [26], where a Au particle is used as a catalyst for the anisotropic epitaxial assembly of material on a semiconductor substrate. This method has in modern days been perfected to produce nanowires with extreme control of materials composition [27], doping [28], and crystal structure [29]. In contrast to their bulk counterparts, III–V nanowires can exist in both the zincblende and the wurtzite crystal structures. The crystal structure can affect properties such as the electronic structure, the morphology, and the symmetry of the wires. Figure 2.1d shows an InAs nanowire with varying crystal structure: the bottom and top segments have the wurtzite structure, while the middle segment has the zincblende structure. Figure 2.1e instead shows an example of varying doping in an InP nanowire. This wire also has three segments, where the bottom and top ones are highly n-doped, and the middle segment is intrinsic (not intentionally doped). In this case, the segments are indistinguishable in the SEM image, as the doping does not affect the morphology of the nanowire.

2.2 Electromagnetic waves at interfaces

After this brief description of the relevant nanostructures, the rest of this chapter will focus on their optical properties from the perspective of classical electrodynamics. Initially, some fundamental concepts of electrodynamics will be described, serving as a starting point for both the rest of this chapter and for chapter 3 about ultrashort laser pulses.

The key quantities in this description are the electric field $\vec{E}$ and the electric displacement field $\vec{D}$, which is related to the induced polarization $\vec{P}$ in a material according to $\vec{D} = \epsilon_0\vec{E} + \vec{P}$. The relations between these fields and their magnetic counterparts are governed by Maxwell's equations, as described in detail in e.g. [30]. This thesis will focus on non-magnetic materials and therefore concentrate on the electric fields. The interaction of light with a material is then in a classical picture fully described by the constitutive relation between $\vec{E}$ and $\vec{D}$. This relation can take many forms depending on the material. In some cases, the relation is a simple scalar ($\vec{D} = \epsilon_0\epsilon\vec{E}$), and the material is said to be linear, homogeneous, isotropic, and non-dispersive. The dielectric constant ϵ is in some cases used interchangeably with the refractive index $n = \sqrt{\epsilon}$. The assumption of a non-dispersive material, however, means that the material response is instantaneous and does not depend on the applied field at any previous instant of time, an assumption which is typically not valid. This temporal dispersion is most easily described in the frequency domain. By Fourier transformation and considering time-harmonic fields, the response of a dispersive material can be described by a frequency-dependent dielectric function[1] $\epsilon(\omega)$, as $\vec{D} = \epsilon_0\epsilon(\omega)\vec{E}$.

From Maxwell's equations follows, in the absence of external charges and currents, the homogeneous wave equation

[1] This is a description of dispersion in time. For spatially dispersive materials, ϵ also depends on the wave vector $\vec{k}$.

$$\nabla \times \nabla \times \vec{E} \;=\; -\mu_0 \frac{\partial^2 \vec{D}}{\partial t^2} \;=\; -\frac{\epsilon}{c^2}\frac{\partial^2 \vec{E}}{\partial t^2}\,, \tag{2.1}$$

where the fundamental constant $c = (\mu_0\epsilon_0)^{-1/2}$ is the speed of light in vacuum and the second step is valid when $\vec{D} = \epsilon_0\epsilon\vec{E}$. Assuming time-harmonic fields and a frequency-dependent $\epsilon(\omega)$, equation 2.1 has solutions in the form of propagating plane waves

$$\vec{E}(\vec{r},t) \;=\; \vec{E}_0 \exp(i(\vec{k}\cdot\vec{r} - \omega t))\,, \tag{2.2}$$

$$\omega \;=\; ck/\sqrt{\epsilon\,(\omega)}\,. \tag{2.3}$$

Equation 2.3 connects the frequency with the wavenumber ($k = |\vec{k}|$) of the propagating wave and is known as the dispersion relation. Equations 2.2–2.3 describe the basics of electromagnetic wave propagation through dispersive media, of central importance both for the remainder of this chapter, and for ultrashort laser pulses (chapter 3).

2.2.1 The dielectric function

The origin of the dielectric function can be traced to electric field-induced excitations in the material. These excitations can be divided into those involving bound electrons and those involving free electrons. The bound electron, or interband, contribution can be treated as an ensemble of harmonic oscillators with resonance frequencies ω_n, damping constants γ_n, and oscillator strengths f_n. This is the Lorentz model of the dielectric function, and takes the form [31]

$$\epsilon_{\text{bound}}\,(\omega) \;=\; 1 + \sum_n \frac{f_n}{\omega_n^2 - \omega^2 - i\omega\gamma_n}\,, \tag{2.4}$$

Equation 2.4 is a good model for dielectrics such as glasses and neutral gases. However, for conductors the contribution from free charges becomes important. Free charges have a very large number of available states within a small frequency range, and can therefore be treated as a Lorentz model with one resonance at $\omega = 0$. This yields the Drude model of a free electron gas, which is the free-electron, or intraband, contribution

$$\epsilon_{\text{free}}\,(\omega) \;=\; 1 - \frac{\omega_p^2}{\omega^2 + i\omega\gamma_0}\,. \tag{2.5}$$

Here the plasma frequency $\omega_p^2 = n_f e^2/\epsilon_0 m$ depends on the free electron density n_f and the free electron effective mass m. For an undamped electron gas ($\gamma_0 = 0$), the plasma frequency represents the transition from negative to positive $\epsilon(\omega)$, i.e. from purely imaginary to purely real propagation constant (see

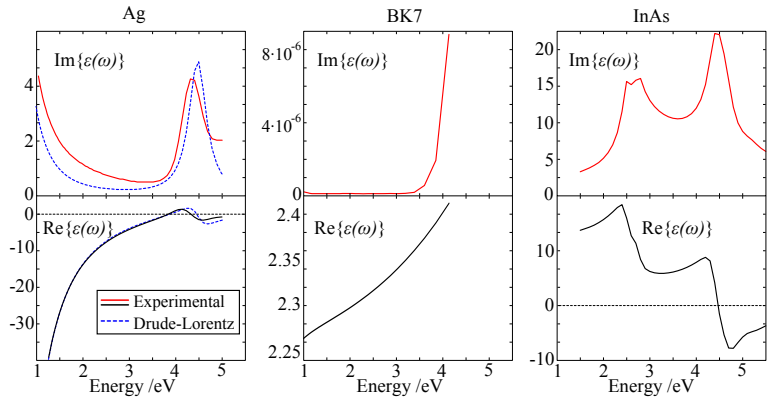

Figure 2.2: Real (lower row) and imaginary (upper row) parts of the dielectric function for Ag [33], BK7 glass [34], and InAs [35]. For Ag (leftmost column), both experimental data (solid lines) and a Drude-Lorentz fit (dashed blue lines) are shown.

equation 2.3). A perfect metal is thus transparent above the plasma frequency, and opaque below. For real metals, the response involves both inter- and intraband transitions, and can be modelled using a combination of equations 2.4–2.5. However, in many cases dielectric functions are instead taken directly from experimentally determined data found in literature such as Johnson & Christy [32] or Palik [33].

The experimentally determined real and imaginary parts of the dielectric function at optical frequencies for the three example materials silver, BK7 glass, and indium arsenide are shown in figure 2.2. For Ag, a fit calculated using a free-electron contribution, a single harmonic oscillator, and a constant contribution ϵ_∞ from higher resonances, is shown for comparison. Fit parameters were obtained from reference [31]. One notable feature of figure 2.2 is the negative real part of the dielectric function for Ag across the whole visible part of the spectrum. Note also the almost constant real part and the very small imaginary part of the dielectric function of BK7, corresponding to the low dispersion and absorption of the material making it a popular choice of glass for optical components.

2.2.2 Boundary value problems

Nanostructures, with their small dimensions, are not homogeneous materials. However, they can in most cases be considered *piecewise homogeneous*, meaning that they can be treated as a finite number of volumes with their own frequency-dependent dielectric functions, separated by sharp boundaries. This approximation is typically valid as long as the dimensions involved are not smaller than a few nanometres [36–38]. The boundary conditions can be derived directly from Maxwell's equations, and state that the electric field $\vec{E}$ and the displacement field $\vec{D}$ at the boundary between materials i and j must fulfil [30]

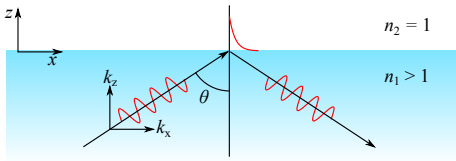

Figure 2.3: Schematic drawing of total internal reflection, showing the exponentially decaying field in the positive half-space.

$$\vec{n} \times (\vec{E}_i - \vec{E}_j) = \vec{0} \tag{2.6}$$

$$\vec{n} \cdot (\vec{D}_i - \vec{D}_j) = \sigma\,, \tag{2.7}$$

where $\vec{n}$ is a unit normal vector and σ is the surface charge density on the boundary. Equation 2.6 requires continuity of the tangential electric field across the boundary, while equation 2.7 tells that the discontinuity of the normal displacement field is equal to the surface charge density. The condition 2.7 then means that the electric field can show sharp discontinuities at interfaces between media with distinctly different $\epsilon\,(\omega)$.

The simplest boundary problem is that of an infinite flat surface dividing space into two homogeneous half-spaces $z < 0$ and $z \geq 0$. At such a boundary, new solutions of the wave equation (2.1) can be found. For example, solutions that are plane waves in the xy plane but exponentially decreasing in the z-direction can exist. These solutions are only permitted at an interface between different materials, as for homogeneous materials an exponentially decreasing solution in one direction would mean an exponentially increasing solution in the opposite direction. An example of a situation where there is an exponentially decaying solution is total internal reflection at a dielectric–vacuum interface at $z = 0$, as schematically shown in figure 2.3. In this case, the incident wave propagates through the dielectric in the negative half-space with a real and positive $k_{z1} = k_1 \cos\theta$. In the positive half-space however, the z-component of the wave vector can be calculated from Snell's law to be $k_{z2} = k_2\sqrt{1 - n_1^2 \sin^2\theta}$. For large enough θ, k_{z2} becomes purely imaginary and the wave decreases exponentially in the z-direction in the positive half-space [39].

Such an exponentially decaying solution is called an *evanescent wave*. Evanescent waves can besides optical waves be, for example, radio waves at the surface of a cellphone antenna, or electron waves in the tip–sample region of a scanning tunnelling microscope. An imaginary component of the wave vector can also facilitate confinement in other directions, as some components of the wave vector can be larger than the norm. For example, if k_z is imaginary, there can be a situation where

$$k_x > k = \sqrt{k_x^2 + k_y^2 + k_z^2}\,. \tag{2.8}$$

A large k_x allows for localization in the x-direction on a scale smaller than the free-space wavelength $\lambda_0 = 2\pi/k$, as seen from the uncertainty relation $\Delta x \geq 2\pi/k_x$ [39]. This is why evanescent waves are so important for nano-optics: they can be localized to volumes smaller than the traditional diffraction limit.

The electric field of an evanescent electromagnetic wave can because of its localization completely dominate the total field within a fraction of a wavelength from the boundary. This region is commonly called the *near-field*[2], as opposed to the far-field consisting of waves unbound to any surface. Near-fields offer new possibilities to concentrate and control waves beyond the diffraction limit, and are of central importance for the work behind this thesis.

Another illustrative example of a boundary value problem is that of a sphere with radius $a \ll \lambda$, excited by a monochromatic plane wave. For such a small sphere, the field of the incoming wave can be assumed to be spatially constant across the structure. This is commonly denoted the quasi-static approximation. The electric fields inside and outside a sphere with dielectric function $\epsilon(\omega)$, can then be calculated analytically. The field along the polarization axis outside a sphere located at the origin and surrounded by vacuum is given by [30]

$$E = E_0 + 2a^3 \frac{\epsilon(\omega) - 1}{\epsilon(\omega) + 2} \frac{1}{r^3} E_0 \, . \tag{2.9}$$

Equation 2.9 tells that there can be an enhanced field close to the surface. For a dielectric sphere with $\epsilon = 2$, the field will be enhanced by a factor of 1.5 just outside the surface of the sphere. However, if $\epsilon \approx -2$ (as e.g. seen for Ag around 3.4 eV in figure 2.2), there can be a resonant enhancement of the electric field. The field described by equation 2.9 is not an evanescent wave, but the sum of the incident field and the field of an electrostatic dipole at the origin.

It was shown in the beginning of the 20th century by Gustav Mie that an analytic solution exists also for the case of larger spheres [40]. In this case, the maths is a bit more complicated as the field variation across the particle must be taken into account. However, by expanding the incoming and scattered fields into vector spherical harmonics, the problem can be solved and the fields calculated inside and outside the particle. The terms in the expansion represent the different multipoles, with the quasi-static approximation corresponding to only including the lowest order term, the dipole. Fig. 2.4 (a) shows a schematic drawing of how the field is enhanced by Ag spheres with diameters of 20, 100, and 200 nm for a wavelength of 400 nm. The field enhancement at the surface calculated from Mie theory including the first 5 orders of the expansion is shown in (b) as a function of polar angle. One can clearly see the transition from purely dipolar behaviour towards including more and more of the quadrupole mode when the particle size increases. Note that a maximum field enhancement of more than a factor of 7 occurs for the 100 nm diameter sphere, corresponding to a local

[2]There is little consensus on the definition of the term "near-field"; while some sources describe the near-field as the total field within a certain fraction of a wavelength from the surface or source, others define it more strictly as the field of evanescent waves.

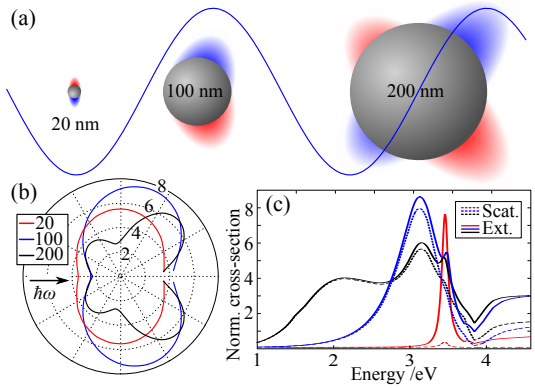

Figure 2.4: (a) Schematic (drawn to scale) and (b) Mie theory calculation of the field enhancement by Ag spheres of different sizes, showing how the enhancement evolves from purely dipolar to mainly quadrupolar as the size of the particle increases. The excitation wavelength is 400 nm, and the wave is propagating towards the right in the plot. Data for the dielectric function of Ag are taken from Johnson & Christy [32]. (c) Calculated scattering and extinction cross-sections for the three particles. The cross-sections are all normalized to the geometrical cross-section of the respective particle. The largest particle is seen to have one broad resonance (dipolar) at approximately 2 eV, and one quadrupolar resonance close to 3.1 eV, which corresponds to the wavelength used in (a–b).

intensity enhancement of about 50. The interaction between particle and field converts the energy either to ohmic losses (absorption) or to far-field radiation (scattering). The sum of these components is referred to as extinction. Scattering and extinction cross-sections of the particles are shown as functions of frequency in figure 2.4 (c). Spectral signatures of the different modes can there be clearly seen as peaks with different heights and widths. For the smallest sphere, the extinction is dominated by absorption and the peak is narrow. For the larger particles, the extinction is instead dominated by scattering and the peaks are broad because of the short radiative lifetime.

2.3 Plasmonics

2.3.1 Propagating surface plasmon polaritons

The special case of nano-optics at the interface between a conductor ($\mathrm{Re}\{\epsilon\} < 0$) and a dielectric ($\mathrm{Re}\{\epsilon\} > 0$) is so important that it has become its own research field, called *plasmonics*. This special treatment is due to a particular type of surface mode inherent to these interfaces: the surface plasmon polariton (SPP). A surface plasmon polariton is a quasiparticle arising from the coupling of a charge density wave (plasmon) in the conductor with an electromagnetic field. If the interface is an infinite, flat surface dividing a conductive half-space $z < 0$ from

a dielectric half-space $z \geq 0$, there can exist solutions for propagating fields bound to the interface. These solutions correspond to SPPs, and take the form [41]

$$\vec{E}\left(\vec{r},t\right) = \begin{cases} \vec{E}_{01}\exp\left(-k_{z1}z\right)\exp\left(i(k_x x-\omega t)\right) & ,\ z \geq 0 \\ \vec{E}_{02}\exp\left(k_{z2}z\right)\exp\left(i(k_x x-\omega t)\right) & ,\ z < 0\ , \end{cases} \tag{2.10}$$

with k_{z1}, k_{z2} real and positive. It can be shown that this surface wave can only exist in transverse magnetic (TM) polarization, where the electric field component of the wave at the surface is in the z-direction. Furthermore, the propagation constant k_x fulfils the dispersion relation

$$k_x \quad = \quad k_0\sqrt{\frac{\epsilon\left(\omega\right)\epsilon_d}{\epsilon\left(\omega\right)+\epsilon_d}}\ , \tag{2.11}$$

where k_0 is the vacuum wavenumber and ϵ_d is the dielectric constant of the dielectric in the positive half-space. As actual metals have a finite imaginary part of $\epsilon(\omega)$, k_x will in practice be complex, leading to a decreasing amplitude of the wave as it propagates. This decrease in amplitude corresponds to resistive heating in the metal. The situation is shown schematically in figure 2.5a, together with the dispersion relation (equation 2.11) for SPPs at the Ag-vacuum interface (b). At low frequencies, the SPP dispersion closely follows the light line $\omega = ck$, to then deviate more and more. The deviation of the SPP dispersion from the light line means that an SPP cannot be directly excited by light due to momentum mismatch. Momentum matching can be achieved using a grating coupler or by illuminating a thin metal film from the back side through a prism. Defects such as edges or curved surfaces can also serve as sources of momentum. The singularity of the SPP wavenumber around 3.6 eV corresponds to a delocalized but non-propagating excitation of the whole surface. This surface mode is what was originally called the *surface plasmon*, as predicted by Ritchie [42] and experimentally demonstrated by Powell [43]. However, since then the term surface plasmon has come to represent many different types of modes. In this thesis, the focus is on localized surface plasmons (LSPs) in low-dimensional systems, with some discussion of the propagating surface plasmon polaritons (SPPs) of figure 2.5.

2.3.2 Localized surface plasmons

LSPs are responsible for the different resonances of metallic spheres seen in figure 2.4. The resonances can be illustrated with a mass-in-a-spring model: the electric field displaces the free electrons, which then feel a restoring force from the positive ionic lattice. Such a system is well characterized by a driven, damped harmonic oscillator with a resonance frequency ω_0 and lifetime τ_l. The lifetime of an LSP is typically between a few and some tens of femtoseconds [44], after which the energy of the LSP is either absorbed by the particle or rescattered into

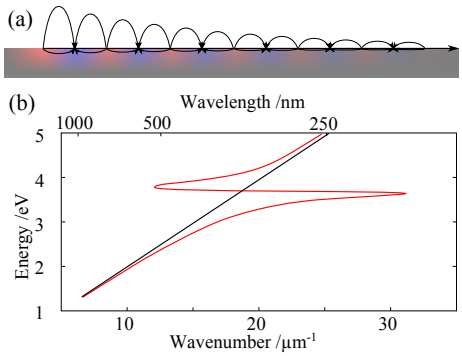

Figure 2.5: (a) Schematic drawing of a propagating SPP at a metal/dielectric interface, with a collective charge oscillation (shaded colours) coupled to an electromagnetic field (arrows). (b) Dispersion relation for SPPs at a planar Ag/vacuum interface (red line). The black line shows the light line $\omega = ck$. SPPs can exist below the surface plasmon frequency of 3.6 eV/$\hbar$.

far-field radiation. Common characterization methods of LSPs therefore measure the scattering and extinction spectra of the particle. As seen in figure 2.4, these can show large differences.

Most physical systems are neither small spheres nor infinite planar surfaces. A simple extension from a sphere is an elongated object such as the nanorice shown in figure 2.1b, which has different resonances along its long and short axes, giving rise to a strongly polarization dependent field enhancement. The longitudinal resonances of such a quasi-1D object can be described as standing waves in one dimension, classified by the number of nodes m [45]. Schematic drawings of charge distributions associated with the first four modes are shown in figure 2.6. The modes are either odd ($m = 1,\ m = 3$, etc., left part) or even ($m = 2,\ m = 4$, etc., right part), and the corresponding charge distribution is an odd or even function of position. This has an important consequence for optical studies. Consider the LSP excitation by a plane wave incident from below in figure 2.6, with a wavelength much larger than the short axis of the particles. In this case, the excitation can be considered as an oscillating, spatially constant field inducing a polarization in the particle. However, the even modes (right part of figure 2.6) are symmetric and not associated with any net polarization (dipole moment) of the particle. These modes can therefore not couple to far-field radiation at normal incidence, and are commonly denoted “dark” [46]. Modes that do have a net dipole moment are correspondingly called “bright”. The even modes can, however, be excited by light if the symmetry is broken, for example, by a substrate or by grazing incidence illumination.

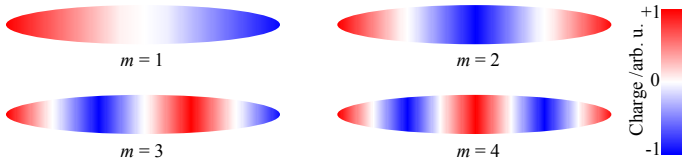

Figure 2.6: Schematic visualization of the four lowest longitudinal modes of an ellipsoidal particle.

2.3.3 Experimental characterization of surface plasmons

Because of the combined optical and electronic nature of surface plasmons, experimental approaches in plasmonics utilize both optical and electronic methods, as well as combinations thereof. The simplest characterization methods are different types of optical far-field measurements, which can accurately determine the scattering and extinction cross-sections, i.e. how well the plasmonic system scatters and absorbs light. Far-field optical spectroscopy can also be used for sensing purposes, for example, in surface enhanced Raman spectroscopy [47, 48]. However, these methods do not give near-field information. This can instead be reached by scanning near-field optical microscopy (SNOM), where a small aperture or sharp tip is used to couple the near-field and far-field [49, 50]. However, this requirement makes the method intrinsically invasive, as the structure coupling to the near-field also disturbs it.

Electronic methods most notably include electron energy loss spectroscopy (EELS), which was the method used for the first experimental proof of surface plasmons [43]. EELS in a transmission electron microscope is still widely employed for LSP characterization due to its high spatial resolution [51–53]. EELS can also be implemented in low-energy electron microscopy (LEEM) [54].

The technique being the topic of this thesis, photoemission electron microscopy (PEEM), combines optical excitation with electronic detection, and is sensitive to the near-field because of the detected electrons all originating from the surface region. The "inverse" method, cathodoluminescence (CL), excites surface plasmons using a focused electron beam and detects emitted radiation [55]. Another technique combining optics and electronics is photon-induced near-field electron microscopy (PINEM), where a laser beam is coupled into a transmission electron microscope for optical excitation of plasmonic nanoparticles [56]. The plasmonic field can then give the imaging electrons an energy shift, which can be detected by electron energy gain spectroscopy. As these experimental methods use different ways of excitation and detection, they will measure different properties. EELS, for instance, characterizes plasmon modes independently of their dipole moment, while CL only detects modes that radiate into the far-field [57]. PEEM can characterize both bright and dark modes [58], depending on the geometry of the combined system of excitation source and sample.

2.4 Numerical field simulations

Solutions to Maxwell's equations can, as described in the previous sections, be found analytically for a few simple geometries, such as planar surfaces, spheres, and spheroids [59]. In most cases however, analytical solutions are not available and numerical methods need to be employed. These have recently become widely available and applicable to more and more complicated problems due to the rapid decrease in the cost of computational power. User-friendly software implementations have also contributed to the popularity of numerical field simulations such as the finite element or finite-difference time-domain methods.

2.4.1 The finite-difference time-domain method

A brute-force method for obtaining numerical solutions to Maxwell's equations is by discretization of space and time into small elements, and approximation of the derivatives by finite differences. This method, introduced by Yee in 1966 [60], is known as the finite-difference time-domain (FDTD) method. It can be applied to a large variety of problems involving the propagation of electromagnetic waves, and has become something of a standard method for simulations in nano-optics. A geometry from a typical FDTD simulation is shown in figure 2.7a.

In FDTD calculations, the simulation space is typically discretized into rectangular elements, meaning that all objects are approximated by a staircase-type surface consisting only of elements with their faces along the main coordinate axes (see inset of figure 2.7a). Each element is described by its dielectric function, and for magnetic materials also its magnetic permeability. The boundary conditions (equations 2.6–2.7) are then implicitly fulfilled when solving the problem [61]. The electric and magnetic fields are calculated for each point in space using the discretized approximations of Maxwell's equations and the defined initial values. These fields are then used as input values for calculating the fields in the next time step. This method is quite memory demanding due to the 4-dimensional space-time grid. For example, if a $1\,\mu m^3$ simulation space is divided into $1\,nm^3$ elements, and the simulation is performed during 100 fs with a time step of 10 as, the fields need to be calculated in 10^{13} points. With 6 field components and assuming a numerical precision of 64 bits, such a calculation gives hundreds of terabyte of data. For this reason, FDTD algorithms typically only save the fields within certain pre-defined sensors, and with down-sampled time intervals.

The calculated fields can also be used to extract the radiated and absorbed powers and thus the scattering and extinction cross-sections. Spectral information is extracted from the simulations by Fourier transformation and normalization by the excitation spectrum. The use of a 4-dimensional space-time grid thus gives the response to all frequencies in one simulation, which is not the case for the finite element method (FEM), with which the fields need to be calculated for each frequency separately. Examples of spectral information extracted from FDTD simulations are shown in figure 2.7b–d, using ellipsoidal nanoparticles on a glass substrate as an example system. The absorption cross-section (a) shows distinct peaks corresponding to the different longitudinal modes described in fig-

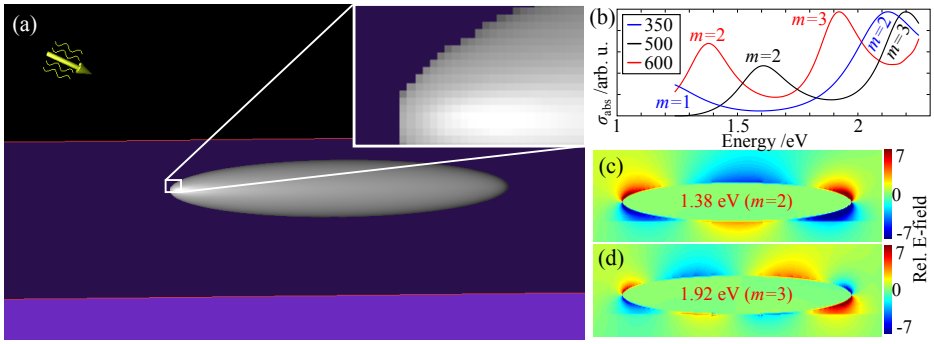

Figure 2.7: (a) Setup for FDTD simulation of a laser pulse interacting with an ellipsoidal Ag nanoparticle on a substrate. (b) Calculated absorption spectra of three different particles, whose lengths (in nm) are indicated in the inset. (c–d) Steady-state field distributions in a cross-section through the particle of 600 nm length at frequencies corresponding to the $m = 2$ and $m = 3$ modes, respectively. These simulations were used for Paper **II**.

ure 2.6. These peaks shift to lower energies for longer particles, in accordance with the standing-wave picture. Figure 2.7c–d show the steady-state field distributions for the 600 nm long particle, evaluated at two frequencies corresponding to the $m = 2$ and $m = 3$ modes. These particular simulations are also presented in Paper **II**, but FDTD simulations were used for all of the Papers **I**–**III** and **V**. All of these simulations were performed using the commercial software FDTD Solutions from Lumerical.

Chapter 3

Ultrashort Laser Pulses

Concentrating light into extremely short pulses is desirable for two main reasons: the light can reach very high peak powers, and the bursts can be used as ultrashort flashes for time-resolved studies. This chapter will give an introduction to femtosecond laser pulses, their generation and amplification, and how they can be used to generate attosecond pulses. It will also contain brief descriptions of the laser systems used for the experiments behind this thesis. The focus will be on the application of the laser systems as light sources for PEEM. For more complete descriptions of the different laser systems used, see [62, 63].

3.1 Basic description of short pulses

To produce a short burst of light, many monochromatic waves with different frequencies need to be coherently added. This concept is illustrated in figure 3.1, where 21 monochromatic waves with wavelengths reaching from 650 to 1050 nm are shown (a), together with their coherent superposition (b). Figure 3.1c shows the corresponding temporal intensity and phase, to be introduced later. From the temporal intensity envelope it is possible to measure the pulse duration to be 5.1 fs. Because short pulses can be described as superpositions of monochromatic waves, the electrodynamics of time-harmonic waves described in the previous chapter is also valid for short pulses as long as the response of the medium can be considered linear.

For the PEEM experiments described in this thesis, the area of interest on the sample is typically much smaller than the focal spot of the laser beam. Therefore, the spatial properties of the laser beam can be well approximated by a plane wave, and this chapter will therefore focus on the time–frequency characteristics. The starting point in this basic mathematical description is a linearly polarized laser pulse, which at a fixed point in space can be described by a time-varying complex electric field according to

$$\vec{E}(t) = U(t)\,\vec{e}\exp(i\omega_0 t)\exp(i\varphi(t)), \tag{3.1}$$

where $U(t)$ is the real scalar field envelope[1], $\vec{e}$ a unit vector in the polarization direction, ω_0 the centre frequency, and $\varphi(t)$ the temporal phase.

[1] For a Gaussian pulse with a full-width at half maximum (FWHM) duration Δt of the intensity envelope, $U(t) = U_0 \exp\left(-2\ln 2\, t^2/\Delta t^2\right)$.

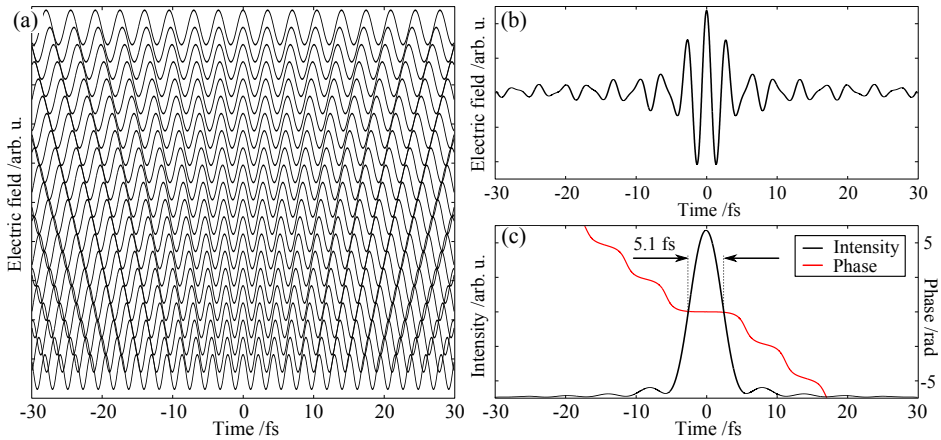

Figure 3.1: (a) Time-dependent electric field of 21 different monochromatic waves with wavelengths spanning from 650 nm (bottom) to 1050 nm (top). (b) Sum of all the waves in (a), corresponding to a very short burst of light. (c) Intensity and phase corresponding to the electric field shown in (b), showing a pulse duration of 5.1 fs. As the waves in (a) were added with equal weight, the spectrum of the resulting pulse has a rectangular shape. Therefore, the intensity envelope seen in (c) is a sinc^2 function, the Fourier transform of a rectangular spectrum.

The temporal description of an ultrashort laser pulse is practical for providing an intuitive picture of how the electric field behaves. However, for manipulation of the pulse properties a frequency representation is much more convenient due to the wide range of ways to selectively manipulate certain frequencies of the field. The frequency-domain description of the field is the Fourier transform of the temporal field, and can be written as

$$\vec{E}(\omega) \quad = \quad \int \vec{E}(t) \exp(-i\omega t)\, \mathrm{d}t \quad \equiv \quad A(\omega)\, \vec{e} \exp(i\phi(\omega)) \ , \tag{3.2}$$

characterized by the spectral envelope $A(\omega)$ and the spectral phase $\phi(\omega)$. For mathematical convenience, the rest of this chapter will assume a Gaussian pulse, for which both the temporal envelope $U(t)$ and the spectral envelope $A(\omega)$ are Gaussian functions. The duration Δt and the spectral width $\Delta\omega$ are usually defined as the full-width at half maximum (FWHM) of the respective intensity envelopes. Through the Fourier transform it is possible to show that the widths of the spectral and temporal envelopes of a Gaussian pulse fulfil the relation

$$\Delta\omega\Delta t \quad \geq \quad 4\ln 2 \quad \approx \quad 1.82 \text{ eV fs}/\hbar \ . \tag{3.3}$$

This quantity is called the *time–bandwidth product* and is of central importance for short laser pulses. It is the quantitative measure of the inverse relationship

between duration and spectral width, illustrated in figure 3.1. As an example, a Gaussian pulse of 5 fs duration must have a spectral width of at least 365 meV. For a pulse of 100 as duration, the corresponding minimum spectral width is 18 eV, which means that the central frequency of such a pulse must be in the UV to X-ray region of the electromagnetic spectrum.

If the time–bandwidth product is minimized, the pulse reaches its shortest possible duration given a certain spectral width, and is said to be Fourier limited. The pulse is Fourier limited if the spectral phase $\phi(\omega)$ depends linearly on the frequency. The spectral phase is typically described by its Taylor expansion around the central frequency ω_0, as

$$\begin{aligned} \phi(\omega) &= \phi(\omega_0) + \sum_n \frac{1}{n!} \left.\frac{\partial^n \phi}{\partial \omega^n}\right|_{\omega=\omega_0} (\omega - \omega_0)^n \\ &= \phi_0 + \sum_n \phi_n (\omega - \omega_0)^n , \end{aligned} \tag{3.4}$$

where a change in the zero-order term introduces a shift of the carrier-envelope phase (CEP), a change in the first-order term a temporal delay, and a change in the second-order term a linear ramp in instantaneous frequency with time. This linear ramp in instantaneous frequency is called a linear *chirp*, and plays a central role in working with short laser pulses. Correspondingly, higher-order terms in equation 3.4 are referred to as higher-order chirp. Examples of Gaussian pulses with different CEP and chirp are shown in figure 3.2.

3.1.1 Pulse propagation through dielectric media

The propagation of a plane wave through a linear, homogeneous, and isotropic medium is described by equations 2.2–2.3. In the spectral domain, propagation by a distance L through the medium transforms the field $\vec{E}(\omega, x = 0)$ to

$$\vec{E}(\omega, x = L) = \exp(ik(\omega) \cdot L)\, \vec{E}(\omega, x = 0) , \tag{3.5}$$

where $k(\omega) = \sqrt{\epsilon(\omega)} k_0$ is the wavenumber of the propagating wave in the medium (k_0 is the vacuum wavenumber). For a perfect dielectric (non-absorbing) medium, $k(\omega)$ is real and only the phase of the wave changes upon propagation. The wavenumber in the medium can thus be seen as the accumulated spectral phase per unit length, and its effect on the pulse is also commonly expressed in a Taylor expansion around the central frequency, as

$$k(\omega) = k(\omega_0) + \sum_n \frac{1}{n!} \left.\frac{\partial^n k}{\partial \omega^n}\right|_{\omega=\omega_0} (\omega - \omega_0)^n . \tag{3.6}$$

In analogy to equation 3.4, if $k(\omega)$ is constant the pulse only changes its CEP upon propagation through the medium. The linear term $\partial k / \partial \omega$ (units of s/m)

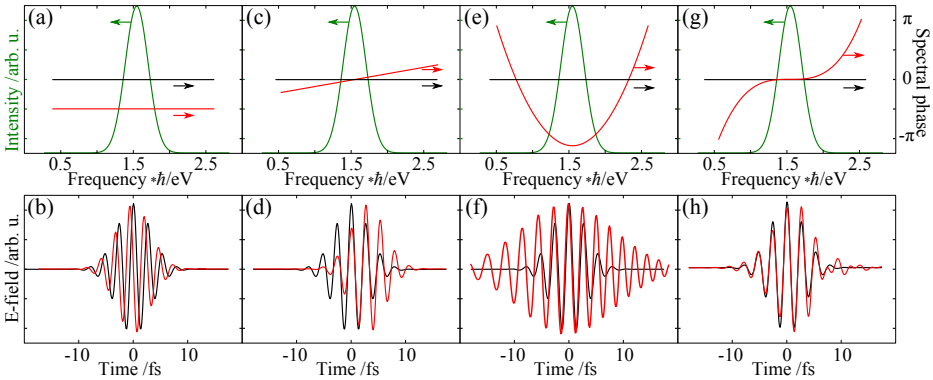

Figure 3.2: Examples of Gaussian pulses with different parameters, described in the upper row by their spectral intensity (green curves) and phase (red and black curves), and in the lower row by their time-dependent electric fields. (a–b) Fourier limited, 5 fs Gaussian pulses with a constant offset in spectral phase, corresponding to a $\pi/2$ CEP offset. (c–d) Pulse with the same spectral envelope, but with a linear variation of the spectral phase, corresponding to shift in time. In all cases, the spectral phase and electric field of the pulse corresponding to $\phi(\omega) = 0$ are shown in black for reference. (e–f) The pulse from (a–b) with a GDD of 25 fs^2, stretching the pulse to 14 fs duration. (g–h) The pulse from (a–b) with a TOD of 40 fs^3, resulting in a distorted electric field.

corresponds to a temporal delay per unit length of medium, which is the inverse group velocity ($v_g = \partial\omega/\partial k$). The group velocity is thus related to the refractive index as

$$v_g = \left(\frac{\partial k}{\partial \omega}\right)^{-1} = \frac{c}{n(\omega) + \omega\, \partial n/\partial \omega}\,. \tag{3.7}$$

From equation 3.7, it can be seen that for a medium with $n(\omega) = const.$, the group velocity v_g reduces to c/n, the phase velocity of a monochromatic wave. If the group and phase velocities are the same, the carrier wave and the envelope travel at the same speed and the pulse does not change its shape upon propagation.

The coefficient for the quadratic part of the Taylor expansion in equation 3.6 ($1/2\ \partial^2 k/\partial\omega^2$, units of s^2/m) is called the group velocity dispersion, and introduces a linear chirp to the pulse propagating through the medium. The second-order dispersion induced by propagation of a length L is called the group delay dispersion (GDD). Higher-order terms of $Lk(\omega)$ are called third order dispersion (TOD), fourth order dispersion, and so forth. The effect of the different terms of equation 3.6 on a few-cycle pulse is illustrated in figure 3.2. As long as k is a linear function of ω, the pulse remains undistorted (except for the CEP) by the medium. However, higher-order terms can cause major distortions of the pulse shape. The 25 fs^2 of GDD stretching the pulse in figure 3.2e–f corresponds to

propagation through 0.7 mm of fused silica glass, or approximately 1.2 m of air. It is therefore crucial to carefully compensate for any dispersion introduced by optical elements in order to keep a well-defined, short pulse.

3.1.2 Dispersion control

The importance of dispersion control depends on the bandwidth of the pulses used. For example, a Fourier limited Gaussian pulse of 35 fs duration centred around 800 nm would have a duration of 36 fs after passing through 3 mm of fused silica glass, corresponding to the entrance window of the vacuum chamber used for PEEM experiments. A pulse originally of 5.5 fs duration would instead be stretched to 55 fs upon propagation through the same piece of glass. Precise control of the spectral phase of the pulse is therefore much more important for the few-cycle pulses used in Papers **I**–**III** and **V** than for the longer pulses used in Papers **IV** and **VI**.

Virtually all transparent materials have a refractive index that is a convex function of frequency in the visible part of the spectrum. This means that $\partial^2 k/\partial\omega^2 > 0$, and the material is said to have positive dispersion. This positive dispersion can be compensated for by creating a setup where light of lower frequency travels a longer path. Such a setup can be built using prisms, or as done in the majority of the work behind this thesis, using chirped mirrors. A chirped mirror is a mirror with a multilayer coating designed to reflect different wavelengths at different depths in the material. A lot of research has been focused on manufacturing chirped mirrors for optimum shaping of the spectral phase since the 1990s [64]. Appropriate chirped mirrors can be combined with a pair of glass wedges, with which it is possible to continuously adjust the amount of glass in the beam. Using this combination together with proper pulse characterization methods, we were able to get a pulse duration of 5.5 fs on the sample for the experiments presented in Papers **I**–**III**.

3.2 Sources of femtosecond pulses

3.2.1 Mode-locked oscillators

The generation of femtosecond laser pulses poses two main challenges: producing coherent radiation across a sufficiently large spectral bandwidth, and controlling the spectral phase so that the frequency components coherently add up to a short burst of light. Both of these criteria can be met by mode-locked Ti:sapphire oscillators, which have made femtosecond light sources become readily available during the past 30 years[2]. The use of Ti:sapphire as a gain medium has several advantages, with the main one being the large gain bandwidth. In this way, a laser cavity with a Ti:sapphire crystal as the gain medium can support a large

[2]Most femtosecond oscillators produce pulses with durations of several tens of femtoseconds, while oscillators delivering few-cycle pulses have only been around for 10–15 years due to the improved dispersion control.

number of modes spanning a wavelength range between approximately 650 and 1050 nm. If the phases of all these modes are locked to each other, the sum of the modes corresponds to a femtosecond pulse, as shown previously in figure 3.1. Mode-locking is typically achieved by deliberately making the laser cavity slightly unstable in the linear regime, while being stable for ultrashort pulses due to Kerr lens focusing (an effect of the intensity-dependent refractive index) in the Ti:sapphire crystal. When properly mode-locked, a single pulse travels back and forth in the cavity, is amplified each time it passes the crystal, and emits a short burst each time it hits the output coupler. This leads to a repetition rate (number of pulses per unit time) of a mode-locked oscillator of $f_{rep} = c/l$, where l is the length of one round-trip. In most oscillators, $l \approx 3.75$ m, corresponding to a repetition rate of 80 MHz. An ultra-broadband Ti:sapphire oscillator was used as a light source for the experiments presented in Papers **I**–**III**, and Ti:sapphire oscillators were also used for seeding the amplifiers used for Papers **IV**–**VII**.

3.2.2 Chirped-pulse amplification

Amplification of femtosecond pulses is challenging due to mainly two effects: heat accumulation in the gain medium, and unwanted nonlinear effects such as self-focusing. The way to circumvent overheating of the gain medium is to reduce the repetition rate of the laser system. However, to minimize the influence of unwanted nonlinear effects, the peak intensity needs to be lowered. This is done by stretching the pulse in time before amplification, to later re-compress it. The stretching and re-compression can be done using, for example, gratings or chirped mirrors. This technique of stretching, amplification, and compression is usually called chirped-pulse amplification (CPA), and has become a widespread technique for production of intense femtosecond pulses. However, the technique is typically limited to repetition rates below 10 kHz due to heat accumulation. Furthermore, the bandwidth of the pulse gets narrower for each amplification step because of the central frequencies always being amplified more than the peripheral ones. This gain-bandwidth narrowing in practice sets a lower limit of ∼20 fs for the pulse duration, and post-compression techniques must be employed to reach even shorter pulses. A CPA system delivering pulses of 30 fs duration at a repetition rate of 1 kHz was used for the experiments presented in Papers **IV** and **VI**. A simplified schematic of this system is shown in figure 3.3.

3.2.3 Optical parametric amplifiers

The main principle behind optical parametric amplification (OPA) is difference-frequency generation (DFG). This effect occurs when two light waves (with $\omega_1 > \omega_2$) interact with a medium and send out a third wave whose frequency is the difference between those of the incoming waves ($\omega_3 = \omega_1 - \omega_2$). Energy conservation is reached by emission of an additional wave at ω_2, effectively amplifying this field. A fundamental difference between OPA and laser amplification is that OPA utilizes excitations to virtual states in the medium. This leads to

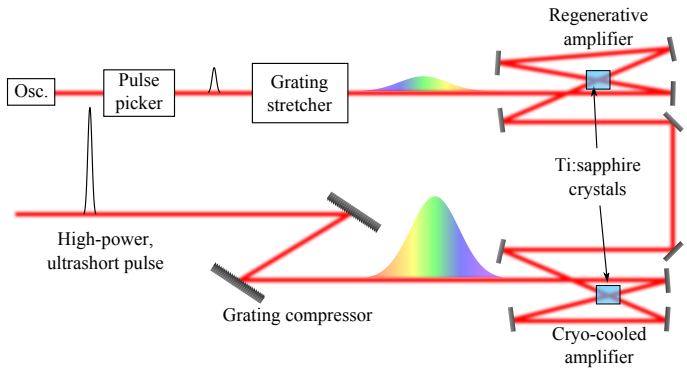

Figure 3.3: Simplified drawing of the CPA system used for Papers **IV** and **VI**. One pulse per millisecond is selected from the oscillator (Osc.) for amplification, stretched in time, amplified in two steps, and then compressed to a short duration again.

two of the main advantages of OPA: first, the energy and bandwidth of the amplified spectrum do not depend on specific laser transitions. Second, the energy difference between the pump and signal photons is released as an auxiliary light wave (called the "idler" wave), instead of as phonons heating the gain medium. Schematic energy diagrams comparing optical parametric amplification to laser amplification are shown in figure 3.4.

On a microscopic level, the gain in an OPA system is determined by the second order nonlinear susceptibility of the interaction medium. However, for efficient amplification on a macroscopic level, the microscopic components of the amplified signal need to be added in phase. This phase-matching condition can also be expressed as the combination of energy and momentum conservation, i.e. as the two relations

$$\omega_{\text{pump}} = \omega_{signal} + \omega_{idler} \tag{3.8}$$

$$\vec{k}_{\text{pump}} = \vec{k}_{signal} + \vec{k}_{idler} \, . \tag{3.9}$$

Special care is required for amplification of broadband pulses, as the relations 3.8–3.9 must be valid across a large frequency range. There are multiple ways to accomplish this, one of the most effective being a non-collinear geometry. The non-collinear geometry further has the advantages of spatial separation of the outgoing beams, including any beams generated in the medium through unwanted wave mixing processes [62, 65]. Using a non-collinear geometry where the pump and signal beams propagate with a 2.4° angle with respect to each other, efficient phase matching for optical parametric amplification in beta-barium oxide (BBO) crystals can be accomplished for a bandwidth exceeding 0.75 eV (400 nm around 800 nm central wavelength) [65].

Two different setups for optical parametric amplification were used throughout this work: one to produce amplified few-cycle pulses at high repetition rate

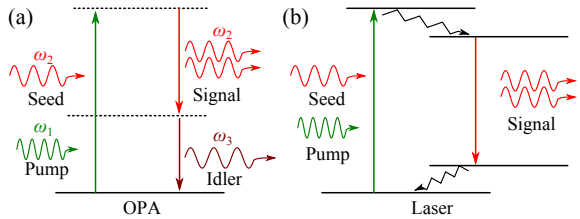

Figure 3.4: Energy diagram comparison of optical parametric amplification and laser amplification. (a) Schematic visualization of the difference-frequency generation (DFG) process utilized in OPA. Two photons with frequencies ω_1 and ω_2 interact with a material, emitting a new photon with frequency $\omega_3 = \omega_1 - \omega_2$ and one with frequency ω_2 via transitions to virtual energy levels. The process of DFG therefore amplifies the signal at frequency ω_2, and creates an idler beam with frequency ω_3. (b) Schematic visualization of laser amplification in a four-level system, for comparison with (a). In the case of laser amplification, the involved energy levels are real and only two frequencies are involved as energy is transferred from the pump beam to the signal beam. The energy difference between pump and seed photons is instead lost as phonons in non-radiative transitions. These phonons (heat) in the laser crystal then need to be cooled away.

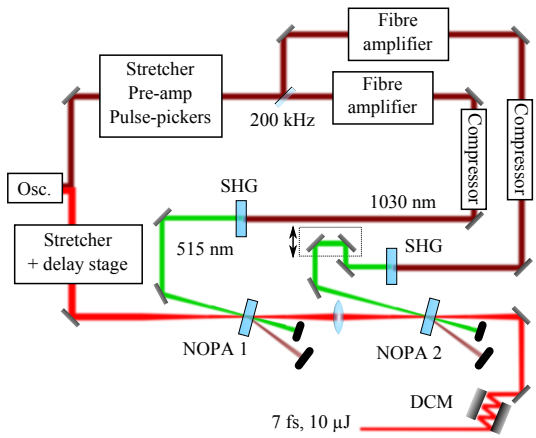

Figure 3.5: Simplified drawing of the OPCPA system used for Papers **V** and **VII**. The oscillator (Osc.) beam is split into two, where part of the spectrum around 1030 nm is used to seed two fibre amplifiers. The amplified infrared pulses are then converted to green light through second harmonic generation (SHG), and used to pump two non-collinear optical parametric amplification (NOPA) stages, where the remaining broad spectrum around 800 nm from the oscillator is used as the seed. Finally, the long pulses are compressed by a pair of double chirped mirrors (DCM).

(Papers **V** and **VII**), and one to produce femtosecond pulses at 1.55 μm wavelength (Paper **IV**). A simplified sketch of the setup for the high-repetition rate system is shown in figure 3.5. For a more complete description of this system, see [62, 65, 66]. The pump pulse in this setup is the second harmonic of the output from two ytterbium-doped fibre amplifiers seeded by part of the oscillator spectrum. As the amplification bandwidth in the Yb-doped fibres is relatively small, the pump pulse reaches a duration of hundreds of femtoseconds. For optimum overlap in the nonlinear crystal used for parametric amplification, the seed pulse is stretched to a similar pulse duration. This also keeps the peak intensity in the crystals at a level where unwanted nonlinear effects are not too prominent. This optical parametric chirped-pulse amplification (OPCPA) system amplifies a seed pulse from an ultra-broadband Ti:sapphire oscillator in two stages[3], both based on difference-frequency generation in a non-collinear geometry in BBO crystals. The system is quite sensitive to fluctuations because of the requirement that the pulses meet in space, time, and angle in the crystals. Active stabilization of the relative position, angle, and temporal delay of the pulses is therefore necessary in order to reach stable experimental conditions.

The optical parametric amplification system used for the experiments presented in Paper **IV** is based on white light generation followed by parametric amplification of a selected part of the white light spectrum. The system is manufactured by Light Conversion Ltd. and goes by the acronym TOPAS (Travelling-wave Optical Parametric Amplification of Superfluorescence). It was used together with the 1 kHz CPA system described in section 3.2.2.

3.3 Interaction of short pulses with nanostructures

The formalisms from this and the previous chapters can be combined to describe the ultrafast response of a plasmonic nanostructure to a femtosecond pulse. The plasmonic response can, with careful tailoring of both the nanostructured system and the excitation pulse, be used to simultaneously control the near-field on a nanometre and femtosecond scale [67–70]. In the quasi-static limit, the electric field near a nanostructure can be described by a local impulse response function, which can be used to calculate the response to an arbitrary excitation [71, 72]. An illustrative example is the small metallic sphere for which the magnitude of the electric field at a fixed position just outside the surface can be described by equation 2.9, which can be slightly rewritten to take the form

$$E(\omega) = \left\{1 + 2\frac{\epsilon(\omega) - 1}{\epsilon(\omega) + 2}\right\} E_0(\omega) \equiv T(\omega) E_0(\omega) , \tag{3.10}$$

with $T(\omega)$ being the impulse response function. Assuming a Drude-Lorentz approximation of the dielectric function for Ag (section 2.2.1), the electric field can be calculated for excitation by a short pulse. Two different cases are shown in figure 3.6. Both excitations have the same Gaussian spectrum centred around

[3]This system was recently upgraded to now work with three amplification stages.

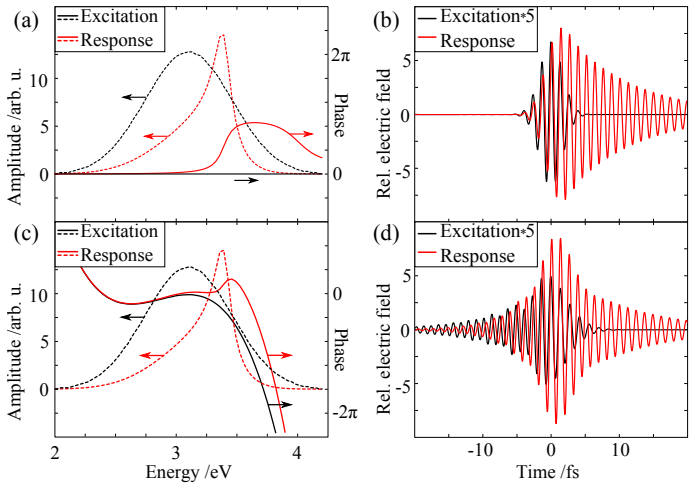

Figure 3.6: (a,c) Spectral, and (b,d) temporal characteristics of the excitation source (black lines) and the resulting electric field at a small Ag sphere (red lines) for two different pulses. (a–b) shows a Fourier limited excitation pulse, which gives a transient response, while (c–d) is for a pulse with quadratic and cubic spectral phase applied to achieve a more symmetric near-field pulse.

3.1 eV, but with different spectral phase: either Fourier limited (a–b) or with $\phi_2 = 6$ fs^2 and $\phi_3 = 17$ fs^3 (c–d). Shaping the phase of the excitation pulse to compensate for the inherent phase of the nanosystem in this case yields a more symmetric and slightly more intense near-field pulse (d) than what is achieved with a Fourier limited pulse (b). This is an important aspect of ultrafast nano-optics: how the temporal (and/or spatial) characteristics of the near-field can be designed by changing the phase of the input pulse.

This input–output formalism can be applied for any quasi-static plasmonic system, which means that the plasmon response of these systems is fully characterized by a spatially varying impulse response function. Beyond the quasi-static approximation, the excitation field can vary across the nanosystem. However, an extension of equation 3.10 to include retardation effects is not straightforward, as the response at one point can depend on the excitation at a different point, and the impulse response can no longer be considered local. A full characterization of the plasmonic system would then instead yield a functional connecting the spatially varying excitation field with the spatially varying near-field response.

3.4 High-order harmonic generation

A fundamental limit of a light pulse is that its duration cannot be shorter than the period of its carrier wave. This requirement can also be understood from the central frequency of a pulse always being at least half its bandwidth, to-

gether with the time-bandwidth product of equation 3.3. Therefore, a visible or infrared laser pulse can never be made shorter than a few femtoseconds. To create even shorter bursts of light, one thus needs a source of coherent radiation in the ultraviolet or X-ray regime. However, UV or X-ray lasers are challenging to realize due to the short upper-state lifetimes making it difficult to obtain a population inversion. Free electron lasers have lately emerged as a promising way to accomplish this, but they are bulky, expensive, and have so far been based on amplified spontaneous emission, leading to an uncontrolled time structure of the pulses. Relatively cheap and compact alternatives[4] are high-order harmonic sources, which are based on the highly nonlinear interaction of a strong laser field with matter. High-order harmonic generation (HHG) was first observed in the late 1980s [10, 11], and has since led to the emergence of attosecond science [73, 74]. The following section will give a brief introduction to the theory of HHG, as well as some practical experimental concerns. It will also describe the two HHG setups used in the work behind this thesis: one used together with the 1 kHz CPA system schematized in figure 3.3, and one used with the 200 kHz OPCPA system (figure 3.5).

3.4.1 HHG by a single atom

A basic understanding of high-order harmonic generation can be gained from a semiclassical three-step model, shown schematically in figure 3.7a–c. HHG can occur when an atom is subjected to a laser field with a strength comparable to that of the Coulomb potential binding the electrons to the nucleus. An electron then has the possibility to tunnel through the barrier formed by the distorted atomic potential, and out to the continuum (figure 3.7a). Once in the continuum, the electron is accelerated by the laser field along a trajectory that depends on the instant of tunnelling (figure 3.7b). In some cases, the trajectory leads back to the parent ion where the electron can relax into its previous state, releasing its excess energy as a photon (figure 3.7c). Energy conservation in combination with the inversion symmetry of the atom and field dictate that the frequency of an emitted photon is an odd multiple of the fundamental frequency. The trajectory of the electron in the continuum can be calculated classically, and some of these trajectories are shown in figure 3.7d for HHG by a long driving pulse. The return energy of the electron along a certain trajectory is colour-coded, with the blue trajectories corresponding to the highest return energy. As seen in the figure, there are two different trajectories for each return energy, one long and one short. It can also be seen that for the short trajectory, light of lower energy (red curves) is emitted before light of higher energy (blue curves), and the resulting radiation will have a positive chirp. The opposite holds for the long trajectory, for which the higher-energy light is emitted first. This has consequences for phase-matching and shaping of the resulting radiation.

[4] To be fair, almost anything is cheap and compact when compared to an X-ray free electron laser; the European XFEL will measure 3.4 km in length and cost an estimated 1.2 billion euro.

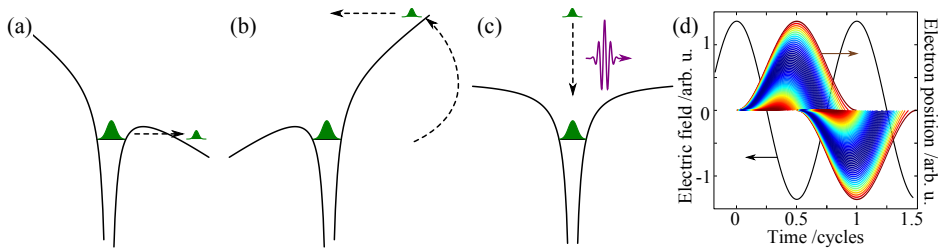

Figure 3.7: Schematic visualization of the three-step model of HHG. (a) In step 1, part of the electron wave packet tunnels through the distorted Coulomb potential and out into the continuum. (b) In step 2, the free part of the electron is accelerated by the laser field. (c) Step 3 is the radiative recombination which can occur if the electron trajectory through the continuum leads back to the parent ion. (d) Classically calculated electron trajectories for different tunnelling times. The colour of each trajectory represents the energy of the electron when it returns to the parent ion, with blue corresponding to the highest energy.

This three-step model was introduced in 1993 [75, 76], and can reproduce the basic features of radiation from HHG. It especially reproduces the perhaps counter-intuitive plateau region where the harmonics have similar intensity. A schematic of a typical HHG spectrum is shown in figure 3.8. Harmonics up to approximately 31, corresponding to a photon energy of 48 eV, can be routinely generated by focusing pulses from the CPA laser system shown in figure 3.3 into a gas cell filled with argon.

A harmonic spectrum such as the one in figure 3.8 can with proper dispersion control correspond to a train of pulses whose duration is a fraction of the optical cycle of the driving field, possibly reaching below 100 attoseconds. Such attosecond pulse trains (APTs) have during the past decade been used to measure, for example, ionization time-delays in rare gases [6, 77] or dynamics of double ionization [78] on the attosecond time scale. APTs were used as a light source for PEEM experiments for Papers **VI**–**VII**.

3.4.2 HHG by a macroscopic gas volume

The three-step model describes the interaction between a laser field and a single atom. For efficient HHG in a macroscopic volume of gas, the relative phase of the radiation emitted by different atoms must be matched. This is visualized in figure 3.9a, schematically showing the harmonic emission from many atoms in a loose-focusing geometry. For all of the high-order harmonic radiation to be emitted in phase, the velocity of the XUV radiation and the driving pulse must be the same through the medium. This can be accomplished thanks to the negative dispersion of plasmas. By careful tuning of the gas pressure and the level of ionization, phase-matching can be achieved as the positive dispersion of the neutral gas is compensated for by the negative dispersion of the free electrons.

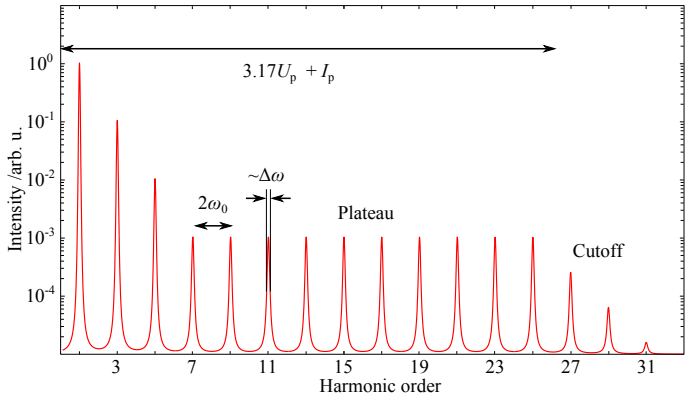

Figure 3.8: Schematic of a typical HHG spectrum. The intensity decreases rapidly with energy for the lower harmonics, to then stay approximately constant in the plateau region. This region is then followed by a sharp cutoff.

This requirement of just the right amount of ionization leads to a non-monotonous dependence of the HHG yield on incident laser power; if the power is increased too much, the gas becomes too ionized and the phase matching conditions will no longer apply. It can be shown that the phase matching conditions differ for the long and short trajectory, and that phase matching for the short trajectory in the propagation direction leads to phase matching in other directions for the long trajectory [79]. This results in the radiation emitted by the long trajectory being more divergent than that from the short trajectory, which makes it possible to select the emission from the short trajectory using a hard aperture. This is important for obtaining a well-defined time structure of the radiation.

Because of the Goldilocks effect in the intensity dependence of HHG, the intensity of the harmonics cannot always be increased by simply increasing the power of the incident pulse. A change in pulse power must instead be accompanied with a change in both the focusing geometry and the gas pressure in the interaction region [80]. HHG by high-power lasers is therefore typically performed in loose-focusing geometries, while a tight-focusing geometry is needed to reach the necessary intensities when working with low pulse energies. In the HHG setup used with the 200 kHz OPCPA system, the pulses were therefore focused with a focal length of 5 cm (schematically depicted in figure 3.9b), while the pulses from the 1 kHz CPA system were focused using 50 cm focal length (figure 3.9a). The gas was also injected in different ways in the two setups, as shown in the figures.

With phase-matching accomplished and the radiation from the short trajectory selected, two challenges remain: filtering out the strong driving pulse used for generation, and compensating for the positive dispersion inherent to the HHG process. Both of these goals can be accomplished by a thin metallic film, which is transparent and exhibits negative dispersion above its plasma frequency (as mentioned in section 2.2.1). The workhorse setup in Lund during the past years

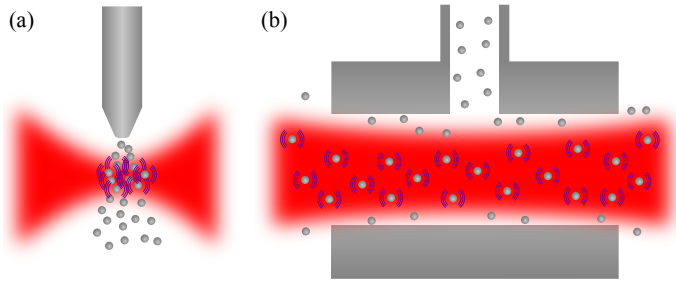

Figure 3.9: Schematic drawings of HHG in (a) tight-focusing and (b) loose-focusing geometries. The picture shown in (a) is representative of the HHG setup used together with the 200 kHz OPCPA system, while a setup like the one in (b) was used with the 1 kHz CPA system.

is based on generation of high-order harmonics in Ar, followed by transmission through a 200 nm thick Al film. The Al film blocks all radiation below approximately the 13th harmonic, and compresses the higher-order harmonics into a train of attosecond pulses. This configuration was also used for the experiments in Papers **VI**–**VII**. However, the large number of possible combinations of pulse characteristics, generating media, metallic filters, and wavelength-selective mirrors offers a multitude of different characteristics of the HHG radiation, including single attosecond pulses [81], or attosecond pulse trains with one pulse per cycle [82].

Chapter 4

Photoemission

This chapter will give an introduction to the photoemission process, which is of fundamental importance for all experiments presented in this thesis. The term photoemission will here be used to describe *any* process in which the absorption of electromagnetic radiation leads to electron emission, regardless of mechanism. The starting point will be direct one-photon photoemission, after which the processes of secondary electron emission, multiphoton photoemission, laser-induced thermionic emission, and optical field emission will be described.

4.1 Direct photoemission

A general picture of photoemission is schematically depicted in figure 4.1. Matter emits electrons upon absorption of electromagnetic radiation, a process observed by Hertz in 1887 [83, 84]. However, it was not until 1905 that the process of photoemission was explained by Einstein [85], a discovery granting him the 1921 Nobel Prize in Physics. Einstein described the photoemission process as a photon with energy $\hbar\omega$ transferring its energy to a solid, causing the emission of an electron with kinetic energy $E_{\mathrm{kin}} = \hbar\omega - P$, with P being the work required for the electron to leave the sample. This work is usually divided into the *binding energy* E_{b} and the *work function* Φ, where the latter is a characteristic of the particular surface and is defined as the minimum energy required to remove an electron from a state at the Fermi level to a state where it no longer interacts with the surface. This gives the fundamental formula of photoelectron spectroscopy:

$$E_{\mathrm{kin}} \quad = \quad \hbar\omega - \Phi - E_{\mathrm{b}} \; . \tag{4.1}$$

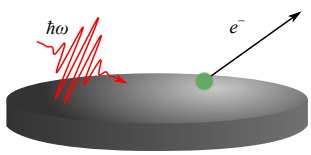

Figure 4.1: Common fundamental principle of photoemission: radiation impinges on matter, which emits electrons.

Photoemission is commonly described in a semiclassical way where the electromagnetic field is treated classically and the electron states quantum mechanically. Using perturbation theory and assuming a time-harmonic field, photoemission can be described by Fermi's golden rule. In a first-order approximation, Fermi's golden rule describes the transition probability per unit time $W_{i\to f}$ from an initial state $|i\rangle$ to a final state $|f\rangle$ as

$$W_{i\to f} = \frac{2\pi}{\hbar}\left|\langle f|\hat{V}|i\rangle\right|^2 \rho_i\,(1-\rho_f)\,\delta\left(E_f - E_i - \hbar\omega\right)\ . \tag{4.2}$$

Here, ρ_i and ρ_f represent the populations of states i and f, the delta function guarantees energy conservation, and $\hat{V}$ is the part of the Hamiltonian representing the perturbation [86, 87]. $\hat{V}$ can be quite complicated to estimate if, for example, effects of electron–electron interaction, variations of the field across the extent of the electronic states, or relativistic effects are included. The important feature for the coming description is that $\hat{V}$ is proportional to the amplitude of the electric field. From this first approximation, the conclusions are therefore:

i) Electrons can only be emitted if the photon energy is higher than the work function of the surface.

ii) Increasing the intensity of the incident radiation gives a proportional increase in the number of electrons, but does not alter their energy.

iii) Increasing the energy of the photons increases the maximum energy of the emitted electrons.

The initial state in the photoemission process is typically a solid in thermal equilibrium, while the final state is a free electron and a solid with a decaying hole. The transition from the initial to the final state is most accurately described as a single step taking all effects into account, but there is also simpler and more phenomenological three-step model[1] [84, 88]. The three-step model describes the photoemission process as excitation of the electron to a higher state in the band structure, transport to the interface, and finally penetration through the surface. This model will be used in the next section as a starting point to describe secondary electron emission.

The work function for most solid materials is on the order of 4–5 eV, meaning that visible light cannot normally induce photoemission. At ultraviolet energies slightly above the work function of the material, electrons are typically emitted in a direct process often referred to as threshold photoemission. This can be accomplished with, for example, a Hg discharge lamp, which emits light with energies up to 4.9 eV and is also the most common light source for PEEM. However, one of the major strengths of photoemission techniques is the possibility to spectrally resolve electrons emitted from deeper energy levels, as this together with

[1] Not to be confused with the three-step model of high-order harmonic generation described in chapter 3.

equation 4.1 gives experimental access to the binding energies of both core-level and valence band electrons. Core-level binding energies are both element specific and sensitive to the chemical environment, and X-ray photoelectron spectroscopy has therefore become an extremely wide-spread technique for chemical characterization of surfaces. The interaction of a high-energy photon in the extreme ultraviolet (XUV) or X-ray regime can also cause electron emission through other mechanisms than the direct photoemission of a core-level electron. For example, an initial excitation of an electron can give rise to subsequent electron–electron interaction resulting in Auger electron emission or secondary electron emission. Some important mechanisms for electron emission by high-energy photons are pictured schematically in Fig. 4.2, together with their respective spectral signatures.

4.2 Secondary electron emission

The majority of the electrons emitted from a solid upon X-ray excitation are secondary electrons (SEs). The SE cascade, drawn schematically in Fig. 4.2c, arises because of the electron–electron interaction in the solid. After initial excitation of an electron to a high-energy state in the band structure, this primary electron can exchange energy and momentum with other electrons in the material, thus promoting them to excited states. In this way, the excitation of a single electron to a higher-energy state can lead to a large number of excited electrons in the material. This can in turn lead to a quantum yield of more than one emitted electron per absorbed photon, in contrast to the case of direct photoemission. From an experimental point of view, the abundance of secondary electrons makes them easy to detect, but their applicability to time-resolved studies could be limited by the duration of the SE cascade. The rest of this section will therefore go through the steps in SE emission to better understand the process and to obtain an estimate of its duration. Because of the importance of metals for ultrafast nano-optics, in combination with their relatively simple electronic structure, the focus will be on emission from metals.

The probability for electron–electron scattering is what determines the mean free path for low-energy electrons ($\lesssim$ 50 eV) in a metal, and this mean free path can be as short as a few Ångström. At high primary electron energies, the momentum of the primary electron is so large that it upon scattering will hardly change its direction. In the opposite side of the spectrum ($\lesssim$ 50 eV), the electron–electron scattering is almost spherically symmetric and the energy lost by the primary electron can be approximated to follow a rectangular distribution [89].

The model developed more than half a century ago by Wolff [89] has also been used more recently for application to attosecond spectroscopy from solids [90]. This simple model treats the electrons as classical, free particles with an energy-independent mean free path (of 5 Å), scattering with each other in a spherically symmetric fashion and losing on average half their excess energy in each collision. It furthermore assumes that all electrons are excited from the Fermi level of the metal. The photoelectron spectrum can be calculated analytically using

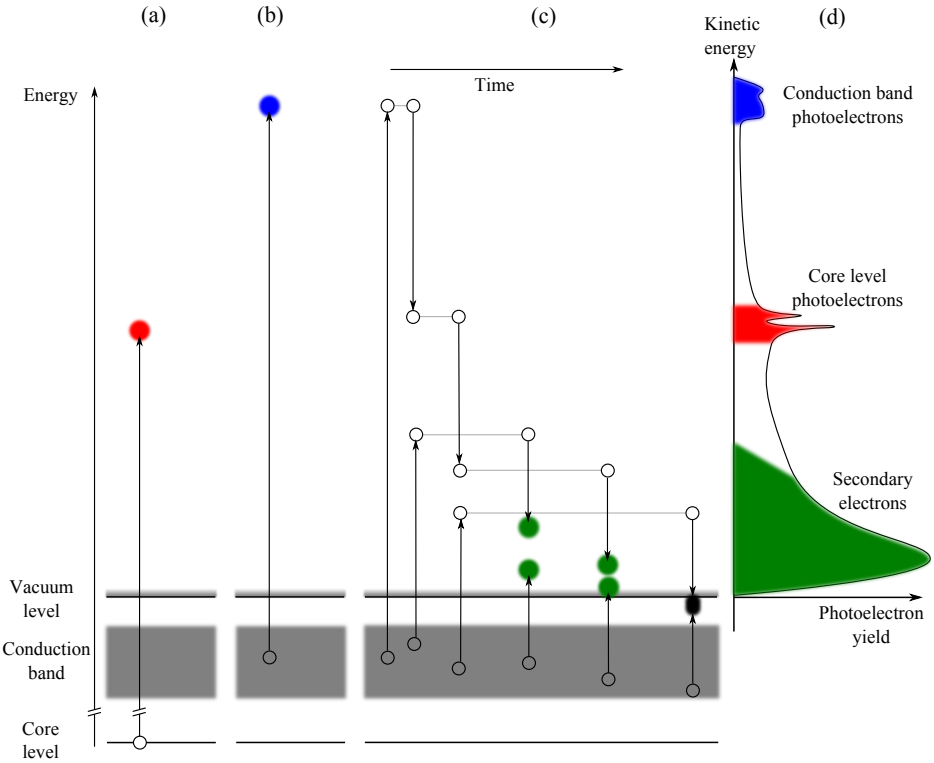

Figure 4.2: Schematic diagram of photoemission using high-energy photons. Three different processes and their respective spectral signatures are shown: core level photoemission (a), conduction band (or valence band) photoemission (b) and secondary electron emission (c). In (c), the SE cascade is schematized in the time domain. It starts with an electron from the conduction band (or from a core level) being photoexcited to a short-lived state. The electron can decay from this state by interaction with an electron in the conduction band, exchanging energy and resulting in two excited electrons. The lifetimes (drawn as horizontal grey lines) of the excited electrons depend on their energy. Green circles represent electrons that penetrate the surface barrier and escape, while filled black circles represent electrons that have energies below the vacuum level, and thus will be thermalized back into the Fermi sea. The respective spectral signatures of these processes are shown in a sketch of a typical photoelectron spectrum in (d). The secondary electron peak is usually even more dominant than depicted in the figure.

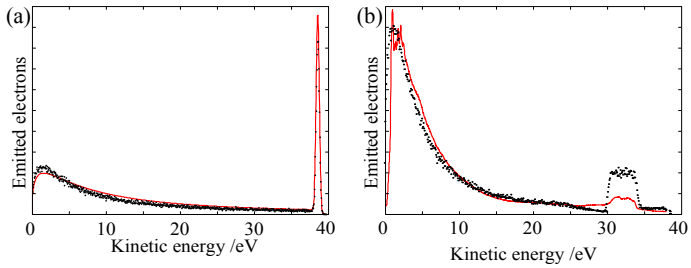

Figure 4.3: (a) Theoretical photoelectron spectra calculated using the analytical model of Wolff [89] (red line) and using the simplest version of the Monte Carlo model (black dots). (b) Theoretical photoelectron spectrum calculated using the modified Monte Carlo model used in Paper **VI** (black dots), and experimental spectrum measured at the I311 beamline at the MAX IV Laboratory (red line). All theoretical spectra were calculated using an excitation source with 43 eV central energy and 0.5 eV bandwidth, to create similar conditions as for the experimental spectrum.

this model, as seen in Fig. 4.3a. In Paper **VI**, a Monte Carlo simulation is presented based on this model. The Monte Carlo simulation uses some of the same approximations, but is done in real-time, calculating energy and momentum for the electron for each discrete time step. This allows for a simulation of the temporal evolution of the SE cascade, and thus for evaluation of the feasibility of SEs in time-resolved studies. The use of the same assumptions means that the results from the Monte Carlo simulation are very similar to those from the analytical model, as seen from the comparison between the modelled spectra in Fig. 4.3a.

In order to reach a better agreement with experimental data, the Monte Carlo simulation can be modified to include an energy-dependent mean free path. The lifetime of a hot electron depends on the energy above the Fermi level, since a higher-energy electron has more electrons available to scatter with. Fermi liquid theory predicts the lifetime to be $\tau = \alpha\,(E - E_F)^{-2}$. The parameter α depends on the material, and values also vary a bit throughout the literature. For Ag, reported values lie between 10 and 40 fs eV^2 [91–95].

Another modification is to include an approximate band structure of the material. This accounts for the fact that electrons are not only excited from the Fermi level, but from all available filled states. In the model used in Paper **VI**, the band structure of Ag is approximated with two rectangular distributions, representing the 4d and the 5s electrons, respectively. The simulated spectrum using these two modifications is shown in Fig. 4.3b, together with an experimental photoelectron spectrum measured at the I311 beamline at the MAX IV Laboratory. This modified Monte Carlo simulation gives a qualitative agreement with the experimental spectrum, even though the ratio between primary and secondary electrons differs. This can be both because of shortcomings of the semiclassical model and because the electron energy analyser used to record the experimental spectrum was not optimally calibrated for the low energies of the secondary

electrons.

An important advantage of the Monte Carlo simulation over the analytical model is that more information than just the energy distribution of the emitted electrons can be gained. For example, the temporal evolution and the spatial extent of the secondary electron cascade can be directly extracted from the simulations. This was done in Paper **VI**, where the simulations showed that 80% of the emitted electrons escape within 1 fs after excitation, and that 80% of the emitted electrons originate from primaries that were created within a volume 1 nm away laterally and 2 nm into the material, counted from the position of emission. This probing depth agrees well with an experimental study done with slightly higher photon energies using different thicknesses of Cr in synchrotron-based PEEM experiments [96].

4.3 Nonlinear photoemission

With the large peak intensities possible with femtosecond laser pulses, especially in combination with nanostructures enhancing the optical field at the surface, nonlinear phenomena become likely. This section will describe electron emission resulting from nonlinear interactions of electrons with the optical field. The description assumes a separation between a linear collective response of the sample giving rise to an enhanced local field, followed by a nonlinear interaction between the local field and single electrons in the sample [97]. Nonlinear photoemission was studied in all of the Papers **I**–**VII**, and was of central importance in Papers **I**–**V**.

4.3.1 Perturbative multiphoton photoemission

Equation 4.2 is a first-order approximation in the sense that it assumes only one interaction between the field and matter. However, with the high intensities possible with femtosecond laser pulses, first-order perturbation theory is no longer a good approximation. Extending the treatment to higher-order perturbation theory, the transition rate (equation 4.2) will also depend on transition matrix elements describing multiple interactions with the perturbation. For example, the expression for a three-photon transition will include matrix elements of the form

$$V_{fpqi} \quad = \quad \langle f|\hat{V}|p\rangle\langle p|\hat{V}|q\rangle\langle q|\hat{V}|i\rangle \ , \tag{4.3}$$

which describes the transition to an intermediate state $|q\rangle$, then to a second intermediate state $|p\rangle$, followed by the transition from $|p\rangle$ to the final state. This third-order matrix element is proportional to the cube of the perturbation (and thus the field), and the nth order matrix elements will correspondingly be proportional to the nth power. To estimate the total n-photon photoemission (nPPE) yield, one must also sum the transitions over all possible intermediate

states. Importantly, the energy conservation law regarding the n-photon transition is that the final and initial states must be separated by n photon energies, and photoemission is therefore possible even for photon energies below the work function.

The intermediate state(s) can be either real or virtual. The lifetime of real intermediate states has been intensively studied by time-resolved two-photon photoemission spectroscopy [91, 97, 98]. If the transition occurs via at least one real state, the photoemission is resonant and its probability can be greatly enhanced. Figure 4.4 shows energy diagrams of (a) non-resonant and (b) resonant multiphoton photoemission. The non-resonant photoemission occurs solely via virtual states and is usually assumed to be instantaneous [99, 100]. The n-photon photoemission probability during a short time $\mathrm{d}t$ is then proportional to the $2n$th power of the instantaneous electric field. The total photoemission yield at a point $\vec{r}$ by a field of finite duration can therefore be estimated as

$$Y(\vec{r}) \quad \propto \quad \int_{-\infty}^{\infty} |E(\vec{r},t)|^{2n} \mathrm{d}t \; . \tag{4.4}$$

The probability of multiphoton photoemission is also strongly favoured by an electric field polarized perpendicular to the surface [101–104]. For this reason, it is a good approximation to consider only the field component normal to the surface when evaluating equation 4.4.

4.3.2 Thermionic emission

If the temperature of the material is increased, the Fermi distribution will flatten out, and the probability increases for an electron to have a high enough energy for emission (figure 4.4c). A back-of-the-envelope calculation using the Richardson-Dushman equation [105–107] and a typical work function of 4.5 eV tells that the thermionic emission rate reaches a modest value of 1 el. s^{-1} $\mu\mathrm{m}^{-2}$ at a temperature of around 1200 K, which is already hot enough to permanently damage most nanostructures used in the work behind this thesis. However, this reasoning assumes a thermal equilibrium, which is far from the case for excitation with short pulses. Instead, the process of electron excitation followed by electron–electron interactions will effectively heat the electron gas on a femtosecond timescale, while the heat dissipation from the electron gas to the crystal lattice is a much slower process. The electronic temperature can therefore be much higher than the lattice temperature, and thermionic emission can occur without damage of the sample. Thermionic emission does not show a simple power-law dependence on the intensity of the excitation, but has an effective order that decreases with increasing intensity [107]. It is also incoherent, in the sense that the relative phase between the different absorbed photons is not important, in contrast to the case of coherent multiphoton photoemission (figure 4.4a). Equation 4.4 is therefore not necessarily valid, as the assumption of an instantaneous response no longer holds.

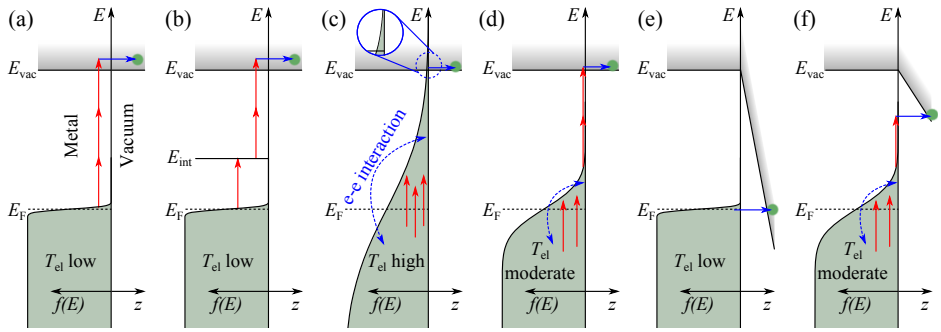

Figure 4.4: Different mechanisms of electron emission through absorption of multiple photons. (a) Coherent non-resonant multiphoton photoemission. The electron is excited by three photons via virtual energy levels. (b) Resonant multiphoton photoemission. The electron is excited by three photons via one real and one virtual energy level. (c) Thermionic emission. The electron gas is heated by absorption of photons and by electron–electron interaction, to the point where the high-energy tail of the Fermi distribution reaches above the vacuum level. (d) Combination of the previous processes. The electron gas is heated to a moderate temperature, until electrons at the high-energy tail of the Fermi distribution can be emitted by fewer photons than in (a). (e) Field emission. The applied field is so strong that it distorts the potential to the point where electrons at the Fermi level can tunnel out into vacuum. (f) Example of a combined process, where the electron gas is heated to a moderate temperature, an electron is photoexcited, and then tunnels through the barrier formed by the slightly distorted potential.

The processes of perturbative multiphoton photoemission and thermionic emission are not mutually exclusive. A moderate heating of the electron gas can lead to an appreciable amount of electrons whose energy allows for photoemission by fewer photons than for electrons at the Fermi level (figure 4.4d). Such processes further complicate the interpretation of nonlinear photoemission data.

4.3.3 Optical field emission

In the regime of strong fields, the laser field can no longer be considered a perturbation and Fermi's golden rule is not applicable regardless of the order. In this regime, the dominant mechanism for electron emission is instead through electron tunnelling, which can occur if the field distorts the potential to the point where unoccupied states in the vacuum overlap with occupied states in the material (figure 4.4e). Field emission has mainly been observed from sharp metal tips, where the field can be concentrated at the apex, causing a localized emission of electrons for applications such as electron guns. Optical field emission is slightly different because of the rapidly oscillating field. Optical field emission dominates over multiphoton photoemission when the Keldysh parameter $\gamma = \omega\sqrt{2m\Phi}/(eE)$ is below unity [108–110]. For a work function of 4.5 eV and a central photon energy of 1.55 eV, this occurs at an electric field strength of approximately 10 V/nm, corresponding to a peak intensity of $\sim 10^{17}$ W m^{-2}, which is high enough to permanently damage many materials.

Field emission can still not be excluded from PEEM investigations, for a number of reasons. First of all, it can act together with the previously described mechanisms, as depicted in figure 4.4f. Furthermore, the damage threshold is measured with respect to the intensity of the incoming pulse, while the probability for tunnelling is governed by the local field at each point on the surface. Because of the very high local field strengths that can be reached by plasmonic field enhancement, optical field emission has been observed from nanostructures with sharp tips or small gaps [58, 110, 111]. Finally, because of the linear dependence on ω, field strengths high enough for optical field emission can be reached by using laser pulses of lower frequency. For example, at a photon energy of 0.8 eV the same Keldysh parameter is reached at about 25% of the intensity compared to at 1.55 eV photon energy.

Chapter 5

Photoemission Electron Microscopy

The concept of forming an image of electrons photoemitted from a surface was realized by Brüche in 1933 [13]. Photoemission electron microscopy (PEEM) has since then found applications within a wide variety of research fields, much because of the versatility of the technique when combined with a variety of different light sources. PEEM can be combined with, for example, gas discharge lamps, synchrotron radiation sources, and many different types of lasers, to give information about the structural, chemical, electronic, and optical properties of surfaces. This chapter will give an introduction to the working principle and electron optics of current instrumentation, in particular the FOCUS IS-PEEM used for Papers **I**–**VII**. It will also discuss some practical considerations of designing an experimental setup for PEEM.

5.1 Principle

PEEM belongs to the family of cathode lens microscopy techniques, which most notably also includes low energy electron microscopy (LEEM). A cathode lens microscope images low-energy electrons either emitted from or reflected off a surface, electrons which are then accelerated by a high voltage and imaged using a set of electron lenses. Because of the rapid acceleration of electrons from the surface, the microscope can utilize the surface sensitive and non-destructive nature of low-energy electrons while still obtaining the high-quality electron microscopy images only possible with multi-keV electrons. However, the acceleration field itself both limits the resolution and complicates the interpretation of PEEM images, as will be described in the following sections.

Figure 5.1 shows schematic drawings of two different PEEM systems: (a), The Integral Sample Stage Photoemission Electron Microscope (IS-PEEM) manufactured by FOCUS GmbH and situated in the laser laboratories of the Department of Physics, and (b), the Aberration Corrected Spectroscopic Photoemission and Low Energy Electron Microscope (AC-SPELEEM) manufactured by Elmitec GmbH and attached to the I311 beamline at the MAX IV Laboratory. The former instrument was used for Papers **I**–**VII**, and the latter was used in the work behind Papers **VII**–**IX**.

These two microscopes are examples of one simple and compact and one complex and versatile PEEM instrument. The Elmitec instrument, with its combination of imaging, diffraction, and spectroscopy with illumination by either photons

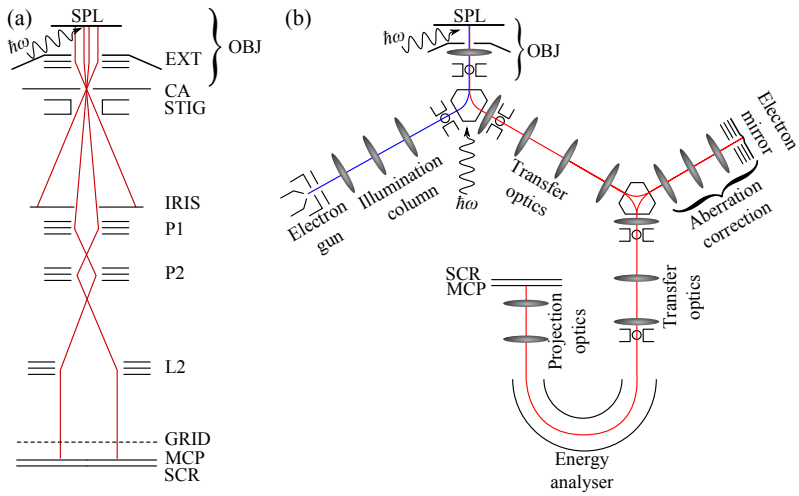

Figure 5.1: Schematic drawings of (a) the FOCUS IS-PEEM, and (b) the Elmitec AC-SPELEEM. SPL: sample; OBJ: Objective lens; EXT: Extractor; CA: Contrast aperture; STIG: Stigmator; MCP: Multichannel plate; SCR: Screen; P1, P2: Projective lenses; L2: Preretardation lens.

or electrons, is as close to the complete surface science instrument as it gets. Examples of the vast possibilities of a microscope such as the Elmitec instrument are shown using heterostructure III–V nanowires as an example system in figure 5.2. Aside from its versatility, the instrument also offers an improvement in PEEM spatial resolution by about a factor of 2 compared to the FOCUS instrument, possibly even further when using the aberration corrector. However, the simple design and operation along with the compact frame of the FOCUS instrument makes it well-suited for exploring the use of new types of state-of-the-art laboratory light sources together with PEEM.

Only the FOCUS IS-PEEM, which was the main instrument for the work behind this thesis, will be described in detail. It is a completely electrostatic system basically consisting of one objective and two projective lenses. It is also equipped with a stigmator/deflector, a contrast aperture limiting the electron angles, and a retarding field energy analyser. The resolution of the microscope is determined mainly by the objective lens, while the projective lenses are used to vary the magnification. The projective lenses can also be turned off, meaning that the microscope can be operated with zero, one, or two intermediate images (electron rays corresponding to the latter case are shown in figure 5.1a). After the projective lenses, the microscope is equipped with a preretardation lens (L2) used to decelerate and collimate the electrons before the retarding field energy analyser. This analyser uses two copper grids to create a homogeneous electric field which decelerates the electrons to ground potential. Slightly changing the sample potential then provides a means of spectromicroscopy, as the retarding

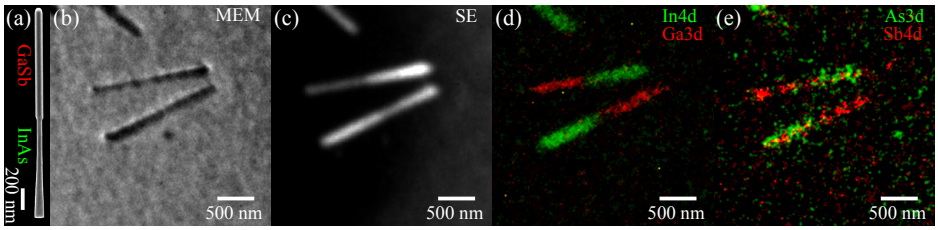

Figure 5.2: Example usage of the Elmitec SPELEEM in combination with synchrotron radiation. (a) SEM image of a nanowire with an InAs bottom part and a GaSb top part. (b) Mirror electron microscopy (MEM) image of two such nanowires, reflecting the electric potential just outside the surface. (c) Secondary electron (SE) image of the same nanowires excited by 70 eV photons from the MAX II storage ring. (d) Two overlaid energy-filtered PEEM images acquired using photoelectrons from the In4d (green, $\hbar\omega = 70$ eV) and Ga3d (red, $\hbar\omega = 70$ eV) core levels. (e) Two overlaid energy-filtered PEEM images using photoelectrons from the As3d (green, $\hbar\omega = 150$ eV) and Sb4d (red, $\hbar\omega = 70$ eV) core levels.

field acts as a high-pass energy filter. The microscope can, however, also be operated without energy filtering.

5.1.1 Sample requirements

As the sample is an integral part of the objective lens of a cathode lens microscope, the properties of the sample can strongly influence the image quality. In order to obtain the highest homogeneity of the acceleration field in the objective lens, the sample should in principle be an infinitely large, completely flat perfect conductor carefully aligned normal to the optical axis of the microscope. In practice, this means that low conductivity, large topographical features, and sample misalignment will all cause distortions of the PEEM image. PEEM instruments therefore have special sample holders to insure an acceleration field which is as homogeneous as possible. Figure 5.3 shows two samples mounted in two different sample holders for the FOCUS IS-PEEM, together with a schematic drawing of the holder. The sample surface is held against a metal cap using a spring, and the sample holder is then fitted into the integral sample stage of the microscope. This ensures that the sample normal coincides with the optical axis of the microscope, as well as eliminates any field distortions arising from sharp edges of the sample. Two different sizes of the cap are available from the manufacturer, with 5 mm or 8 mm open aperture. The former can be used with smaller samples, but limits the area that can be imaged to a few mm^2, as field inhomogeneities caused by the sample holder distorts images of features less than ~ 1.5 mm from the cap of the sample holder.

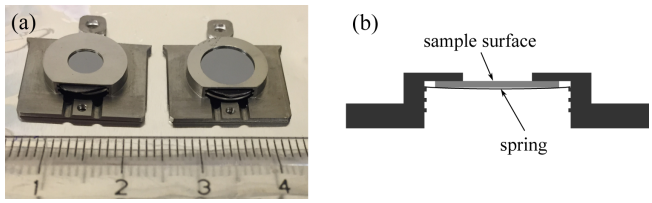

Figure 5.3: (a) Photograph of two different sample holders for the FOCUS IS-PEEM, with 5 mm (left) and 8 mm (right) open aperture, respectively. (b) Side-view cross-sectional sketch of the sample holder. The sample is fixed against the cap of the sample holder by a spring, which in turn is held in place by grooves in the side of the sample holder.

5.2 Aberrations of the objective lens

In the introductory chapter of this thesis, PEEM was described as a way to measure optical properties of a surface without being limited by the diffraction of light. Diffraction in an optical microscope, as well as in an electron microscope, limits the spatial resolution to approximately half the wavelength. Assuming an energy of the photoemitted electrons of 0.5 eV ($\lambda_e \approx 1.7$ nm), the diffraction limit for a PEEM instrument would be below 1 nm, which is far better than the obtainable spatial resolution of the FOCUS IS-PEEM ($\sim$ 30 nm). The resolution is instead limited by the aberrations of the objective lens. The objective lens in the FOCUS IS-PEEM is an electrostatic tetrode lens, consisting of four parts: sample, extractor electrode, focus electrode, and column electrode. In typical conditions, the sample is grounded and the extractor electrode is set to a fixed positive voltage of 10–15 kV. The voltage on the focus electrode then determines the focal length of the lens [112]. Close to the back focal plane of the objective lens is an octupole stigmator/deflector, which compensates for non-spherical aberrations, and a contrast aperture limiting the angular distribution of the photoelectrons.

The resolution of the electron optics is mainly limited by three factors: spherical aberration, chromatic aberration, and diffraction. The latter comes into play when a small contrast aperture is used, lowering the effective numerical aperture of the objective lens and thus increasing the diffraction limit. The spherical and chromatic aberrations can in turn be divided into aberrations originating from the acceleration field and from the lens itself. The combined effect of aberrations of the acceleration field and objective lens can be described as the imaging of a point source as a disc of finite radius δ. Counting aberrations up to third order, which gives a reliable result for non-aberration corrected microscopes, the radius δ can be calculated for small starting angles as [113, 114]

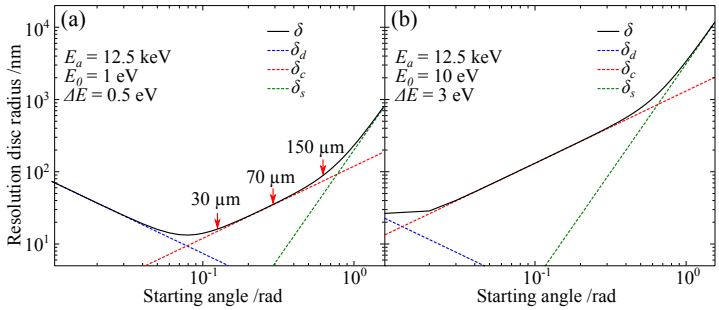

Figure 5.4: Combined aberrations of the objective lens for two sets of parameters. (a) Low starting energy and high monochromaticity gives an optimum resolution of a few tens of nanometres. Approximate cutoff angles for the three smallest contrast apertures in the FOCUS IS-PEEM are indicated by red arrows. (b) Higher starting energy and larger energy spread instead gives a calculated resolution in the micrometre regime.

$$\delta = \sqrt{\delta_s^2 + \delta_c^2 + \delta_d^2}\,, \tag{5.1}$$

$$\delta_s \approx \left(l\frac{E_0}{E_a} + \frac{1}{4}C_s\left(\frac{E_0}{E_a}\right)^{3/2}\right)\xi^3\,, \tag{5.2}$$

$$\delta_c \approx \left(l\frac{E_0}{E_a} + C_c\left(\frac{E_0}{E_a}\right)^{3/2}\right)\frac{\Delta E}{E_0}\xi\,, \tag{5.3}$$

$$\delta_d \approx \frac{0.73\ \text{nm}}{\sqrt{E_0\ /\text{eV}}\sin\xi}\,. \tag{5.4}$$

Here, E_0, E_a, and ΔE are the start energy, acceleration energy, and energy spread of the electrons, ξ is the starting angle, l is the distance between sample and extractor, and C_s and C_c are the spherical and chromatic aberration coefficients of the lens. The radius δ of the total resolution disc and the contributions from the different types of aberrations are shown in figure 5.4 as functions of starting angle for two sets of parameters and using values of $l = 1.8$ mm, $C_s = 300$ mm, and $C_c = 130$ mm, as appropriate for the FOCUS IS-PEEM [114].

The calculated resolutions in figure 5.4 clearly show both the importance of monochromaticity and of a small contrast aperture for optimum spatial resolution. However, the transmission of the microscope is, for small angles, proportional to the square of the aperture radius. This means that the microscope can only be operated with a small contrast aperture if the total emission current is high, as the signal-to-noise ratio might otherwise not allow imaging.

In the hunt for improved spatial resolution, some cathode lens microscopes with correction of aberrations up to third order have been developed lately [115–117]. The correction is performed by reflecting the electrons off an electrostatic tetrode mirror, which can be carefully set to have the same spherical and chromatic

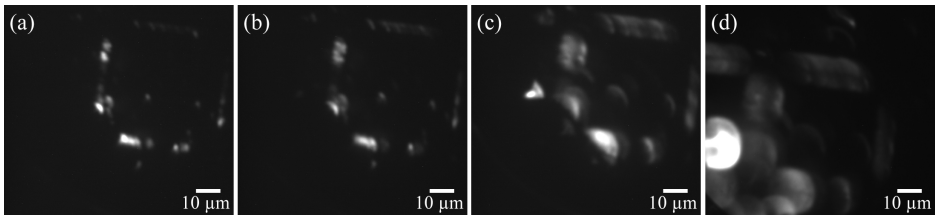

Figure 5.5: (a–d) PEEM images of a lithographic pattern, acquired using femtosecond laser pulses with 800 nm central wavelength. The intensity of the laser pulses impinging on the sample increases from (a) to (d), causing a severe blurring of the image.

aberration coefficients as the objective lens, but with opposite sign [118]. Such an aberration correcting mirror has been implemented with the AC-SPELEEM system at the MAX IV Laboratory, as is depicted in the schematic of figure 5.1b.

5.3 Space charge effects

An effect not included in the discussion of aberrations so far is the space charge effect, which can have a major influence on PEEM experiments using pulsed light sources. At large peak emission currents, the free electron density in the microscope column can become high enough for mutual repulsion between electrons to become important. Such high electron densities can occur close to the sample before the electrons are fully accelerated, in the back focal plane of the objective lens, in energy analysers, or at aberration correcting mirrors [117, 119, 120]. The effect of space charge effects can be clearly seen in figure 5.5, showing a series of images acquired with increasing intensity of the excitation source.

Space charge effects can be divided into deterministic and stochastic effects. Deterministic effects are interpreted as the action on electrons by an average background charge ("true" space charge effects), while the stochastic effects can be seen as an acceleration or lateral deflection of electrons by interaction with single or few electrons [121, 122]. If the total emitted charge forms an approximatively homogeneous beam of electrons, the effect of "true" space charge causes a near-symmetric change in the electric field in the microscope, which leads to a defocus of the electrons. This effect can therefore, to some extent, be compensated by adjusting the focus of the microscope. The stochastic effects are however impossible to compensate for. Lateral deflection of electrons causes a direct blurring of the image, while acceleration and deceleration along the optical axis are most important for microspectroscopy purposes, but contribute indirectly to the image blur through chromatic aberrations.

Because of the inhomogeneity of the beam of emitted electrons and the stochastic effects, the only way to get rid of image blurring due to space charge effects is to limit the peak emission current. For excitation by femtosecond pulses, this is equivalent to limiting the number of emitted electrons per pulse. For space charge effects to be completely eliminated, a maximum of one emitted electron per pulse

is acceptable. However, this quickly becomes challenging for PEEM using excitation sources with a low repetition rate, such as the 1 kHz CPA system described in section 3.2.2. Even if all emitted electrons are used to form the image, the limit of 1000 electrons per second[1] requires very long exposure times in order to collect enough electrons for an image. In practice, it can therefore be advantageous to choose working conditions where space charge effects are not completely eliminated, as there is a trade-off between space charge effects, aperture size, and signal-to-noise ratio. This will be discussed further in section 6.3.

5.4 PEEM setup for laser experiments

The PEEM setup was modified during the work behind this thesis, and the new design will be presented here. The new setup was designed for high flexibility and to be easily moved between different optical setups. The design, shown in figure 5.6, is based on a vibrationally damped optical table with a footprint of 1200×750 mm^2, with a specially designed optical breadboard to make room for vacuum pumps underneath the chamber. The microscope is placed close to one end of the breadboard so that the sample can be positioned close to the optical table containing the laser setup, but also to make room for features such as transfer chambers and optical characterization setups on the opposite side. This possibility of an optical setup on the PEEM breadboard was used to characterize the beam reflected off the sample. This is important for practical aspects such as aligning the beam onto the sample, but can also be used to optimize the focal spot. By placing a lens and a CCD to image the beam reflected off the sample, an optical image of the focal spot on the sample was obtained. The alignment of an IR/visible beam on the sample was performed in multiple steps:

i) The unfocused beam was sent onto the sample. A CCD camera was placed behind the microscope and aligned so that the beam reflected off the sample hit the centre of the CCD.

ii) A lens was inserted between the sample and CCD and aligned to ensure a sharp image of the sample in the centre of the CCD.

iii) The focusing lens was placed before the entrance window of the microscope and aligned to create the smallest possible focal spot size centred on the CCD.

For experiments using high-order harmonics (Papers **VI**–**VII**), the microscope chamber was instead attached to the vacuum chamber of the HHG setup. Because of the harmonics being focused by a toroidal mirror rather than a lens, the microscope had to be aligned with respect to the beam rather than the other way around. For this reason, the table was designed to be used with different types

[1] To completely eliminate space charge effects, the average number electrons per pulse must be even lower than one as the photoemission is a statistical process and the probability of multiple electrons must be kept low.

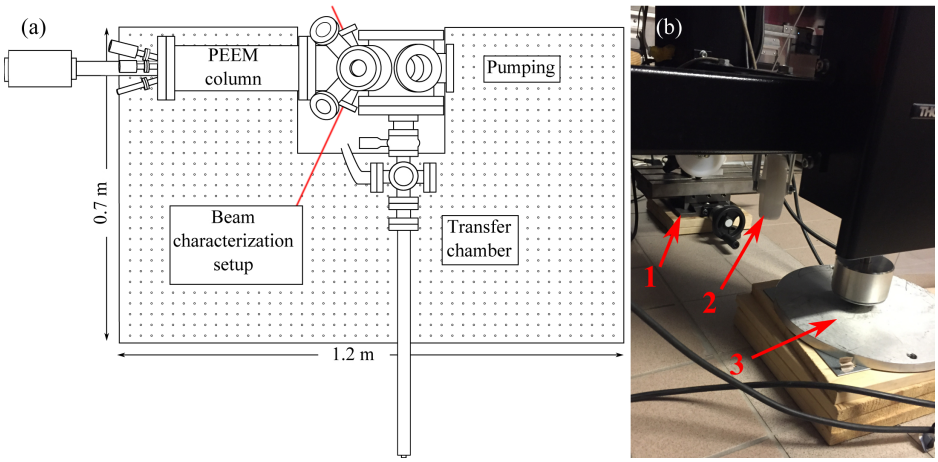

Figure 5.6: (a) Simplified top-view schematic of the PEEM setup. As seen from the drawing, the compact frame of the FOCUS IS-PEEM leaves plenty of space for optical components or an extension of the vacuum chamber even on a small-footprint optics table. (b) Photograph of the lower part of the PEEM table, showing the XY translation stage (1), the wheels (2), and the omnidirectional rolling ball (3).

of feet. For precise alignment of the PEEM setup with respect to the fixed beam from an HHG setup, the table was equipped with industrial XY translation stages on two of its legs, and omnidirectional wheels on the two other legs. This design was inspired by the setup for the SPELEEM instrument at the I311 beamline at the MAX IV laboratory. For easy, long-distance movement of the whole setup, the table can also be lowered onto four wheels. Concrete blocks are used as extra feet for large vertical adjustments of the microscope, which are needed because of the different beam heights in different laser setups. A photograph of the lower part of the table is shown in figure 5.6b. Finally, the microscope is resting on three wedge levellers on top of the breadboard for fine adjustment of the height and for levelling of the instrument.

5.5 Illumination geometries

Already in chapter 2, it was mentioned that the optical response of a nanostructured sample depends strongly on the angle of the incoming beam. An interesting topic of laser-based PEEM studies from recent years has therefore been the use of normal incidence versus grazing incidence excitation. The physical presence of the large extractor electrode close to the sample in a cathode lens microscope severely limits the excitation geometry in PEEM experiments. For LEEM/PEEM systems with a magnetic beam separator, it is possible to either excite in a grazing incidence geometry, i.e. from the side of the extractor electrode, or by shining the light through the beam separator to hit the sample at

normal incidence [123, 124]. For microscopes with a linear column, this becomes impossible and the microscope is typically used in grazing incidence geometry. However, near-normal incidence illumination can be achieved by shining the light through a hole in the microscope column and inserting a tiny mirror close to the back focal plane of the objective lens, thus reflecting the beam onto the sample through the objective lens [124].

The normal incidence geometry has several important advantages, as it simplifies the interpretation of the PEEM data by increasing the symmetry of the system. This has shown to be of value for the imaging of propagating SPPs in two-photon PEEM, where normal incidence illumination can also improve the effective spatial resolution [124]. The normal-incidence geometry also avoids retardation effects and limits which surface plasmon modes are possible to excite.

However, the more challenging interpretation caused by grazing incidence illumination is intimately connected with some important properties of nano-optical fields. One example is the excitation of dark surface plasmon modes, which because of symmetry constraints are difficult to excite in a normal incidence geometry. Another is the retardation effects caused by the phase difference of the excitation field across the nanostructure. These two phenomena can both have pronounced effects on the local near-field, which makes studies in low-symmetry excitation geometries access information that is unavailable with normal incidence excitation. The two different excitation geometries are therefore highly complementary.

Chapter 6

Experimental Results

This chapter will introduce and complement the papers by describing the main experimental results, tying together a number of concepts described so far into the main topic of this thesis: the combination of ultrashort laser pulses with PEEM for studies of ultrafast nano-optics. The chapter is divided based on the different types of experiments used for the papers. The first section describes PEEM using visible-to-infrared femtosecond pulses without time resolution (Papers **I**, **IV**, and **V**), the second section describes interferometric time-resolved PEEM (Papers **II**–**III**), and the final section describes PEEM using high-order harmonics (Papers **VI**–**VII**).

6.1 Multiphoton PEEM

Multiphoton PEEM was first introduced by Schmidt *et al.* [125], and has become a widely employed method for imaging enhanced electromagnetic fields on a conductive surface [15, 16, 110, 126–135]. The technique relies on the nonlinear dependence of multiphoton photoemission (see section 4.3) on the local intensity of the electromagnetic field. The multiphoton PEEM signal is therefore drastically increased in regions of enhanced fields, making the concentration of the optical field the main contrast mechanism.

The major strengths of multiphoton PEEM are the high spatial resolution, the non-invasiveness, the parallel imaging acquisition, and the fact that the detected signal is generated by a nonlinear process driven by the local electric field. This last point is important, as this is similar to the signal of interest in applications where local field enhancements are used to boost a nonlinear effect, such as harmonic generation [136, 137] or Raman scattering [48, 138]. As good as this sounds, multiphoton PEEM also has some limitations. First of all, it requires a conductive surface, which is otherwise not standard for samples used in optics. Second, distortions can arise due to the topography of the surface and the acceleration of the electrons in the near-field. This second part requires extra attention as it can limit the spatial resolution, and in some cases alter the image contrast. Finally, it relies on a photoemission process that is complicated to interpret quantitatively, and can itself give rise to new features in the images. As described in section 4.3, the probability of perturbative multiphoton photoemission at a point $\vec{r}$ is proportional to the $2n$th power of the local field strength. However, the constant of proportionality depends on many factors and can vary

locally. It is sensitive to the local work function of the material, including effects of different materials, different crystal facets, and of adsorbates on the surface. Furthermore, it also depends on the band structure between the Fermi level and the vacuum level, especially if the multiphoton transition can occur via at least one real state. Finally, it can depend on the density of crystal grain boundaries as these can facilitate momentum conservation in non-vertical transitions between real states in the band structure [98, 139].

Even if the photoemission yield could be quantitatively determined from the near-field, the distributions of emitted and detected electrons are not necessarily the same. This was seen already in chapter 5, describing the need to limit the angular distribution of photoelectrons to reduce spherical aberrations. Besides the effects of topography on the observed contrast, the strong optical near-fields present in multiphoton PEEM experiments further complicate the interpretation. Near-field strengths in multiphoton PEEM experiments are typically in the range of $10^7 - 10^{10}$ V/m, which can be compared to the 7×10^6 V/m acceleration field generated by an extractor voltage of 12.5 kV in the FOCUS IS-PEEM. The emitted electron will therefore not be initially accelerated by a homogeneous field defined by the objective lens, but will have its trajectory affected by the local optical near-field. Modelling of the electron trajectories in the combined field of the objective lens and the optical near-field is a complicated issue, and will not be discussed in further detail here.

The complexity of the multiphoton photoemission process essentially makes a direct quantitative measurement of the electric near-field using multiphoton PEEM impossible. However, as long as the sample does not change during a measurement, the local photoemission yield can be used as a relative measurement of the field strength while some property of the excitation source is varied. This is the common principle used in Papers **I**–**III** and **V**.

6.1.1 Polarization-dependent multiphoton PEEM

The properties of the enhanced near-field on a nanostructured surface can strongly depend on the incident polarization. This has been investigated in several previous multiphoton PEEM studies [140–142], and is also the topic of Papers **I** and **V**. The polarization of a grazing incidence illumination source is usually defined with respect to the plane of incidence, which is spanned by the wave vector of the excitation light and the normal vector of the sample surface. The polarization with the electric field parallel to the plane of incidence is then denoted p, and the perpendicular polarization is denoted s[1]. These polarizations are indicated in figure 6.1a.

Polarization-dependent multiphoton PEEM can be modelled in a straightforward way as long as the optical response of the sample is linear. In this case, the surface electric field induced by light with an arbitrary linear polarization can be calculated as

[1] The letters p and s stem from the German words "parallel" and "senkrecht" (parallel and perpendicular).

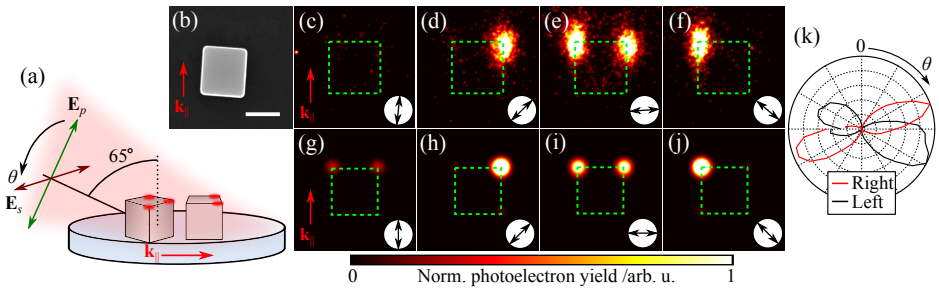

Figure 6.1: Polarization-dependent multiphoton PEEM of a single Ag nanocube. (a) Side-view schematic of the experiment. (b) SEM image of a Ag nanocube. Scalebar is 200 nm. (c–f) Multiphoton PEEM images of the same nanocube for four different polarizations of the incoming light. The light is incident from below in the images, and the polarization as seen in the direction of the incoming light for each image is indicated with an arrow. The green dashed lines represent the spatial extension of the cube. (g–j) Corresponding simulated PEEM images from FDTD simulations followed by equation 6.2. The elongation of the spots in the experimental images is because of image distortions from the topography of the sample and the laser-induced near-field. (k) Polar plots of the photoemission intensity from the two different corners as functions of polarization angle.

$$\vec{E}\left(\vec{r},t,\theta\right) \quad = \quad \vec{E}_p\left(\vec{r},t\right)\cos\theta - \vec{E}_s\left(\vec{r},t\right)\sin\theta\ , \tag{6.1}$$

where θ is the polarization angle defined as the clockwise deviation from p-polarization. Equation 6.1 was used to model the photoemission distribution from electric fields obtained by FDTD simulations in Paper **I**. Together with equation 4.4, and assuming a three-photon process, the PEEM signal from the top facet of a single Ag nanocube was modelled as

$$I\left(\vec{r},\theta\right) \propto \int \left(E_{z,p}\left(\vec{r},t\right)\cos\theta - E_{z,s}\left(\vec{r},t\right)\sin\theta\right)^6 \mathrm{d}t \ \otimes\ \exp\left(-\left|\vec{r}\right|^2/2\sigma^2\right)\ , \tag{6.2}$$

where the last part is a convolution with a Gaussian function representing the finite resolution of the microscope. The result of this modelling can be seen in figure 6.1, where experimental and simulated PEEM images of a Ag nanocube are compared for different polarizations. The excellent agreement strengthens the validity of equation 6.2 for the case of Ag nanocubes.

In some cases, the assumption of equation 4.4 does not hold and the polarization-dependent photoemission intensity does not directly reflect the polarization-dependent field enhancement. This can, for example, be the case if the material is anisotropic. This effect is discussed in Paper **V**, where InAs nanowires with varying wurtzite and zincblende crystal structure are studied. Wurtzite is a hexagonal crystal structure, and materials with the wurtzite structure can therefore have different optical properties depending on the polarization of the light

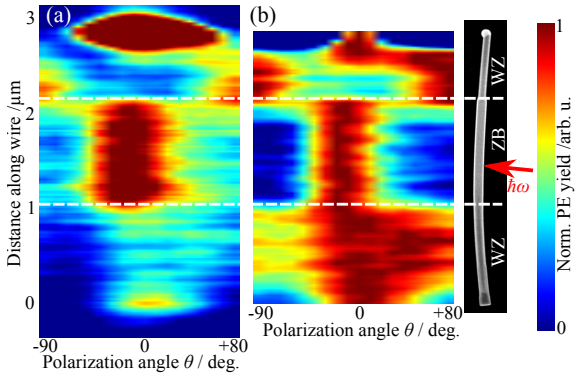

Figure 6.2: Example of an InAs wurtzite-zincblende-wurtzite nanowire and the polarization dependence of the multiphoton photoemission from each segment. (a) Intensity profile measured along the nanowire as a function of polarization of the excitation light. (b) Same data as in (a) normalized linewise for clearer visualization of the different polarization dependences of the segments. As in figure 6.1, 0° is defined as *p*-polarization and the polarization angle θ as the deviation in the clockwise direction as seen in the direction of propagation. An SEM image of the nanowire is shown in the right inset, along with an arrow indicating the in-plane direction of the excitation light. White lines mark the transitions between the crystal phases, as estimated from the SEM image.

with respect to the crystallographic directions. The polarization dependence of the photoemission yield is then governed by a combination of the morphology and the anisotropic response of the material.

An example of the polarization-dependent photoemission yield from an InAs nanowire with varying wurtzite-zincblende-wurtzite structure is shown in figure 6.2, displaying the photoemission intensity along the nanowire as a function of polarization. For *p*-polarized excitation ($\theta = 0°$), the Au particle (top) and the zincblende segment (middle) emit strongly. The upper wurtzite segment on the other hand shows a large emission for *s*-polarization, i.e. when the electric field is aligned with the long axis of the nanowire. The lower wurtzite segment instead shows a polarization behaviour reminiscent of a mixture between those of the zincblende and upper wurtzite segments. The slightly different morphologies of the segments cannot explain this difference in polarization dependence. We propose in Paper **V** that the polarization dependence of the emission from the zincblende segment is governed by the linear response of the material concentrating the light. In contrast, we suggest that the polarization dependence observed for the upper wurtzite segment is dominated by resonant multiphoton photoemission pathways including two- or three-photon transitions sensitive to the polarization of the light with respect to the crystallographic directions.

6.1.2 PEEM using low-frequency laser pulses

Because of the availability of Ti:sapphire femtosecond lasers, multiphoton PEEM studies have traditionally used laser pulses with energies centred around either 1.55 or 3.1 eV (the frequency-doubled output of a Ti:sapphire laser system). For most materials, this corresponds to 2–4 photons being needed for each emitted electron. However, the use of only two central wavelengths limits the applicability of multiphoton PEEM for studying enhanced near-fields in nanostructures. Paper **IV** extends the wavelength regime of multiphoton PEEM by using femtosecond pulses centred around the technologically important telecommunication wavelength of 1.55 μm (0.8 eV). From simple energy conservation laws, this corresponds to 6–7 photons being needed for the emission of each electron for typical values of the work function. As the study presented in Paper **IV** is the first of its kind, many experimental and theoretical questions remained unsolved, for example:

i) What is the dominating emission mechanism?

ii) Which structures will show a detectable field enhancement?

iii) Is it even possible to reach stable imaging conditions in this regime of high nonlinearity?

iv) Will the nanostructures be damaged by the intensities needed for PEEM?

Not all of these questions could be answered by the experiments, partly because of a lack of optical components designed for 1.55 μm radiation in our lab at the time. For example, we had no opportunity of controlled and continuous adjustment and measurement of the incident intensity, which would have been necessary to measure the photoemission yield as a function of laser power. Such a measurement can, as described in chapter 4, give valuable information on the emission mechanism. However, even with a controlled adjustment of the intensity, measuring the power law dependence could be challenging due to the low effective dynamic range limited in one end by the signal-to-noise ratio and in the other end by space charge effects. Some information on the emission process can instead be gained from photoelectron spectra [110, 143], which were measured from Ag nanoparticles in the study. Spectra from 4 particles are shown in figure 6.3a. The photoelectron spectrum is seen to exhibit two regions, each of which can be approximated by a straight line (added in figure 6.3a as a guide to the eye). While a photoelectron spectrum resulting from a purely perturbative process is expected to show a single exponential decline with energy, these spectra instead show a region of slow decrease followed by a sharp cutoff. The cutoff generally occurs at higher electron energy for the particles showing a higher emission yield. This is confirmed in figure 6.3b, which shows two spectra consecutively recorded from the same particle but with slightly different laser power. The second measurement, performed with lower laser power, shows a cutoff shifted to lower energies by approximately 0.4 eV.

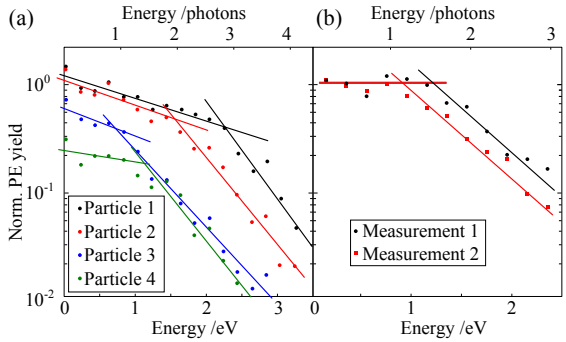

Figure 6.3: Photoelectron spectra from individual Ag particles excited by 1.55 µm radiation. (a) Spectra from 4 different particles within the same field of view. The particles show differences both in emission intensity and in the position of the cutoff of the spectrum, with the cutoff reaching approximately 3 photon energies above the photoemission threshold for the particle showing the strongest emission. (b) Two spectra from another particle, acquired with slightly different intensities of the excitation.

For future studies of PEEM in this wavelength regime, it would be important to increase the repetition rate of the laser system from the 1 kHz used for Paper **IV**. Furthermore, a stable measurement of the photoemission yield as a function of laser power would give valuable further insight into the photoemission process. Finally, it could be of interest to lower the work function of the material by adsorption of a sub-monolayer amount of an alkali metal in order to facilitate photoemission by fewer photons [16, 144]. This latter step would be of interest for studies of nano-optics at longer wavelength, but not for fundamental studies of higher-order photoemission processes.

6.2 Interferometric time-resolved PEEM

The concept of interferometric time-resolved PEEM (ITR-PEEM) was introduced by Schmidt *et al.* [14], and further developed by Kubo *et al.* [15]. The technique relies on the nonlinear photoemission induced by two identical laser pulses with a delay that can be controlled on a sub-cycle level. At delays much larger than the pulse duration, this can be considered a pump–probe technique where one pulse excites the system, and the second pulse probes the excited system at a variable delay. However, when the delay is of the same order as the pulse duration, the interpretation is slightly more complex. From the assumptions of section 4.3, the photoemission yield as probed by the microscope corresponds to a local nonlinear interferometric autocorrelation (IAC) of the surface electric field. The IAC is in some sense a time-resolved measurement, but cannot be interpreted as a stroboscopic film of the temporal evolution, and only in some special cases can the fundamental properties of the sample be retrieved from the IAC [97]. ITR-PEEM was used for Papers **II**–**III**, and the experimental setup

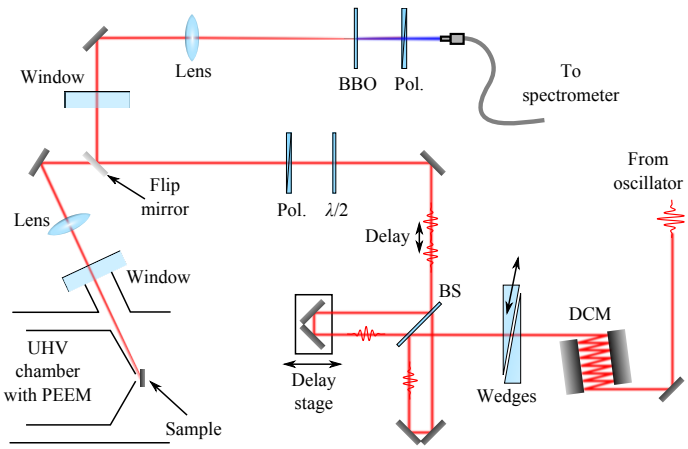

Figure 6.4: Experimental setup for the ITR-PEEM experiments presented in Papers **II**–**III**. DCM: Double Chirped Mirrors, BS: Beam Splitter, Pol: Polarizer.

used in these studies is shown in figure 6.4.

6.2.1 Interferometric autocorrelation

An nth order IAC of a continuous signal $f(t)$ of finite duration[2] maps the function $f(t)$ onto $R(\tau)$ according to

$$R(\tau) = \int_{-\infty}^{+\infty} |f(t) + f(t-\tau)|^{2n} \, \mathrm{d}t \, . \tag{6.3}$$

This equation can be compared with equation 4.4 describing perturbative coherent multiphoton photoemission by n photons. It is then seen that if the function f in equation 6.3 is the local near-field at the surface, the IAC $R(\tau)$ is proportional to the number of photoelectrons emitted by the near-field induced by two identical pulses delayed by a time τ with respect to each other. From the general formula of equation 6.3, it can be seen that i) the ratio between the measured signal at zero delay and at large delay is exactly 2^{2n-1} ($R(0)/R(\infty) = 2^{2n-1}$), and ii) the IAC has mirror symmetry around the absolute zero delay ($R(\tau) = R(-\tau)$). These two conditions can be used as indicators of how ideal the measurement is.

The interferometric autocorrelation technique has been widely used to characterize ultrashort laser pulses, for which it can accurately measure the pulse duration if the pulse shape is known [145]. A typical implementation for this measurement is to measure the intensity of the second harmonic generated in a nonlinear crystal as a function of delay between two identical pulses. The response of the nonlinear crystal is to a good approximation instantaneous, and

[2]Finite duration means that there exists a time t' such that $|t| > t' \Rightarrow f(t) = 0$.

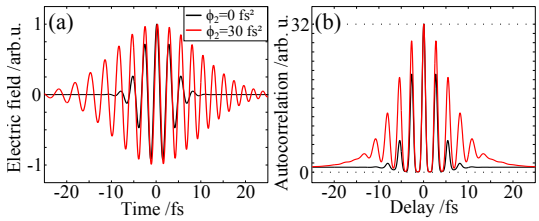

Figure 6.5: Two laser pulses and their IACs. Electric fields (a), and the corresponding third-order interferometric autocorrelations (b) of two Gaussian pulses with identical spectrum but different phase: Fourier limited (black), and with a linear chirp corresponding to a GDD of 30 fs^2 (red). The IACs show the same positions of the fringes but have different widths, and the fringes in the IAC of the chirped pulse wash out for large delays.

equation 6.3 is then valid with the laser pulse electric field as the function $f(t)$ and the intensity of the second harmonic proportional to the function $R(\tau)$. In ITR-PEEM, the interpretation is a bit more complicated as the field of interest is a convolution between the laser pulse and the sample response, and the precise shape of the field is therefore typically not known. The ITR-PEEM studies presented in Papers **II**–**III** deal with third-order IACs, and the rest of this section will therefore focus on cases where $n = 3$. The third-order IACs of two laser pulses with identical spectra but different phases are shown in figure 6.5. For a Fourier limited Gaussian pulse, the IAC also has a Gaussian shape with a constant separation between the fringes (black curves). If the pulse has a linear chirp (red curves), the envelope is widened and the visibility of the fringes decreases in the wings of the IAC, corresponding to the overlap between the high-frequency part of one pulse and the low-frequency part of the other pulse.

Because of the complicated relationship between the near-field and its interferometric autocorrelation, it typically has to be interpreted using simulations based on certain assumptions. A first approximation is assuming a single harmonic oscillator response of the system [146]. Figure 6.6a–b show the electric fields and IACs of two harmonic oscillators excited by the 5.5 fs laser pulse shown as a black curve in figure 6.5. The oscillators have the same lifetime $\tau_l = 7$ fs (defined as the time for the intensity of the impulse response to drop to e^{-2} of its maximum value), but different resonance frequencies ($\hbar\omega_0 = 1.65$ eV and $\hbar\omega_0 = 1.46$ eV, respectively). The resulting fields show the same decay rate but different oscillation frequencies, which is also seen in the IAC where the fringes of the curve calculated from the lower-frequency oscillator (red curve) shift to longer delays. Correspondingly, changing the lifetime while keeping the resonance frequencies constant changes the decay rate of the fields and the width of the IAC envelope (c–d), while the fringe spacing stays the same. If the harmonic oscillator model is valid, the induced electric field can be fully retrieved through a fitting procedure provided that the excitation pulse is well characterized [97]. However, the assumption of the sample response being described by a single harmonic oscil-

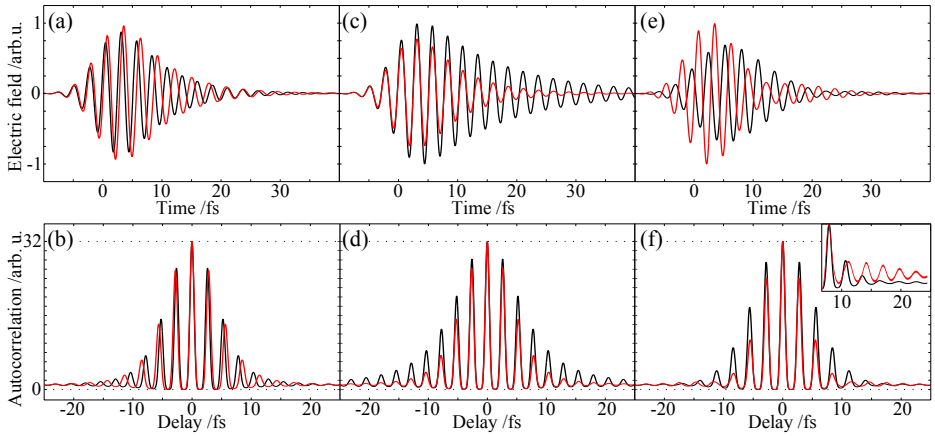

Figure 6.6: Electric fields of harmonic oscillators excited by few-cycle laser pulses (upper row), and the corresponding third-order IACs (lower row). (a–b) Response of two harmonic oscillators with different eigenfrequencies but identical lifetimes, excited by a 5.5 fs Fourier limited pulse centred around 1.55 eV. The IACs have the same envelopes, but the spacing between the fringes differs. (c–d) Response of two harmonic oscillators with identical eigenfrequencies (1.65 eV) but different lifetimes. The IACs then show the same fringe positions, but different envelopes. (e–f) Two different linear combinations of the responses to the two harmonic oscillators in (a–b). The IACs have different envelopes, but also show differences in the fringe positions, as shown in the inset of (h) where the two IACs are shown with a different normalization to highlight the positions of the fringes.

lator is a drastic simplification of most experimental systems, especially when using broadband excitation. As a first extension of the single harmonic oscillator approximation, one can consider the superposition of the responses from two oscillators. This is shown for an example case of two linear superpositions of the oscillators of (a–b), having the same lifetime but different resonance frequencies. The resulting fields (figure 6.6e) can show more complicated dynamics due to beating between the two modes. The resulting IACs (figure 6.6f) from two different linear combinations of the same two oscillators differ both by the envelope and the positions of the fringes. The shift of the fringe position between the two IACs is also not trivial; while the black curve is slightly shifted to shorter delays for the fringes at 4π and 6π phase delay (~ 5.5 fs and ~ 8 fs), it shows a clear shift in the opposite direction for the fringes further out in the IAC.

If multiple surface plasmon modes are excited simultaneously, a fit using multiple harmonic oscillators can in some cases provide a valid physical picture. However, the harmonic oscillator model is only applicable in the quasi-static limit, where retardation effects are negligible. For a system where the excitation field varies significantly across its dimensions, the response can no longer be considered purely local. The induced field at point $\vec{r}_1$ instead depends both on the excitation field at $\vec{r}_1$ and on the field at point $\vec{r}_2$, for each point $\vec{r}_2$ that is part

of the same nanosystem. This will be further discussed in the next subsection, with the rice-shaped particles on which Paper **II** is based as examples.

Even in cases of negligible retardation effects, a larger number of fit parameters increases the demands on the precision of the measurement of both the laser pulse and the IAC. The focus in Papers **II**–**III** has therefore been on the induced field itself rather than on the extraction of plasmon resonance parameters. In both of these studies, the positions of the fringes in the IAC at delays up to approximately 10 fs were studied. At these short delays, which are on the order of both the pulse duration and the surface plasmon lifetimes, the IAC is dominated by the interference between the strongest parts of the fields induced by the two pulses. Recalling that the $\tau = 0$ peak always coincides for all points in an image due to symmetry, shifts of the position of the first few fringes imply different spacings between the fringes. This in turn corresponds to different frequencies of the induced local field around its peak amplitude, as the interference between the strongest parts of the two fields dominates the IAC at short delays.

The criterion of a peak-to-background ratio of 2^{2n-1} (32 for $n = 3$) is very sensitive to the signal-to-noise ratio in the measurement, as well as to the stability and balance of the interferometer. This becomes especially problematic in ITR-PEEM measurements, where the typical exposure time for a single image is on the order of 30 s and hundreds of images need to be acquired. In contrast, the most common method for measuring an IAC is by frequency upconversion in a nonlinear medium, in which case the high signal-to-noise ratio can allow a whole measurement to be performed within a second. As examples for discussing the signal-to-noise ratio, figure 6.7 shows interferometric autocorrelations for a particle ensemble (a) and a single particle (b), respectively. The total integrated signal is approximately a factor of 60 larger for the ensemble measurement, which shows the expected peak-to-background ratio of 32. The peak-to-background ratio in the single-particle measurement is ~ 10. This demonstrates that the setup is stable and well aligned, but that the measurement of a weak signal from a small region does not necessarily yield a peak-to-background ratio of 32. The other criterion mentioned previously, the symmetry around the zero delay, is fulfilled to a reasonable extent for both measurements displayed in figure 6.7.

6.2.2 ITR-PEEM of Ag nanorice

An example of a system where retardation effects are prominent is the case of a rice-shaped nanoparticle excited by grazing-incidence p-polarized laser pulses. This experimental situation was used for Paper **II**, and is shown schematically in figure 6.8a. As the length of the particle is on the order of half a wavelength of the light, the excitation field will have different phases at the two ends. This phase difference has important effects on the local field at the particle, as the surface plasmon mode(s) of the particle will be driven with different phase at different points. Still, as the surface plasmon is a collective excitation involving all of the conduction electrons in the particle, there is an internal coupling. Furthermore, dark modes will be possible to excite as the quasi-static (or dipole) approximation

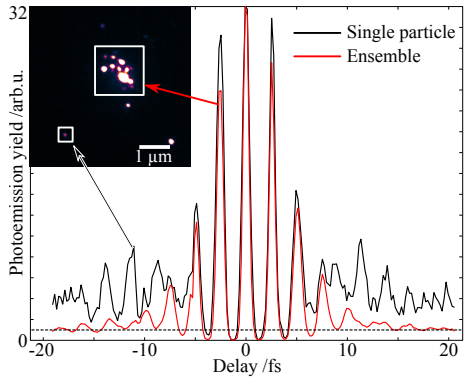

Figure 6.7: Comparison between an IAC measured from a single particle and that measured from an ensemble of aggregated particles. Both curves are normalized to reach from zero to a maximum value of 32. While the ensemble measurement shows the expected peak-to-background ratio of 32, the single particle measurement instead has a peak-to-background ratio of approximately 10. The sample is Ag nanorice on an ITO substrate; the excitation is a 5.5 fs laser pulse centred around 800 nm.

no longer holds.

The retardation effect in extended systems can be seen as an interference effect between the freely propagating light source and the surface plasmon excitation propagating from the part first struck by the excitation pulse. This leads to a nonlocal response; the plasmon response at point $\vec{r}$ depends not only on the excitation field at point $\vec{r}$, but on the field at a set of points. An illustrative example of this is a rice-shaped particle excited by a broadband laser pulse where the particle response is dominated by the $m = 2$, or quadrupole, mode. This mode is dark, and can thus not be excited at normal incidence. Figure 6.8b shows the simulated absorption spectrum of a 500 nm long particle. In figure 6.8c–d, the component normal to the substrate of the instantaneous electric field is shown in the plane of incidence during two half-cycles of the electric field. The first series of images (c) shows the electric field evolution during a half-cycle close to the maximum near-field amplitude. The second set of snapshots (d) shows the evolution at a time 10 fs later, when the excitation pulse has passed. Figure 6.8e shows the field as a function of time at the two ends of the particle. This shows how the fields at the two ends of the particle are driven out of phase by the pulse because of the phase difference of the excitation across the particle. However, the $m = 2$ mode dominating the particle response is even, so when the excitation pulse has passed the fields at the two ends oscillate in phase. If the excitation pulse is only a few cycles, this transition between out-of-phase excitation and in-phase free oscillation occurs during a time comparable to the optical period. This leads to a frequency difference between the fields at different points of the particle during the few cycles of maximum field enhancement, despite both the surface plasmon resonance frequency and the excitation frequency being the same

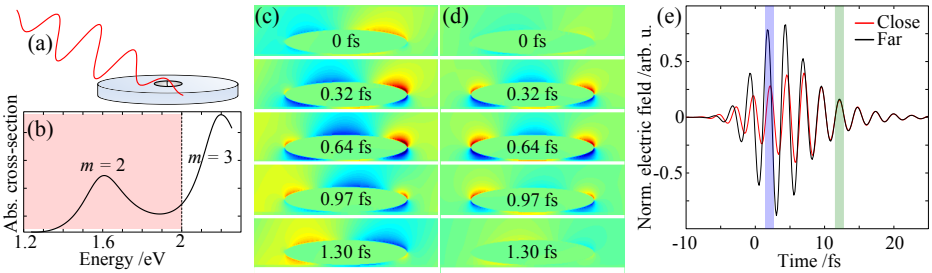

Figure 6.8: (a) Schematic of a rice-shaped particle excited by a laser pulse whose wavelength is approximately twice the particle length. (b) Simulated absorption cross-section for a 500 nm rice-shaped Ag particle. The red shaded area represents the approximate spectral window of the laser pulse. (c–d) Sequences of images showing snapshots of the z-component of the electric field during a half-cycle just before (c) and slightly after (d) the maximum amplitude of the field. The scale in (c) is from -5 to $+5$, while that in (d) is from -2 to $+2$ relative to the amplitude of the excitation pulse. (e) z-component of the electric field at the two ends of the particle. The blue and green shaded areas represent the time windows from which the snapshots of (c) and (d) are taken, respectively.

across the particle.

From the previous discussion on the interferometric autocorrelation, the shift in frequency observed around the peak amplitude of the field in figure 6.8e should appear in the IAC as a difference in the fringe spacing at short delays. Indeed, calculating the IACs from the two fields shown in figure 6.8, the fringes in the IACs from the two ends appear shifted with respect to each other (figure 6.9a). This can also be measured experimentally in an ITR-PEEM setup, which was done in Paper **II**. An example of IACs measured by ITR-PEEM from two ends of a rice-shaped particle is shown in figure 6.9b. The shift between the fringes from the two ends visible at 5 fs delay (corresponding in this case to two cycles) shows that the fringe spacing is different for the few central fringes of the IAC.

The spectrum in figure 6.8b shows an $m = 2$ mode that is well centred in the spectral window of the laser pulse, and that completely dominates the response. However, for other lengths of the particles two modes can overlap with the laser spectrum. In this case, the fields, and thus also the IACs, become more complicated due to the beating between the different modes. This combination of modes can further add to the difference in dynamics between the two ends if the two modes have different parities. The $m = 2$ mode, for example, corresponds to an in-phase oscillation of the two ends, while the $m = 3$ mode corresponds to an out-of-phase oscillation. This case of complicated dynamics resulting from excitation of multiple modes is also discussed in Paper **II**.

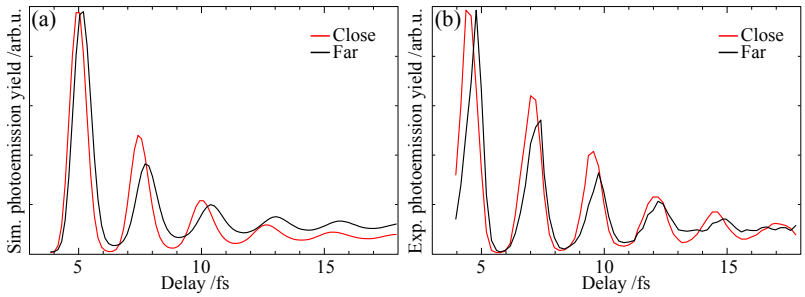

Figure 6.9: (a) Calculated interferometric autocorrelations from the fields shown in figure 6.8e, showing how the frequency difference existing during a few cycles appears as a shift in the fringe position between the two ends. (b) Experimental ITR-PEEM measurement of a rice-shaped Ag particle of 380 nm length, showing a similar shift between the fringes from the two ends.

6.3 PEEM using high-order harmonics

PEEM using high-order harmonic sources has the capability of providing direct real-space motion pictures of near-field dynamics with attosecond temporal resolution [17]. However, the use of high-order harmonics in PEEM is challenging due to the high flux required for PEEM imaging compared to, for example, spatially averaged photoelectron spectroscopy. As most high-order harmonic sources have repetition rates of 1 kHz or below, their use for PEEM applications has been associated with severe experimental concerns, especially considering space charge effects [18, 19].

Two different setups for PEEM using high-order harmonics have been employed in the work behind this thesis. In Paper **VI**, we follow up on the initial experiments performed by Mikkelsen *et al.* [18] using the 1 kHz chirped-pulse amplification (CPA) system described in section 3.2.2. In Paper **VII**, we provide a summary of the early experiments using a 1 kHz HHG source, and present new measurements performed using the 200 kHz optical parametric chirped-pulse amplification (OPCPA) system described in section 3.2.3.

6.3.1 1 kHz CPA system

Because of the space charge effects described in section 5.3, the intensity achievable with harmonics generated by the 1 kHz CPA system is far too high for PEEM applications. Therefore, in the experimental setup used for Paper **VI**, the microscope was placed approximately 80 cm behind the focus of the beam. In the focus, a magnetic bottle electron spectrometer (MBES) was placed for characterization of the harmonics. This experimental setup, including the Mach-Zehnder interferometer used for pump–probe experiments, is shown in figure 6.10.

Practical PEEM imaging using a 1 kHz laser system is about optimizing a range of parameters, the most important of which are laser intensity, contrast aperture,

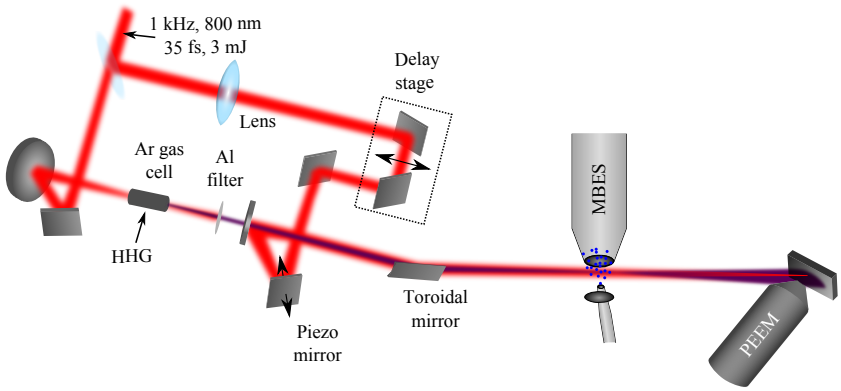

Figure 6.10: Experimental setup for Paper **VI**. The focus point of the XUV beam is ∼80 cm before the PEEM to avoid space charge effects, while the focus point of the IR beam is moved closer to the PEEM using an additional lens. MBES: Magnetic Bottle Electron Spectrometer.

and exposure time. Space charge effects are reduced by using a low pulse energy; however, this also inevitably results in a poor signal-to-noise ratio. At some point, it can be advantageous to work in a regime where slight space charge blurring occurs, if the signal-to-noise ratio otherwise becomes too low. The same applies for the contrast aperture. As described in section 5.2, a small contrast aperture reduces both spherical and chromatic aberrations, and is therefore crucial for obtaining a high resolution. Even with a small energy spread of the emitted electrons, the calculated spatial resolution in the FOCUS IS-PEEM is hundreds of nanometres if operated using the 500 µm contrast aperture, as seen in figure 5.4. However, a large contrast aperture might still be favourable in order to increase the signal-to-noise ratio. This is especially true for pump–probe experiments, where a series of ∼100 images is typically needed.

An estimate of the noise levels for typical exposure times is shown in figure 6.11 for a sample of Ag nanowires on a Au substrate. The sample is illuminated by XUV attosecond pulse trains and IR femtosecond pulses simultaneously, with the latter giving rise to the few intense hot-spots in the images. Red arrows indicate a region with two nanowires lying across each other. With 100 s exposure time (a), these wires cannot be resolved at the marked point. With 300 s exposure time (b), the two wires are clearly separated. The image gets even sharper with 3000 s exposure time (c), but the improvement is not drastic.

6.3.2 200 kHz OPCPA system

The peak intensity of the high-order harmonics produced by the 200 kHz system is significantly lower than that from the 1 kHz system. The experiments using HHG at 200 kHz repetition rate, presented in Paper **VII**, were therefore performed with

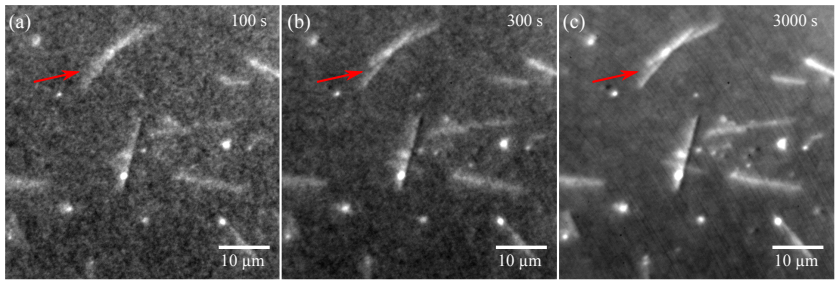

Figure 6.11: PEEM images acquired using XUV attosecond pulse trains and IR femtosecond pulses from the 1 kHz CPA system. The sample is Ag nanowires on a Au substrate. Exposure times are (a) 100 s, (b) 300 s, and (c) 3000 s.

the harmonics focused onto the sample. However, due to geometrical limits set by the physical size of the vacuum chambers, the toroidal mirror used to focus the XUV radiation had to be placed at least ∼95 cm from the gas jet. The toroidal mirror, on the other hand, was designed for placement 60 cm from the gas jet. This physical restraint in the setup led to an unavoidable coma in the focal spot profile, but also to the divergent beam being partially cut by the toroidal mirror. The focal spot profile was monitored by imaging the fundamental beam reflected off the sample using a lens. In a first version of the setup, only the rotation of the toroidal mirror could be adjusted when the chamber was evacuated, which made alignment difficult. This was adjusted for in a later version of the setup, which also included an electrically controlled tilt stage for the toroidal mirror. A typical optimum focal spot profile of the IR beam is shown in figure 6.12a. However, the shape of the focal spot can be different for the IR and XUV beams due to the difference in both divergence angle and wavelength. Figure 6.12b shows a PEEM image acquired in low-magnification mode at a field-of-view of 388 µm, with Ar in the HHG chamber but without any metallic filter. The sample is an evaporated Au film. The image is therefore dominated by photoemission from the strong low-order harmonics (mainly harmonics 3 and 5), with some hot-spots due to multiphoton photoemission induced by the fundamental beam. In contrast, figure 6.12c shows a PEEM image acquired under the same conditions but with a 200 nm Al filter blocking the fundamental beam and the low-order harmonics. As is apparent from these images, the focal spot profiles can show large differences depending on which parts of the radiation are used.

As expected, the imaging can be vastly improved by increasing the repetition rate from 1 kHz to 200 kHz, even when reducing the exposure times by an order of magnitude. Figure 6.13 shows PEEM images acquired with XUV attosecond pulse trains from (a) the 1 kHz system during 400 seconds, and (b) the 200 kHz system during 30 seconds. Both samples consist of similar Ag nanowires on a Au substrate. A profile across the wires show a reduction in the apparent width by approximately a factor of 3 (figure 6.13c). The issues with obtaining an adequate focal spot profile on the sample in the first experimental setup with the 200 kHz

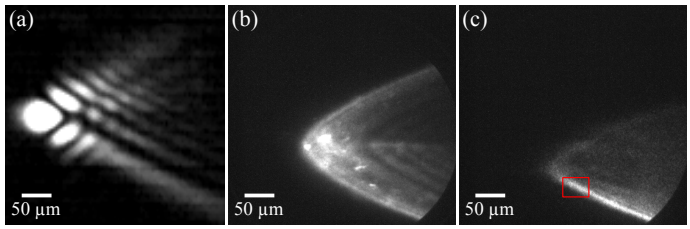

Figure 6.12: (a) Focal spot profile of the IR beam as imaged from the beam reflected off the sample. (b) Low-magnification PEEM image acquired without any filter after the harmonic generation. (c) Same as (b), but with an Al filter blocking the fundamental beam and low-order harmonics. The MCP voltage was also increased to get a suitable image intensity. The red rectangle marks the part of the spot used for high-resolution imaging.

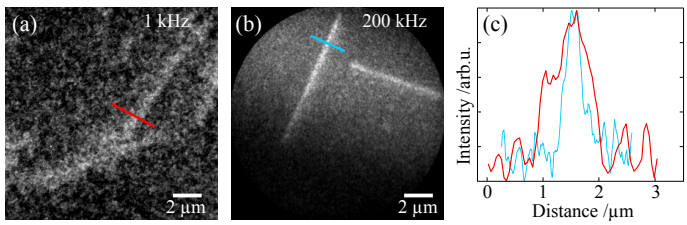

Figure 6.13: Comparison of the image quality when using high-order harmonics from (a) the 1 kHz CPA system with 400 s exposure time, and (b) the 200 kHz OPCPA system with 30 s exposure time. (c) Intensity profiles along the lines indicated in (a–b). Despite more than a factor of 10 shorter exposure time, the obtainable image quality is much higher with the 200 kHz HHG source.

system can also be seen in (b) as a bright stripe across the image. This bright stripe is the most intense part of the of the XUV focal spot, as indicated by the red rectangle in figure 6.12c.

The third generation of the setup for PEEM using high-order harmonics at high repetition rate is being commissioned during the writing of this thesis, and features a new vacuum chamber allowing placement of the toroidal mirror at the appropriate distance from the gas jet. This will facilitate a more controlled spot profile on the sample, thus reducing any wavefront distortions. The new setup will also feature an in-vacuum interferometer for IR pump–XUV probe experiments. This new setup is shown schematically in figure 6.14.

6.3.3 Contrast

A practical issue with XUV imaging is the image contrast. For multiphoton PEEM, the contrast typically reflects the enhanced nano-optical fields due to the nonlinear photoemission process. For photoemission by XUV radiation, however,

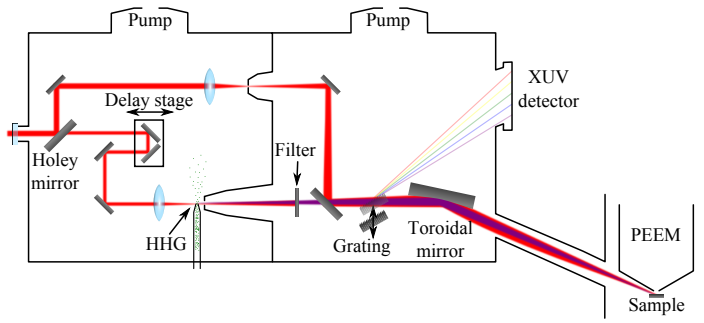

Figure 6.14: Schematic of the new setup for IR pump–XUV probe experiments. The pulse is split inside the vacuum chamber by a mirror with a hole in its centre. A grating can be inserted into the beam to disperse the XUV radiation onto a coated MCP for measuring the XUV spectrum.

the contrast mechanisms are sensitive to the band structure and the ionization cross-section of the material. In combination with the low signal-to-noise ratio in HHG-PEEM experiments, this makes it necessary to find a materials system where the plasmonic structures of interest show a higher emission yield than the substrate. In Paper **VI**, we experimentally investigated the contrast in secondary electron imaging of Ag nanowires on three different substrates: Cr, Au, and ITO. Representative images are shown in figure 6.15. It is seen that the ITO substrate, which has beneficial optical properties, emits significantly more secondary electrons than do the Ag nanowires. Using this system to study field dynamics in the Ag nanowires would therefore be challenging, because of the higher yield from the substrate decreasing the signal-to-noise level. The Au substrate, however, shows a low emission yield such that the Ag nanowires appear significantly brighter in the PEEM image.

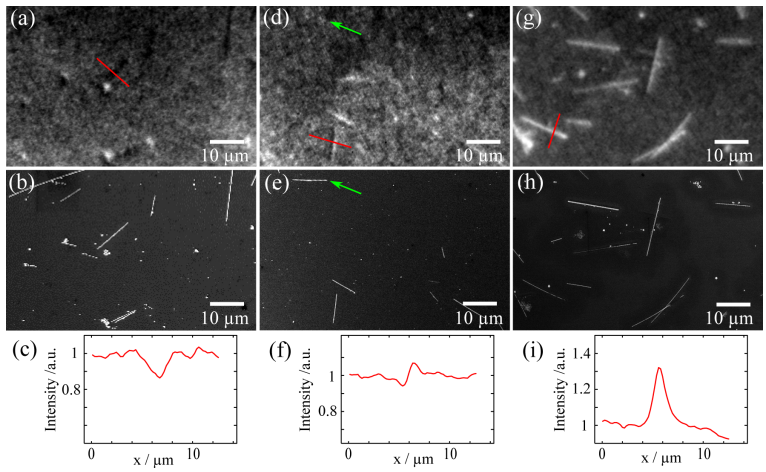

Figure 6.15: Image contrast for different substrates. Top row shows PEEM images acquired using XUV attosecond pulse trains at 1 kHz repetition rate. Middle row shows SEM images of the same areas, and bottom row shows intensity profiles along the red lines in the PEEM images. For the ITO substrate (a–c), the nanowires show an inverse contrast as the substrate appears brighter. On the Cr substrate (d–f), the nanowires and the substrate show almost the same intensity, and only the side of the nanowire facing the radiation appears bright in the image (the XUV radiation is incident from the right). The horizontal nanowire marked with green arrows cannot be seen at all. On the Au substrate (g–h), the nanowires clearly emit more electrons than does the substrate.

Chapter 7

Conclusions and Outlook

7.1 Perspectives on nonlinear PEEM

Nonlinear laser-based PEEM for characterization of nano-optical fields has been around for more than a decade now, with a steadily increasing number of research groups using the technique. The experimental schemes presented have evolved from early investigations of where on the surface the electric field is enhanced [125, 126, 147] to advanced experimental schemes involving polarization pulse shaping for coherent control [16], correlated PEEM and optical measurements [58], aberration corrected instruments [141], or two-dimensional spectroscopy with nanoscale spatial resolution [130]. The systems studied have gone from mesoscopic metal particles and randomly rough surfaces to now include dielectric waveguides [148], solar cell absorber layers [107], and plasmonic devices [149].

My contribution to this field has been to explore combinations of PEEM with novel, advanced laser sources. This has resulted in the first images acquired with sub-6 fs pulses from an ultra-broadband oscillator (Papers **I**–**III**), with femtosecond pulses at 1.55 μm (Paper **IV**), and with amplified sub-7 fs pulses from an OPCPA system (Paper **V**). These light sources all have their strengths and weaknesses depending on the system under study, but together they show the huge possibilities offered by the wide and quickly evolving selection of table-top laser sources.

Oscillators are stable, compact, and reliable light sources that operate at high repetition rates, which is more or less a prerequisite for PEEM applications. Nonetheless, they can deliver laser pulses with durations down to two optical cycles. In Paper **II**, pulses from such an oscillator were used to extend the method of interferometric time-resolved PEEM to the few-femtosecond regime. This led to new experimental insights into how the local near-field is affected by effects like retardation and beating. Oscillators still have a rather low pulse energy, which limits their use to systems showing large field enhancements, such as metallic nanostructures, or to systems where photoemission can be achieved by fewer than three photons.

Optical parametric amplifiers can provide higher pulse energies than oscillators, while still working at repetition rates of hundreds of kHz or even MHz. This type of light source was therefore used to study the moderate field enhancements in semiconductor nanowires in Paper **V**. Optical parametric amplifiers can also

be used to generate femtosecond pulses with tunable wavelengths, such as the 1.55 μm pulses used for Paper **IV**.

7.2 Towards attosecond PEEM

Ever since the proposal of an attosecond nanoplasmonic-field microscope by Stockman in 2007 [17], at least two research groups have tried to combine PEEM with HHG sources to reach attosecond temporal resolution. However, the combination has turned out to be quite challenging, and the output has been limited to three journal articles published so far ([18], [19], and Paper **VI**). Up until now, the main challenges have been space charge effects and experimental stability, which are both helped by the development of new HHG sources working at high repetition rate. This was also shown in Paper **VII** to vastly improve the imaging conditions.

Even with reliable high-repetition rate attosecond light sources becoming more available, attosecond PEEM poses new challenges not present for the case of nonlinear PEEM. The original proposal [17] described the streaking by instantaneous acceleration of the photoemitted electrons. However, the instantaneous acceleration requires a highly localized electric field, which sets demands on a spatial resolution in the 1 nm regime. While aberration corrected instruments might reach this goal within a few years, doing it in combination with an attosecond light source is a whole other challenge. The requirement of instantaneous acceleration is however not set in stone; simulations of streaking in nanoplasmonic fields have suggested that it is possible to retrieve the electric field anyway [150], thus lowering the demands on field localization at the cost of a more complicated interpretation of the experiment. Another issue is the high field strength of several V/nm necessary for streaking experiments [17, 150], giving rise to a large background of nonlinearly emitted electrons that can contribute with space charge effects. A way to circumvent this is the use of higher photon energies of the attosecond pulse, but this is in turn associated with lower ionization cross-sections and worse performance of the microscope. Furthermore, the requirements of high near-field strengths effectively limits the technique to studies of plasmonic "hot-spots" showing very high field enhancements.

An alternative approach to electron streaking in the nanoplasmonic field is to study changes in the yield of either primary or secondary electrons (SEs) due to the varying electron density associated with the surface plasmon. The SE approach is especially favourable from an experimental point of view, as SEs are abundant and have a reasonably low energy. SEs can even be merged into a narrow low-energy peak by adsorption of a surface layer [151]. However, the SE atto-PEEM concept is less direct than the streaking concept, and no reliable estimate of the magnitude of the surface plasmon-induced change in the SE yield has been made. The achievable temporal resolution also depends on the exact mechanism from excitation by the attosecond pulse to emission of SEs, and could be limited by the duration of the SE cascade to around 0.5–1 fs.

7.3 Prophecies and forecasts

There are many different paths ahead for laser-based PEEM research. Some of these involve more application-centred studies of, for example, solar cell materials [107], a path that can lead to studies of field dynamics in actual operational devices. PEEM could offer direct spatiotemporal imaging of how radiation is transferred into a collective electron excitation followed by the decay into single-particle excitations, increasing the understanding of plasmon-enhanced solar cell devices [152].

Another, more fundamental path is the hunt for attosecond temporal resolution, as discussed in the previous section. While there are still significant challenges ahead, the remaining obstacles are "only" technological ones, and extrapolating from the rapid development of experimental instrumentation during the past decade it seems reasonable to expect a working atto-PEEM setup within 5 years from today. Looking further ahead, attosecond pump–attosecond probe light sources are becoming a reality and could possibly be used for direct imaging of fundamental processes such as hole screening in metals on a sub-femtosecond time scale.

The use of optical parametric amplifiers dramatically increases the range of available femtosecond pulses from the "traditional" Ti:sapphire pulses and their harmonics. Moreover, pulses of different, precisely tuned wavelengths can be generated from seeds from the same oscillator to ensure synchronization. This leads to many possibilities for multi-colour pump–probe experiments with a temporal resolution of tens to hundreds of femtoseconds, where the pulses can be tuned to image transitions via selected intermediate states.

Finally, there is currently a development of HHG sources designed not for attosecond pulse generation, but as user-friendly table-top sources of XUV and soft X-ray radiation. This development is likely to continue, leading to high-repetition rate systems delivering femtosecond pulses with up to hundreds of eV photon energy. This would mean that most of the PEEM experiments currently only available at giant and expensive synchrotron facilities could be performed in-house, using a relatively cheap and small HHG source. The intrinsic possibility of femtosecond temporal resolution would in this case only be a bonus.

Bibliography

[1] M. L. Brongersma and V. M. Shalaev, *The case for plasmonics*, Science **328**, 440 (2010).

[2] "Ernst Ruska – Biographical". *nobelprize.org*. Nobel Media AB 2014. Web. 15 Nov 2015., <http://www.nobelprize.org/nobel_prizes/physics/laureates/1986/ruska-bio.html>.

[3] M. A. O'Keefe *et al.*, *Sub-Ångstrom high-resolution transmission electron microscopy at 300 keV*, Ultramicrosc. **89**, 215 (2001).

[4] P. E. Batson, N. Dellby, and O. L. Krivanek, *Sub-Ångstrom resolution using aberration corrected electron optics*, Nature **418**, 617 (2002).

[5] A. L. Cavalieri *et al.*, *Attosecond spectroscopy in condensed matter*, Nature **449**, 1029 (2007).

[6] K. Klünder *et al.*, *Probing single-photon ionization on the attosecond time scale*, Phys. Rev. Lett. **106**, 143002 (2011).

[7] T. H. Maiman, *Stimulated optical radiation in ruby*, Nature **187**, 493 (1960).

[8] E. Goulielmakis *et al.*, *Single-cycle nonlinear optics*, Science **320**, 1614 (2008).

[9] "Press Release: The 1999 Nobel Prize in Chemistry". *nobelprize.org*. Nobel Media AB 2014. Web. 16 Nov 2015., <http://www.nobelprize.org/nobel_prizes/chemistry/laureates/1999/press.html>.

[10] A. McPherson *et al.*, *Studies of multiphoton production of vacuum-ultraviolet radiation in the rare gases*, J. Opt. Soc. Am. B **4**, 595 (1987).

[11] M. Ferray *et al.*, *Multiple-harmonic conversion of 1064 nm radiation in rare gases*, J. Phys. B: At., Mol. Opt. Phys. **21**, L31 (1988).

[12] K. Zhao *et al.*, *Tailoring a 67 attosecond pulse through advantageous phase-mismatch*, Opt. Lett. **37**, 3891 (2012).

[13] E. Brüche, *Elektronenmikroskopische Abbildung mit lichtelektrischen Elektronen*, Z. Phys. **86**, 448 (1933).

[14] O. Schmidt *et al.*, *Time-resolved two photon photoemission electron microscopy*, Appl. Phys. B **74**, 223 (2002).

[15] A. Kubo *et al.*, *Femtosecond imaging of surface plasmon dynamics in a nanostructured silver film*, Nano Lett. **5**, 1123 (2005).

[16] M. Aeschlimann *et al.*, *Adaptive subwavelength control of nano-optical fields*, Nature **446**, 301 (2007).

[17] M. I. Stockman *et al.*, *Attosecond nanoplasmonic-field microscope*, Nat. Photon. **1**, 539 (2007).

[18] A. Mikkelsen *et al.*, *Photoemission electron microscopy using extreme ultraviolet attosecond pulse trains*, Rev. Sci. Instrum. **80**, 123703 (2009).

[19] S. H. Chew *et al.*, *Time-of-flight-photoelectron emission microscopy on plasmonic structures using attosecond extreme ultraviolet pulses*, Appl. Phys. Lett. **100**, 051904 (2012).

[20] European Commission, *Commission Recommendation of 18 October 2011 on the definition of nanomaterial*, Official Journal of the European Union **275**, 38 (2011).

[21] Y. Sun and Y. Xia, *Shape-controlled synthesis of gold and silver nanoparticles*, Science **298**, 2176 (2002).

[22] Y. Sun and Y. Xia, *Large-scale synthesis of uniform silver nanowires through a soft, self-seeding, polyol process*, Adv. Mater. **14**, 833 (2002).

[23] H. Liang *et al.*, *High-yield uniform synthesis and microstructure-determination of rice-shaped silver nanocrystals*, J. Am. Chem. Soc. **131**, 6068 (2009).

[24] X. Lu *et al.*, *Chemical synthesis of novel plasmonic nanoparticles*, Annu. Rev. Phys. Chem. **60**, 167 (2009).

[25] Y. Sun *et al.*, *Polyol synthesis of uniform silver nanowires: A plausible growth mechanism and the supporting evidence*, Nano Lett. **3**, 955 (2003).

[26] R. S. Wagner and W. C. Ellis, *Vapor-liquid-solid mechanism of single crystal growth*, Appl. Phys. Lett. **4**, 89 (1964).

[27] M. T. Björk *et al.*, *One-dimensional heterostructures in semiconductor nanowhiskers*, Appl. Phys. Lett. **80**, 1058 (2002).

[28] J. Wallentin and M. T. Borgström, *Doping of semiconductor nanowires*, J. Mater. Res. **26**, 2142 (2011).

[29] S. Lehmann *et al.*, *A general approach for sharp crystal phase switching in InAs, GaAs, InP, and GaP nanowires using only group V flow*, Nano Lett. **13**, 4099 (2013).

[30] J. D. Jackson, *Classical Electrodynamics* (Wiley, 1999).

[31] A. D. Rakić *et al.*, *Optical properties of metallic films for vertical-cavity optoelectronic devices*, Appl. Opt. **37**, 5271 (1998).

[32] P. B. Johnson and R. W. Christy, *Optical constants of the noble metals*, Phys. Rev. B **6**, 4370 (1972).

[33] E. D. Palik, *Handbook of Optical Constants of Solids* (Academic Press, 1985).

[34] SCHOTT, Optical glass: Data sheets, <http://refractiveindex.info/download/data/2012/schott_optical_glass_collection_datasheets_dec_2012_us.pdf>, 2012, Web. 16 Sep 2015.

[35] D. E. Aspnes and A. A. Studna, *Dielectric functions and optical parameters of Si, Ge, GaP, GaAs, GaSb, InP, InAs, and InSb from 1.5 to 6.0 eV*, Phys. Rev. B **27**, 985 (1983).

[36] J. Zuloaga, E. Prodan, and P. Nordlander, *Quantum description of the plasmon resonance of a nanoparticle dimer*, Nano Lett. **9**, 887 (2009).

[37] J. Zuloaga, E. Prodan, and P. Nordlander, *Quantum plasmonics: Optical properties and tunability of metallic nanorods*, ACS Nano **4**, 5269 (2010).

[38] Y. Wang *et al.*, *Ultrafast nonlinear control of progressively loaded, single plasmonic nanoantennas fabricated using helium ion milling*, Nano Lett. **13**, 5647 (2013).

[39] L. Novotny and B. Hecht, *Principles of Nano-Optics* (Cambridge University Press, 2006).

[40] G. Mie, *Beiträge zur Optik trüber Medien, speziell kolloidaler Metallösungen*, Ann. Phys. **25** (1908).

[41] S. A. Maier, *Plasmonics: Fundamentals and Applications* (Springer Science, 2007).

[42] R. H. Ritchie, *Plasma losses by fast electrons in thin films*, Phys. Rev. **106**, 874 (1957).

[43] C. J. Powell and J. B. Swan, *Origin of the characteristic electron energy losses in aluminum*, Phys. Rev. **115**, 869 (1959).

[44] C. Sönnichsen *et al.*, *Drastic reduction of plasmon damping in gold nanorods*, Phys. Rev. Lett. **88**, 077402 (2002).

[45] H. Wei *et al.*, *Multipolar plasmon resonances in individual Ag nanorice*, ACS Nano **4**, 2649 (2010).

[46] P. Nordlander *et al.*, *Plasmon hybridization in nanoparticle dimers*, Nano Lett. **4**, 899 (2004).

[47] M. Fleischmann, P. Hendra, and A. McQuillan, *Raman spectra of pyridine adsorbed at a silver electrode*, Chem. Phys. Lett. **26**, 163 (1974).

[48] M. Moskovits, *Surface-enhanced Raman spectroscopy: A brief retrospective*, J. Raman Spectrosc. **36**, 485 (2005).

[49] A. Lewis *et al.*, *Development of a 500 Å spatial resolution light microscope: I. light is efficiently transmitted through $\lambda/16$ diameter apertures*, Ultramicrosc. **13**, 227 (1984).

[50] D. A. Higgins and E. Mei, Near-field scanning optical microscopy, in *Scanning Probe Microscoy and Spectroscopy*, Wiley-VCH, 2001.

[51] M. Kociak and J. García de Abajo, *Nanoscale mapping of plasmons, photons and excitons*, MRS Bull. **37**, 39 (2012).

[52] O. Nicoletti *et al.*, *Three-dimensional imaging of localized surface plasmon resonances of metal nanoparticles*, Nature **502**, 80 (2013).

[53] A. Losquin *et al.*, *Experimental evidence of nanometer-scale confinement of plasmonic eigenmodes responsible for hot spots in random metallic films*, Phys. Rev. B **88**, 115427 (2013).

[54] Y. Fujikawa, T. Sakurai, and R. M. Tromp, *Surface plasmon microscopy using an energy-filtered low energy electron microscope*, Phys. Rev. Lett. **100**, 126803 (2008).

[55] R. Gómez-Medina *et al.*, *Mapping plasmons in nanoantennas via cathodoluminescence*, New J. Phys. **10**, 105009 (2008).

[56] B. Barwick, D. J. Flannigan, and A. H. Zewail, *Photon-induced near-field electron microscopy*, Nature **462**, 902 (2009).

[57] A. Losquin *et al.*, *Unveiling nanometer scale extinction and scattering phenomena through combined electron energy loss spectroscopy and cathodoluminescence measurements*, Nano Lett. **15**, 1229 (2015).

[58] F. Schertz *et al.*, *Near field of strongly coupled plasmons: Uncovering dark modes*, Nano Lett. **12**, 1885 (2012).

[59] S. Asano and G. Yamamoto, *Light scattering by a spheroidal particle*, Appl. Opt. **14**, 29 (1975).

[60] K. Yee, *Numerical solution of initial boundary value problems involving Maxwell's equations in isotropic media*, IEEE Trans. Antennas Propag. **14**, 302 (1966).

[61] A. Taflove and S. C. Hagness, *Computational Electrodynamics: The Finite-Difference Time-Domain Method, Third Edition* (Artec House, 2005).

[62] P. Rudawski, *Second-generation High-Order Harmonic Sources*, PhD thesis, Lund University, 2014.

[63] D. Guénot, *Probing Electron Correlation on the Attosecond Timescale*, PhD thesis, Lund University, 2014.

[64] R. Szipöcs *et al.*, *Chirped multilayer coatings for broadband dispersion control in femtosecond lasers*, Opt. Lett. **19**, 201 (1994).

[65] J. Matyschok *et al.*, *Temporal and spatial effects inside a compact and CEP stabilized, few-cycle OPCPA system at high repetition rates*, Opt. Express **21**, 29656 (2013).

[66] P. Rudawski *et al.*, *Carrier-envelope phase dependent high-order harmonic generation with a high-repetition rate OPCPA-system*, Eur. Phys. J. D **69**, 70 (2015).

[67] M. I. Stockman, S. V. Faleev, and D. J. Bergman, *Coherent control of femtosecond energy localization in nanosystems*, Phys. Rev. Lett. **88**, 067402 (2002).

[68] T. Brixner *et al.*, *Nanoscopic ultrafast space-time-resolved spectroscopy*, Phys. Rev. Lett. **95**, 093901 (2005).

[69] T. Utikal *et al.*, *All-optical control of the ultrafast dynamics of a hybrid plasmonic system*, Phys. Rev. Lett. **104**, 113903 (2010).

[70] M. Aeschlimann *et al.*, *Spatiotemporal control of nanooptical excitations*, Proc. Natl. Acad. Sci. U. S. A. **107**, 5329 (2010).

[71] A. Anderson *et al.*, *Few-femtosecond plasmon dephasing of a single metallic nanostructure from optical response function reconstruction by interferometric frequency resolved optical gating*, Nano Lett. **10**, 2519 (2010).

[72] N. Accanto *et al.*, *Capturing the optical phase response of nanoantennas by coherent second-harmonic microscopy*, Nano Lett. **14**, 4078 (2014).

[73] P. B. Corkum and F. Krausz, *Attosecond science*, Nature Phys. **3**, 381 (2007).

[74] F. Krausz and M. Ivanov, *Attosecond physics*, Rev. Mod. Phys. **81**, 163 (2009).

[75] P. B. Corkum, *Plasma perspective on strong-field multiphoton ionization*, Phys. Rev. Lett. **71**, 1994 (1993).

[76] K. J. Schafer *et al.*, *Above threshold ionization beyond the high harmonic cutoff*, Phys. Rev. Lett. **70**, 1599 (1993).

[77] D. Guénot *et al.*, *Photoemission-time-delay measurements and calculations close to the 3s-ionization-cross-section minimum in Ar*, Phys. Rev. A **85**, 053424 (2012).

[78] E. P. Månsson *et al.*, *Double ionization probed on the attosecond timescale*, Nat. Phys. **10**, 207 (2014).

[79] K. Klünder, *Electron Wave Packet Dynamics on the Attosecond Time Scale*, PhD thesis, Lund Unviersity, 2012.

[80] C. M. Heyl *et al.*, *High-order harmonic generation with μJ laser pulses at high repetition rates*, J. Phys. B: At., Mol. Opt. Phys. **45**, 074020 (2012).

[81] M. Hentschel *et al.*, *Attosecond metrology*, Nature **414**, 509 (2001).

[82] J. Mauritsson *et al.*, *Coherent electron scattering captured by an attosecond quantum stroboscope*, Phys. Rev. Lett. **100**, 073003 (2008).

[83] H. Hertz, *Über einen Einfluss des ultravioletten Lichtes auf die electrische Entladung*, Ann. Phys. **267**, 983 (1887).

[84] F. Reinert and S. Hüfner, *Photoemission spectroscopy—from early days to recent applications*, New J. Phys. **7**, 97 (2005).

[85] A. Einstein, *Über einen die Erzeugung und Verwandlung des Lichtes betreffenden heuristischen Gesichtspunkt*, Ann. Phys. **322**, 132 (1905).

[86] J. J. Sakurai, *Modern Quantum Mechanics* (Addison-Wesley, 1994).

[87] S. Hüfner, *Photoelectron Spectroscopy: Principles and Applications* (Berlin: Springer, cop., 2003).

[88] C. N. Berglund and W. E. Spicer, *Photoemission studies of copper and silver: Theory*, Phys. Rev. **136**, A1030 (1964).

[89] P. A. Wolff, *Theory of secondary electron cascade in metals*, Phys. Rev. **95**, 56 (1954).

[90] J. C. Baggesen and L. B. Madsen, *Secondary-electron cascade in attosecond photoelectron spectroscopy from metals*, Phys. Rev. A **80**, 030901 (2009).

[91] H. Petek and S. Ogawa, *Femtosecond time-resolved two-photon photoemission studies of electron dynamics in metals*, Prog. Surf. Sci. **56**, 239 (1997).

[92] E. Knoesel *et al.*, *Dynamics of photoexcited electrons in metals studied with time-resolved two-photon photoemission*, Surf. Sci. **368**, 76 (1996).

[93] F. Weik, A. de Meijere, and E. Hasselbrink, *Wavelength dependence of the photochemistry of O2 on Pd(111) and the role of hot electron cascades*, J. Chem. Phys. **99**, 682 (1993).

[94] L. Bürgi *et al.*, *Probing hot-electron dynamics at surfaces with a cold scanning tunneling microscope*, Phys. Rev. Lett. **82**, 4516 (1999).

[95] A. García-Leuke *et al.*, *Role of occupied d bands in the dynamics of excited electrons and holes in Ag*, Phys. Rev. B **68**, 045103 (2003).

[96] B. H. Frazer *et al.*, *The probing depth of total electron yield in the sub-keV range: TEY-XAS and X-PEEM*, Surf. Sci. **537**, 161 (2003).

[97] M. Merschdorf, C. Kennerknecht, and W. Pfeiffer, *Collective and single-particle dynamics in time-resolved two-photon photoemission*, Phys. Rev. B **70**, 193401 (2004).

[98] M. Weida *et al.*, *Parallel excitation pathways in ultrafast interferometric pump-probe correlation measurements of hot-electron lifetimes in metals*, Appl. Phys. A **71**, 553 (2000).

[99] R. W. Boyd, *Nonlinear Optics* (Academic Press, 2003).

[100] H. Ueba and B. Gumhalter, *Theory of two-photon photoemission spectroscopy of surfaces*, Prog. Surf. Sci. **82**, 193 (2007).

[101] L. A. Lompre, J. Thebault, and G. Farkas, *Intensity and polarization effects of a single 30-psec laser pulse on five-photon surface photoeffect of gold*, Appl. Phys. Lett. **27**, 110 (1975).

[102] A. Damascelli *et al.*, *Multiphoton electron emission from Cu and W: An angle-resolved study*, Phys. Rev. B **54**, 6031 (1996).

[103] P. Dombi, F. Krausz, and G. Farkas, *Ultrafast dynamics and carrier-envelope phase sensitivity of multiphoton photoemission from metal surfaces*, J. Mod. Opt. **53**, 163 (2006).

[104] A. Gloskovskii *et al.*, *Electron emission from films of Ag and Au nanoparticles excited by a femtosecond pump-probe laser*, Phys. Rev. B **77**, 195427 (2008).

[105] O. W. Richardson, *The Emission of Electricity from Hot Bodies* (Longmans, Green and Co., 1916).

[106] E. Bauer, *Surface Microscopy with Low Energy Electrons* (Springer New York, 2014).

[107] M. Aeschlimann *et al.*, *Perfect absorption in nanotextured thin films via Anderson-localized photon modes*, Nat. Photon. **9**, 663 (2015).

[108] L. V. Keldysh, *Ionization in the field of a strong electromagnetic wave*, Sov. Phys. JETP **20**, 1307 (1965).

[109] M. Pant and L. K. Ang, *Ultrafast laser-induced electron emission from multiphoton to optical tunneling*, Phys. Rev. B **86**, 045423 (2012).

[110] F. Schertz *et al.*, *Field emission of electrons generated by the near field of strongly coupled plasmons*, Phys. Rev. Lett. **108**, 237602 (2012).

[111] P. Dombi *et al.*, *Ultrafast strong-field photoemission from plasmonic nanoparticles*, Nano Lett. **13**, 674 (2013).

[112] Focus GmbH, Omicron Nanotechnology, *Instruction Manual Focus PEEM*, , 2.2 ed., 2007.

[113] E. Bauer, *The resolution of the low energy electron reflection microscope*, Ultramicrosc. **17**, 51 (1985).

[114] M. Escher, N. Weber, and M. Merkel, *Electron optics of the photoelectron emission mircorscope (PEEM & NanoESCA)*, Lecture notes from 4th FOCUS PEEM workshop, 2011.

[115] J. Feng *et al.*, *An X-ray photoemission electron microscope using an electron mirror aberration corrector for the study of complex materials*, J. Phys. Cond. Mat. **17**, 1339 (2005).

[116] R. M. Tromp *et al.*, *A new aberration-corrected, energy-filtered LEEM/PEEM instrument. I. Principles and design*, Ultramicrosc. **110**, 852 (2010).

[117] T. Schmidt *et al.*, *First experimental proof for aberration correction in XPEEM: Resolution, transmission enhancement,and limitation by space charge effects*, Ultramicrosc. **126**, 23 (2013).

[118] G. F. Rempfer *et al.*, *Simultaneous correction of spherical and chromatic aberrations with an electron mirror: An electron optical achromat*, Microsc. Microanal. **3**, 14 (1997).

[119] N. M. Buckanie *et al.*, *Space charge effects in photoemission electron microscopy using amplified femtosecond laser pulses*, J. Phys. Cond. Mat. **21**, 314003 (2009).

[120] A. Locatelli *et al.*, *Image blur and energy broadening effects in XPEEM*, Ultramicrosc. **111**, 1447 (2011).

[121] G. A. Massey, M. D. Jones, and B. P. Plummer, *Space-charge aberrations in the photoelectron microscope*, J. Appl. Phys. **52**, 3780 (1981).

[122] P. Kruit and G. H. Jansen, Space charge and statistical coulomb effects, in *Handbook of Charged Particle Optics, Second Edition*, pp. 341–389, CRC Press, 2008.

[123] A. Zakharov, A.Mikkelsen, and J. Andersen, *Recent advances in imaging of properties and growth of low dimensional structures for photonics and electronics by XPEEM*, J. Electron Spectrosc. Relat. Phenom. **185**, 417 (2012).

[124] P. Kahl *et al.*, *Normal-incidence photoemission electron microscopy (NI-PEEM) for imaging surface plasmon polaritons*, Plasmonics **9**, 1401 (2014).

[125] O. Schmidt *et al.*, *The spatial distribution of non-linear effects in multi-photon photoemission from metallic adsorbates on Si(1 1 1)*, Surf. Sci. **482–485, Part 1**, 687 (2001).

[126] M. Cinchetti *et al.*, *Photoemission electron microscopy as a tool for the investigation of optical near fields*, Phys. Rev. Lett. **95**, 047601 (2005).

[127] L. I. Chelaru and F.-J. Meyer zu Heringdorf, *In situ monitoring of surface plasmons in single-crystalline Ag-nanowires*, Surf. Sci. **601**, 4541 (2007).

[128] L. Douillard *et al.*, *Short range plasmon resonators probed by photoemission electron microscopy*, Nano Lett. **8**, 935 (2008).

[129] R. C. Word, T. Dornan, and R. Könnenkamp, *Photoemission from localized surface plasmons in fractal metal nanostructures*, Appl. Phys. Lett. **96**, 251110 (2010).

[130] M. Aeschlimann *et al.*, *Coherent two-dimensional nanoscopy*, Science **333**, 1723 (2011).

[131] Q. Sun *et al.*, *Direct imaging of the near field and dynamics of surface plasmon resonance on gold nanostructures using photoemission electron microscopy*, Light: Sci. Appl. **2**, e118 (2013).

[132] S. J. Peppernick *et al.*, *Plasmon-induced optical field enhancement studied by correlated scanning and photoemission electron microscopy*, J. Chem. Phys. **138**, 154701 (2013).

[133] C. Lemke *et al.*, *The interplay between localized and propagating plasmonic excitations tracked in space and time*, Nano Lett. **14**, 2431 (2014).

[134] Y. Gong *et al.*, *Ultrafast imaging of surface plasmons propagating on a gold surface*, Nano Lett. **15**, 3472 (2015).

[135] R. C. Word, J. Fitzgerald, and R. Könenkamp, *Light propagation and interaction observed with electrons*, Ultramicrosc. **160**, 84 (2016).

[136] S. Kim *et al.*, *High-harmonic generation by resonant plasmon field enhancement*, Nature **453**, 757 (2008).

[137] M. Sivis *et al.*, *Extreme-ultraviolet light generation in plasmonic nanostructures*, Nat. Phys. **9**, 304 (2013).

[138] I. Katayama *et al.*, *Ultrafast dynamics of surface-enhanced raman scattering due to Au nanostructures*, Nano Lett. **11**, 2648 (2011).

[139] C. Wiemann *et al.*, *Local 2PPE-yield enhancement in a defined periodic silver nanodisk array*, Surf. Sci. **601**, 4714 (2007).

[140] M. Berndt *et al.*, *Polarization selective near-field focusing on mesoscopic surface patterns with threefold symmetry measured with PEEM*, Opt. Lett. **34**, 959 (2009).

[141] R. C. Word, J. Fitzgerald, and R. Könenkamp, *Photoelectron emission control with polarized light in plasmonic metal random structures*, Appl. Phys. Lett. **99**, 041106 (2011).

[142] P. Melchior *et al.*, *Optical near-field interference in the excitation of a bowtie nanoantenna*, Phys. Rev. B **83**, 235407 (2011).

[143] M. Aeschlimann *et al.*, *Observation of surface enhanced multiphoton photoemission from metal surfaces in the short pulse limit*, J. Chem. Phys. **102**, 8606 (1995).

[144] N. D. Lang, *Theory of work-function changes induced by alkali adsorption*, Phys. Rev. B **4**, 4234 (1971).

[145] J.-C. Diels *et al.*, *Control and measurement of ultrashort pulse shapes (in amplitude and phase) with femtosecond accuracy*, Appl. Opt. **24**, 1270 (1985).

[146] B. Lamprecht *et al.*, *Resonant and off-resonant light-driven plasmons in metal nanoparticles studied by femtosecond-resolution third-harmonic generation*, Phys. Rev. Lett. **83**, 4421 (1999).

[147] M. Munzinger *et al.*, *The lateral photoemission distribution from a defined cluster/substrate system as probed by photoemission electron microscopy*, New J. Phys. **7**, 68 (2005).

[148] J. P. S. Fitzgerald, R. C. Word, and R. Könenkamp, *Subwavelength visualization of light in thin film waveguides with photoelectrons*, Phys. Rev. B **89**, 195129 (2014).

[149] C. Lemke *et al.*, *Spatiotemporal characterization of SPP pulse propagation in two-dimensional plasmonic focusing devices*, Nano Lett. **13**, 1053 (2013).

[150] E. Skopalová *et al.*, *Numerical simulation of attosecond nanoplasmonic streaking*, New J. Phys. **13**, 083003 (2011).

[151] H. Ishiwata *et al.*, *Diamondoid coating enables disruptive approach for chemical and magnetic imaging with 10 nm spatial resolution*, Appl. Phys. Lett. **101**, 163101 (2012).

[152] H. A. Atwater and A. Polman, *Plasmonics for improved photovoltaic devices*, Nat. Mater. **9**, 205 (2010).

Summary of Papers

I. Direct Subwavelength Imaging and Control of Near-Field Localization in Individual Silver Nanocubes

We demonstrate near-field localization at the corners of individual Ag nanocubes, and show how we can image and control it. By tuning the polarization of a broadband laser pulse, we can selectively concentrate the enhanced near-field to one or two corners of the top face of the cube. The polarization concentrating the near-field to a particular corner is found to be close to when the electric field vector of the incoming beam is along the cube body diagonal through the particular corner.

II. Nanoscale Imaging of Local Few-Femtosecond Near-Field Dynamics within a Single Plasmonic Nanoantenna

We show how we can image local differences in the dynamics of the near-field within a single, subwavelength particle on a few-femtosecond time scale. We used interferometric time-resolved PEEM to measure local interferometric autocorrelations of the near-field, and found that the fringe positions in autocorrelations from different points of a particle can differ at delays as short as 3 fs. Using finite-difference time-domain simulations, we attribute the shifts of the fringe positions to different local instantaneous frequencies around the peak amplitude of the near-field. This is in turn caused by a combination of retardation effects and beating between multiple plasmon modes.

III. Size and Shape Dependent Few-Cycle Near-Field Dynamics in Individual Bow-Tie Nanoantennas

The near-field dynamics of individual bow-tie antennas in ordered arrays is compared by interferometric time-resolved PEEM measurements. We find that differences in the dynamics exist not only between antennas of different sizes, but also between antennas with similar geometry. The differences in the near-field dynamics are attributed to roughness and deviations from the ideal shape, which is also confirmed by finite-difference time-domain modelling.

IV. Photoemission Electron Microscopy of Localized Surface Plasmons in Silver Nanostructures at Telecommunication Wavelengths

This paper presents the extension of nonlinear PEEM to longer wavelength regimes, by using femtosecond pulses centred around 1.55 μm to image electrons emitted from silver nanoparticles. We find that the electron yield from a particle is not directly correlated with its size and shape as determined from scanning electron microscopy. We instead suggest that the higher yield from some particles is due to local field enhancements in the narrow particle–sample region of particles electrically contacted to the surface. Furthermore, spectroscopic investigations suggest that the photoemission process is not fully perturbative.

V. Direct Imaging of Crystal Phase Dependent Multiphoton Photoemission from InAs Nanowires

We investigate the polarization-dependent nonlinear photoemission from InAs nanowires with varying wurtzite and zincblende segments. The electron emission is seen to be maximized for different polarizations depending on the crystal structure. Through finite-difference time-domain simulations, we conclude that the polarization dependence of the emission from wurtzite InAs cannot be explained by the morphology of the segments. We therefore propose that the emission from the wurtzite segments is sensitive to anisotropic two- or three-photon transitions in the material, opening up an emission pathway whose cross-section depends on the polarization relative to the crystallographic axes.

VI. Secondary Electron Imaging of Nanostructures Using Extreme Ultra-Violet Attosecond Pulse Trains and Infra-Red Femtosecond Pulses

Imaging of Ag nanowires and nanoparticles is performed using XUV radiation from high-order harmonic generation. We investigate the contrast in secondary electron PEEM images for different material systems, finding that a Au substrate provides superior imaging conditions for Ag nanostructures when compared to Cr or indium tin oxide substrates. Furthermore, we employ a semiclassical theoretical model that suggests that the secondary electron cascade is fast enough to reveal surface plasmon dynamics on a sub-cycle timescale.

VII. Imaging Localized Surface Plasmons by Femtosecond to Attosecond Time-Resolved Photoelectron Emission Microscopy—"ATTO-PEEM"

In this book chapter, we discuss various aspects of PEEM imaging using femtosecond and attosecond pulses. We show how we have improved imaging conditions in multiple steps, including using a new high-repetition rate attosecond HHG source. This source is shown to give superior spatial resolution, while at the same time decreasing exposure times by more than an order of magnitude.